POLITECNICO DI TORINO

Master's Degree in Electronic Engineering

Master's Degree Thesis

Low-cost Antennas for SatCom on the Move Systems

Supervisors

Prof. Paola PIRINOLI

Prof. Giuseppe VECCHI

Dott. Michele BECCARIA

Dott. Giorgio GIORDANENGO

Candidate

Marco CAVALLO

December 2025

Acknowledgements

"Dedicated to my family,
for their constant love and support throughout this journey."

Ringrazio tutti i relatori e le persone che mi hanno aiutato in questi mesi permettendomi di svolgere la mia tesi di ricerca.
In particolar modo ringrazio profondamente la prof.ssa Paola Pirinoli per la sua massima disponibilità e gentilezza.
Desidero inoltre ringraziare il dott. Michele Beccaria per avermi aiutato con pazienza nelle prime fasi dello studio e il dott. Giorgio Giordanengo per i suoi consigli e la preziosa attenzione nei miei confronti.
Un grande ringraziamento va a Marco, Elisa e Battista, i migliori compagni di viaggio in questi due anni di università. Vi ringrazio per ogni momento trascorso, il sostegno da squadra per superare insieme ogni esame e tutte le passioni condivise.
Un ringraziamento lo dedico a tutte le persone conosciute e con cui ho lavorato in questo fantastico ambiente universitario e agli immancabili amici di Cuneo.
Ricordando il calore di casa, ringrazio Tata e Valerio, per il vostro immancabile affetto e i momenti preziosi trascorsi insieme, condividendo chiacchiere e passioni sportive.
Per concludere, il ringraziamento più grande e speciale va alla mia famiglia, alla quale dedico questa tesi.
A Mario, per l'esempio che sei sempre stato e i valori che mi hai insegnato.
A Anna, per l'amore materno che non è mai mancato.
A Luisa, per il sostegno nei momenti difficili ed il bene che mi hai sempre voluto.
A Matteo, per il legame fraterno che ci unisce nonostante la distanza.

Il mio grazie più sincero va a tutti voi.

Marco

Summary

Satellite Communication on the Move (SOTM) enables broadband connectivity for mobile platforms like vehicles, aircraft, and ships. In this context, the expansion of Low Earth Orbit (LEO) and Medium Earth Orbit (MEO) satellite constellations has improved communication capacity while reducing latency. However, this progress demands user terminals with better beam agility, reduced weight, and cost-efficiency. Traditional mechanically steered reflectors and phased arrays provide necessary performance but are unsuitable for widespread civilian use due to their complexity, high power consumption, and production costs. These challenges highlight the need for simpler and lightweight antennas that still meet the required radiation performance standards.

A possible solution consists of the use of a primary feed with a reduced number of electronically controlled elements plus a planar or slightly curved meta-lens, located in the near field region of the primary feed and realized with a (quasi-)planar structure, to reduce the antenna system profile.

The activity carried out in the thesis was focused on the design and analysis of the fully dielectric, planar meta-lens working in Ka-band and discretized with hexagonally arranged unit cells. Acting as a phase-modulating layer, the metasurface converts the feed's spherical wavefront into a collimated beam. For this purpose, the use of a hexagonal pattern provides an enhanced surface discretization, promoting a uniform behaviour radially from the structure's center. The use of dielectric materials enables fabrication through additive manufacturing techniques, resulting in a lightweight and mechanically robust structure.

Several geometric configurations for the unit cell were designed and then analyzed via full-wave simulations in CST Microwave Studio to quantify scattering parameters and phase control performance. The final geometry consists of a cell with a central hexagonal hole with tapered profile, developed using Preperm ABS1000 material with $\epsilon_r = 9.6$ and $\tan\delta = 0.02$. The structure has a size $L = 2.2$ mm $= 0.22\,\lambda_0$ at the design frequency $f_0 = 30$ GHz, and a thickness $H = 8.6$ mm $= 0.86\,\lambda_0$. The phase of the incident field can be compensated by varying the dimension of the internal hole diameter d in the range [0.9, 2.1] mm. This configuration delivers a full 360° transmission coefficient phase coverage, while its magnitude is never lower

than -3 dB across the Ka-band frequency range (29–31 GHz).
Consequently, the unit cell was adopted to design a lens with a diameter $D = 100$ mm $= 10\,\lambda_0$, and illuminated by a circular horn located at a focal distance $F = 124$ mm from the lens, so that $\frac{F}{D} = 1.24$. The results of the numerical analysis of this configuration confirm the effectiveness of the proposed lens structure.
Considering the need to minimize the volume occupied by the entire antenna, the F/D ratio is reduced to $\frac{F}{D} = 0.25$. In this case, the lens design must consider that it is in the near-field region of the feed.
Additionally, an analysis was conducted to evaluate the impact of relocating the feed from the position employed in the lens design on antenna performance. For its improving, a bifocal lens, engineered to enhance angular coverage and sustain a reliable link with moving satellites, all while minimizing the drop in gain, was also designed and analyzed. This research establishes a strong foundation for advancing satellite communication antenna terminals tailored to new applications in transportation, remote connectivity and autonomous communication systems. Upcoming initiatives will aim to enhance the surface design to ensure conical coverage while minimizing the mechanical complexity within the adopted configuration.

Table of Contents

List of Tables

List of Figures

Acronyms

6G

Sixth Generation

Wi-Fi

Wireless Fidelity

TA

Transmitarray Antenna

RA

Reflectarray Antenna

SatCom

Satellite Communication

SOTM

SatCom-On-The-Move

LEO

Low Earth Orbit

MEO

Medium Earth Orbit

GEO

Geostationary Earth Orbit

SNR

Signal-to-Noise Ratio

VSAT

Very Small Aperture Terminal

ESA

Electronically Steerable Antennas

ESPA

Electronically Steerable Phased Antennas

Ka-band

Kurz-above band (26.5–40 GHz)

Ku-band

Kurz-under band (12–18 GHz)

AM

Additive Manufacturing

EM

Electromagnetic

UAV

Unmanned Aerial Vehicles

FDM

Fused Deposition Modeling

SLM

Selective Laser Melting

UC

Unit Cell

UC1

First case of hexagonal Unit Cell

UC2

Second case of hexagonal Unit Cell

UC3

Third case of hexagonal Unit Cell

DXF

Drawing Exchange Format

STL

Stereolithography

CAD

Computer-Aided Design

SLL

Side Lobe Level

BLL

Back Lobe Level

Chapter 1

Introduction

1.1 Background and motivation

Satellite Communication on the Move (SOTM) has become an essential enabler for broadband connectivity across various mobile platforms, including land vehicles, aircraft, and maritime vessels. Historically dominated by geostationary (GEO) satellites, the field is undergoing significant transformation with the advent of Medium Earth Orbit (MEO) and Low Earth Orbit (LEO) satellite constellations. These next-generation systems offer distinct advantages: the shorter distance between user terminals and satellites substantially reduces end-to-end latency, often achieving under 50 milliseconds compared to several hundred milliseconds with GEO counterparts. Additionally, the reduced propagation distance allows for lower transmission power requirements, while multipath distortions are mitigated due to the favorable geometry and improved signal paths.

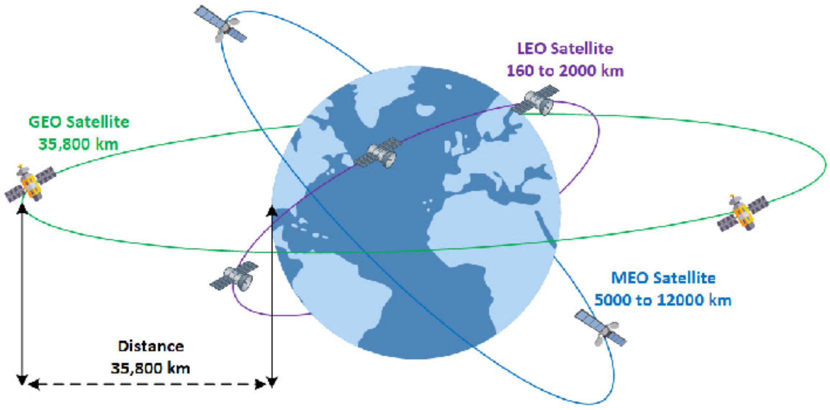

Figure 1.1: Satellite footprints for GEO, MEO, and LEO systems [1].

As illustrated in Figure 1.1, GEO satellites provide large, nearly static coverage areas, whereas "MEO and LEO constellations feature smaller, dynamic footprints that allow for higher spatial resolution and more localized service" [1]. Even if cellular networks and fiber-optic systems have progressed substantially, large portions of the global population—particularly in rural and isolated locations—still experience limited or nonexistent internet access. A study conducted in 2022 revealed that "approximately 2.9 billion individuals remained disconnected from reliable internet services, largely due to the inaccessibility of terrestrial networks" [2]. In this context, satellite systems, especially those deployed in Low Earth Orbit (LEO), offer a promising solution for these problems.

Despite the technical advancements, the usage of LEO and MEO satellites for SOTM introduces demanding requirements for terminal antennas. The main challenge comes from the environment in which the device is mounted. Since the antenna is installed on a moving platform, the propagation medium and the operating conditions are highly dynamic. Establishing and maintaining a reliable communication link therefore becomes complex, as it involves two points in relative motion: the mobile platform (such as an aircraft, ship, or vehicle) and the satellites in orbit. These antennas must operate in high-frequency bands like Ku or Ka (the latter being particularly appealing for high-capacity applications) and provide wide-angle beam scanning capabilities. The goal is to achieve a conical coverage of 60° with respect to the boresight direction. Furthermore, it is important to reach an antenna gain of approximately 30 dBi or higher in order to minimize the free-space path loss during the satellite communication links and comply with stringent regulatory standards.

Given the large distances between the ground terminal and the satellites, the transmitted signal is affected by a significant attenuation when it propagates through space. A sufficiently high gain is therefore essential to ensure that the received power remains above the sensitivity threshold of the receiver, maintaining an acceptable Signal-to-Noise Ratio (SNR) even under adverse propagation conditions. Current solutions, such as mechanically steered reflectors, radome-enclosed systems, and active phased arrays, can reach the required performance levels but are often hindered by drawbacks like excessive size, weight, power consumption, and high costs. Moreover, these solutions should also be low profile for the aerodynamic of the mobile platform on which they are installed. These limitations significantly reduce their suitability for civilian applications, where both economic and physical constraints are far more restrictive compared to those encountered in large-scale military or aerospace platforms. Civilian platforms, especially those targeting widespread deployment, struggle to accommodate the bulk and expense of large phased arrays or complex mechanical steering systems.

This emerging challenge motivates the study of alternative technologies that balance performance with reduced complexity. A possible solution consists of integrating a relatively small set of electronically controlled feed elements with a passive lens to enable beam steering and broad coverage without the prohibitive costs and complexities associated with fully active phased arrays.

Unlike metallic or hybrid structures, fully dielectric cells offer several benefits, such as reducing ohmic losses at high frequencies, including the Ka-band, and minimizing issues related to unwanted resonances or overheating. Additionally, "the absence of metallic components enhances wideband performance and boosts the antenna's power-handling capabilities, which are crucial for ensuring reliability and efficiency in satellite communications" [3].

Dielectric cells align perfectly with modern Additive Manufacturing (AM) techniques. "3D printing allows to obtain a rapid prototyping with a cost-effective production of complex geometries that might be difficult or impossible to achieve through traditional subtractive approaches" [4]. This adaptability reduces not only the design-to-prototype timeline but also enables the production of lightweight, compact and durable components ideally suited for integration into mobile satellite communication terminals.

Such approaches offer the potential to bridge the gap between today's premium technologies and the economic and operational needs of civilian and commercial sectors.

1.2 Objectives of the thesis

The objective of this thesis is based on the study of current technologies employed for SOTM applications, with the aim of identifying their limitations and the potential innovative solutions that are currently under development. The problem focuses on identifying feasible solutions for civilian applications that enable a balance between performance, complexity, and size. A possible solution explored in this research is based on a meta-lens antenna architecture, specifically tailored for SOTM applications in the Ka-band. The key concept is to utilize a simple feed array composed of a smaller number of electronically controlled elements, paired with a planar meta-lens positioned in close proximity to the feed. This arrangement minimizes the complexity of the control system and reduce the overall weight of the antenna, with the goal to obtain a wide conical coverage and high gain essential for dependable communication with LEO/MEO satellites.

An important aspect of the research is the implementation of a hexagonal lattice for the meta-lens discretization, which allows to obtain a lower phase error as it provides a "densely-packed array and a better aproximation of the circular displacement of the unit cells on the transmitarray" [5]. Through design and full-wave simulations on CST MWS, a case study of the system is proposed, based on the mechanical motion of the source in the near-field region of the lens.

1.3 Document Organization

The thesis is systematically structured into six core chapters. After the introductory section, Chapter 2 offers a comprehensive overview of contemporary SOTM antenna technologies. This chapter delves into their classification, operational principles, and associated trade-offs, with a particular focus on the challenges encountered in civil applications. Chapter 3 is dedicated to the overall aperture design, with the unit cell selection and the feed-to-lens configuration. Chapter 4 extends the analysis into the near-field region, discussing the adopted model and examining several case studies to validate it. Lastly, Chapter 5 presents design solutions aimed at achieving beam steering, discussing the advantages and limitations of the proposed approaches.

This structured organization ensures a coherent progression from theoretical foundations to practical implementations, with a clear understanding of the methodologies, analyses, and results that support the development of advanced transmitarray antenna systems.

Chapter 2

SatCom On-The-Move Antenna Technologies

2.1 Introduction

In recent years, satellite communication (SatCom) systems have transitioned from specialized infrastructures primarily utilized in military, maritime, and aerospace operations to significant facilitators of global broadband connectivity. This shift has been driven by advancements in SatCom-On-The-Move (SOTM) technologies, which are engineered to deliver high-throughput, dependable connectivity to mobile platforms, including vehicles such as cars and buses, as well as ships, aircraft, and unmanned systems.

The relevance of such solutions has increased significantly in the context of a global environment where terrestrial communication infrastructures are either inadequate or entirely absent in numerous remote areas.

The SOTM approach directly addresses this challenge through the integration of mobile terminals equipped with advanced antenna systems capable of sustaining continuous satellite communication even under conditions where both the platform and satellites are in motion. This innovation highlights different applications, including "civilian broadband access for mobile users, disaster response efforts, remote media broadcasting, telemetry for autonomous vehicles, and inflight internet services for air-based platforms" [6], as schematically illustrated in Fig. 2.1, which shows the main SatCom system segments from space to the end user. The antenna is an important component of these systems and must satisfy increasingly stringent demands in terms of beam steering, energy efficiency, compactness, and cost-effectiveness. Additionally, contemporary applications require lightweight devices with low-profile in order to guarantee a good aerodynamic of vehicles or aircraft in which they are integrated. Efficient power consumption is important as

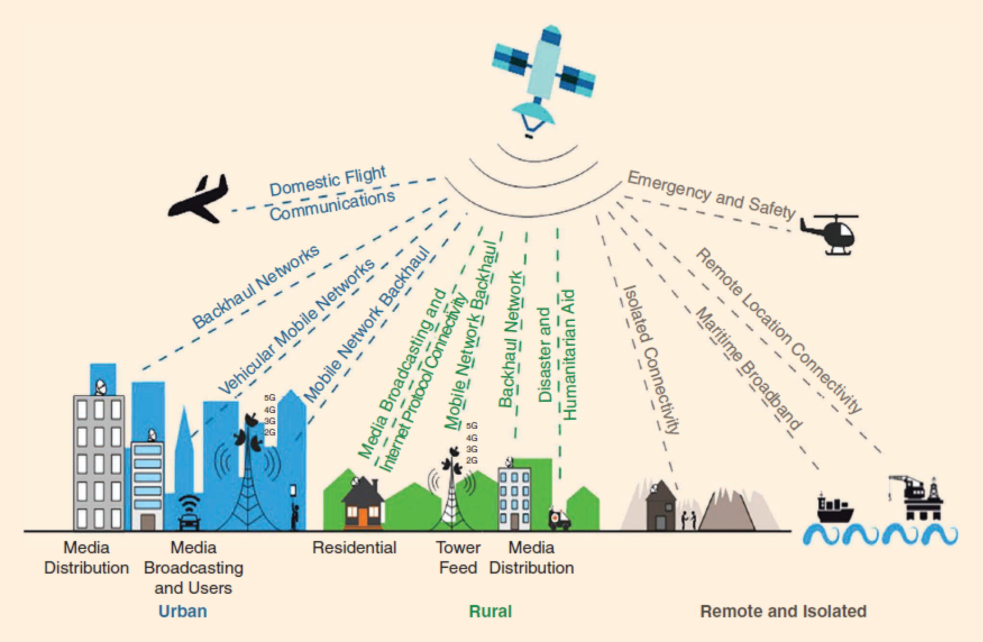

Figure 2.1: The SatCom system segments from space to user [6].

well, particularly for electric vehicles and off-grid operations.
Historically, "mechanically steered antennas—featuring parabolic reflectors mounted on motorized platforms—have been the standard solution for such needs. Despite their durability and high performance, these systems come with drawbacks such as bulkiness, significant weight, slow response times, and elevated costs, all of which limit their appeal in cost-sensitive civilian markets" [7]. Advances in technology have introduced Electronically Steerable Antennas (ESAs), flat-panel phased arrays and metasurface-based designs that provide a low-profile solution. "These innovations enable rapid, silent beam steering without relying on mechanical movement, enhancing reliability and adaptability for integrated deployments" [8].
At the system level, modern SatCom infrastructures are organized into three core segments [2]. These are schematically illustrated in Fig. 2.2 and can be classified as follows:

- The **space segment**, consisting of the satellite constellation (GEO, MEO, LEO);
- The **ground segment**, composed of network gateways, ground control stations, and backbone interconnections;
- The **user segment**, which includes all types of user terminals, including SOTM platforms such as aircraft, trains, maritime vessels, and land vehicles.

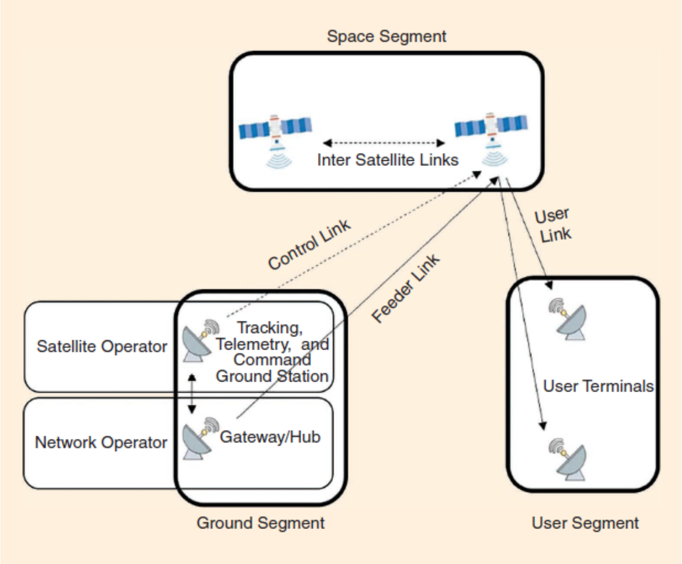

Figure 2.2: The SatCom system architecture [6].

Among these, the recent rise of LEO-based satellite constellations has profoundly reshaped the technical requirements of the user segment. These constellations— including initiatives like Starlink, OneWeb, Amazon's Project Kuiper, and Telesat Lightspeed— consist of hundreds to thousands of satellites moving in fast, low-altitude orbits. "This configuration ensures global coverage with minimal latency but simultaneously introduces new complexities: each satellite crosses a given location's field of view in just a few minutes, necessitating continuous tracking and rapid handovers from one satellite to the next" [2].
To fully understand these requirements, it is essential to examine the physical and operational characteristics of Low Earth Orbit. "Satellites in LEO operate at altitudes between approximately 160 km and 2,000 km, traveling at orbital speeds close to $7.8\,\mathrm{km\,s^{-1}}$. This velocity allows them to complete a full Earth orbit in just 90 to 120 minutes" [9]. LEO constellations are characterized by a relatively short distance from Earth with respect to traditional geostationary systems. The advantage is a lower propagation delay with reduced transmission losses, that allow to simplify the complexity of the terminal due to the lower power requirements. Moreover, since LEO networks consist of numerous satellites in continuous motion, they offer improved elevation angles and reduced multipath effects, particularly in urban or obstructed environments. Conversely, "GEO satellites, operating at approximately 36,000 km, demand larger and more complex antennas and exhibit much higher latency, which restricts their suitability for real-time or safety-critical applications" [10].
Table 2.1 summarizes the comparative characteristics of satellite constellations

across different orbital regimes, highlighting the inherent trade-offs between coverage, latency, and system complexity: while GEO satellites provide extensive Earth visibility with minimal infrastructure, LEO constellations enable low-latency communication at the expense of requiring a significantly larger number of satellites and more sophisticated tracking mechanisms.

Feature	GEO	MEO	LEO
Orbital altitude	∼36,000 km	∼8,000 km	∼1,000 km
Latency	Medium (∼700 ms)	Low (∼150 ms)	Very low (∼50 ms)
Earth view	Very large	Large	Small
Data gateways	Few, fixed	Several, flexible	Numerous, local
Antenna tracking	Stationary antennas	1-hour slow tracking	10-minute fast tracking
Satellites required for global coverage	3 satellites	6 satellites	Hundreds to thousands
Technology maturity	Proven, deployable technology	Proven, deployable technology	Technology still in development for satellite internet

Table 2.1: Comparison of satellite constellation characteristics at different orbital regimes [11].

However, these improvements come at the cost of increased system complexity. Satellites must constantly be tracked across the sky, requiring highly responsive beam steering and seamless handover mechanisms within user terminals. "Networks must handle a constant flux of active and inactive links, often implementing advanced multi-beam architectures, dynamic frequency reuse, and adaptive modulation to maximize throughput while minimizing interference" [2]. Terminals must therefore support fast beam steering, multi-beam connectivity, beam hopping, and polarization diversity.

As it can be observed in figure 2.3 the proliferation of thousands of LEO satellites in recent years raises concerns around orbital congestion, space debris, and electromagnetic interference. This exponential growth of low-orbit traffic calls for more stringent space traffic management and coordination to ensure sustainable use of orbital corridors. These concerns directly affect terminal design and are not just regulatory or environmental. "User devices must be capable of robust tracking in dense orbital environments and comply with strict emission and interference constraints, while still offering reliable performance in mobile scenarios" [10].

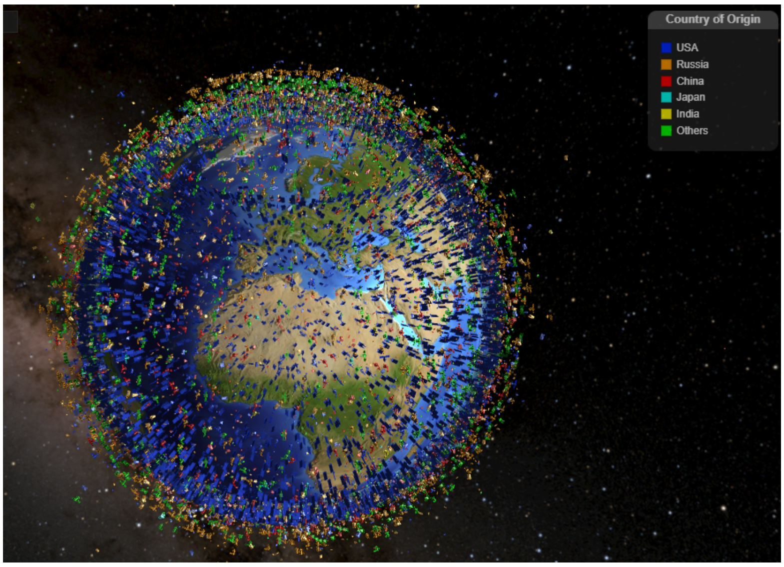

Figure 2.3: Global visualization of active LEO satellites.

Image credit: *LeoLabs, Inc.*. Visualization obtained from the Low Earth Orbit Visualization (LEOV) platform: `https://platform.leolabs.space/visualization`. Reproduced for academic and non-commercial use.

In this context, SOTM user terminals are no longer passive receivers but intelligent, adaptive nodes that play a central role in the success of the satellite network. Their capabilities must extend beyond basic reception to include real-time beamforming, proactive satellite tracking and dynamic spectrum coordination—especially as constellations become denser and more complex.

From a market perspective, a fundamental shift is underway. "SOTM technologies are expanding beyond traditional military and aerospace use cases to enter the civil mass market"[2], including :

- Public transportation (buses, trains);
- Emergency and disaster relief vehicles;
- Mobile news gathering and broadcasting;
- Connected and autonomous vehicles;
- Remote workstations and mobile offices;
- Maritime leisure and logistics;
- Aeronautical connectivity for commercial aviation.

These new markets demand terminals that are not only high-performance, but also affordable, scalable, and simple to install. "The entire SatCom value chain—satellite operators, equipment manufacturers, and research institutions—is now focused on developing lightweight, low-power, and cost-effective antenna technologies capable of operating in the Ka-bands or Ku-bands, supporting data rates upwards of 100 Mbps, and functioning under the power constraints of solar panels or vehicle batteries" [8].
For the purposes of this research, the terminal antenna system must satisfy the requirements listed in Table 2.2.

Feature	**Specification**
Operational Frequency	Ka-band or Ku-band
Scanning Range	Conical, with a semi-aperture angle of 60° from boresight
Gain	$\geq$ 30 dBi over the entire scanning range
Side-lobe Level	$<$ -15 dB
Polarization	Circular polarization (RHCP or LHCP) to ensure stable link performance regardless of orientation

Table 2.2: Key specifications of the antenna system.

This chapter provides a technical overview of the current SOTM antenna solutions, outlining the main types of beam-steering mechanisms, their trade-offs, and their suitability for modern platforms.

2.2 Classification of SOTM Antenna Systems

To address the diverse and challenging needs of SOTM systems, numerous antenna technologies have been introduced over the years. These technologies differ significantly in aspects such as beam-steering mechanisms, physical profiles, signal gain, cost efficiency, power requirements, and adaptability across various platforms. Although no single solution can be considered universally ideal. Understanding the primary categories can help in determining the most suitable technologies for specific applications.
A practical classification of SOTM antennas can be based on their physical characteristics, which broadly fall into two main families [8]:

1. Tall Dome Systems (mechanically steered reflectors);
2. Flat and Thin Systems (fully electronically steered or passive reconfigurable).

This section offers an overview of each category, describing their operating principles, strengths, limitations, and typical use cases.

2.2.1 Tall Dome Systems

The earliest and most widely recognized SOTM antenna systems are typically designed with a parabolic reflector housed within a protective radome and mounted on a motorized mechanism. This configuration facilitates precise azimuth and elevation tracking with a mechanical beam steering.
Such systems exhibit exceptional radiation characteristics, including high gain attributable to their large apertures, narrow beamwidth, and minimal sidelobe and cross-polarization levels. These features make them particularly suitable for demanding applications that require reliable performance in extreme conditions, such as deployment on military ground vehicles or naval platforms.

Figure 2.4: Antenna system designed for maritime applications [12].

The main limitation is their size and weight, often exceeding several tens of kilograms. The mechanical nature of their response mechanisms limits agility due to the inertia of the moving parts, while their height frequently exceeds the aerodynamic constraints imposed on many civilian vehicles.
The high manufacturing and operational costs of these antenna systems reduce their application in large-scale consumer markets.
Existing antenna systems include the "Cobham / Sea Tel family of stabilized VSAT antennas" [12]. An example of this class of products is the Sea Tel 3612, which is illustrated in Figure 2.4. This device is widely used in maritime and mobile

communication applications. It is engineered to comply with stringent standards for vibration and environmental resilience, ensuring reliable performance under demanding operational conditions.

In the land and defense domains, integrated stabilized terminals such as "General Dynamics' M20-20M series" [13] represent vehicle-mounted SOTM solutions that incorporate high-precision pointing mechanisms within reinforced enclosures, coupled with control and tracking electronics in order to maintain stable connectivity during dynamic motion.

Another important example is the "Cobham EXPLORER 9092M, a compact Ku/Ka-band terminal designed for continuous satellite connectivity on mobile platforms" [14]. Compared to traditional tall-dome architectures, this system has a reduced profile and weightand it is able to maintain high pointing accuracy with a fully stabilized gimbal mechanism. Despite these advantages, the 9092M is a high-cost solution, primarily targeted at defence, governmental and specialized industrial applications. It is not practical solution for widespread civilian deployment due to its elevated cost and maintenance requirements.

2.2.2 Phased Arrays

The most recent generation of SOTM antennas is represented by thin and flat electronically steered arrays (ESAs), which eliminate mechanical pointing mechanisms with a complete electronic beam steering. A phased-array antenna consists of multiple individual radiating elements whose relative phases can be electronically controlled. By adjusting the phase of each element, the antenna can rapidly steer the beam in a desired direction without any mechanical movement, with an optimal compensation of the platform motion. Their reduced profile makes them suitable for aircraft, ground vehicles, and maritime platforms, where aerodynamic drag and mechanical complexity are critical concerns.

The products described below represent commercially available solutions currently available in the market. Figure 2.5 illustrates the "Kymeta u8 terminal, operating in the Ku-band and based on metamaterial beamforming technology" [15]. Its standard version works in the Ku-band and it is able to provide a linear polarization with a coverage of 360° in azimuth and $[15°, 90°]$ in elevation. This architecture allows for fully software-defined electronic steering without any moving parts, maintaining a low profile with a total thickness below 10 cm.

Figure 2.5: Kymeta u8 flat panel antenna [15].

Beyond metamaterials, other innovative technologies have been developed to address the specific constraints of the new MEO and LEO constellations.

The solution proposed by ALCAN Systems consists of a thin and flat array working in the Ka-band, where a liquid crystal material encapsulated between two glass sheets separated by spacers is used to perform "2D scanning over a ±55° range" [16]. With a proper bias of the liquid crystal material it is possible to change its dielectric properties and "the antenna achieves a highly cost-effective design with a low power consumption of 98 W" [17].

A different technique to obtain beam scanning is employed by ThinKom Solutions, with the patented "Variable Inclination Continuous Transverse Stub (VICTS)" technology. "This approach combines the benefits of mechanically steered and electronically scanned arrays by controlling the steering and polarization through the rotation of lightweight discs around a single axis" [18]. Among the available configurations, the ThinSat Ka 500 is designed to be mounted on the rooftop of cars for land-mobile connectivity, while the Ka2517 series targets the aerospace sector, offering "high spectral efficiency and interoperability between LEO and GEO orbits" [19].

Another example of a fully digital architectures is presented by SatixFy with an innovative "Digital Beam Forming (DBF) technology" adopted in the "Onyx" Aero terminal [20]. It is an all-in-one solution based on two apertures for transmission and reception and it is able to work at different orbits with a very low profile.

All these systems represent the technological advantages of flat electronically steered arrays but are still complex and expensive for civilian applications.

Ranging from tall dome designs to flat configurations, each type of antenna is characterized by its own set of trade-offs involving performance, cost, complexity, and ease of integration, as summarized in the table 2.3.

Feature	**Tall Dome Systems**	**Flat and Thin Systems**
Beam Steering	Mechanical (gimbaled dish)	Fully electronic (phased array or metasurface)
Physical Profile	High (30–60 cm or more)	Low (<10 cm)
Gain	High (30–40 dBi)	Moderate
Steering Speed	Slow (seconds)	Fast (ms or μs)
Power Consumption	Moderate–High	Low–Moderate
Cost	High	Medium–High (scaling with technology maturity)
Typical Applications	Military vehicles, naval platforms	Cars, UAVs, aircraft, mobile platforms, consumer SatCom

Table 2.3: Comparison of mechanically stabilized tall-dome antennas and electronically steered flat/thin arrays for SOTM applications.

2.3 Proposed solution

A possible alternative solution consists of using a phased array with small size and reduced beam scanning capabilities, and a meta-lens, located in the near-field region of the array, used to focus the beam and eventually amplify the steering.
In order to realize a low-profile configuration, the lens must be positioned within the near-field region of the feed. The beam scanning capability is obtained through a combination of the source architecture and the controlled displacement of the lens with respect to it. Both the characteristics contribute to the overall steering performance. The lens developed in this work is based on the fundamental principles of transmitarray architectures, which are composed of an array of phase-shifting unit cells that manipulate the transmission phase of incident waves, reshaping the wavefront to achieve a targeted radiation pattern.
The adopted unit-cell topology is fully dielectric, characterized by high relative permittivity and low-loss in the material to ensure a reduced lens profile. A significant aspect of the design involves the employment of a hexagonal geometry. Unlike conventional square lattices, honeycomb structures can provide a better

discretization to guarantee a conical scan range. Additionally, the feed source is designed to be compact and structurally simple. The use of a 2 × 2 array of patch antennas can keep this complexity low, moving the design difficulty in the lens realization. The synergy between the feed and the lens designs allows to obtain a focused and steered beam toward specific spherical angles, maintaining high-gain performance. The feed source is placed at a focal distance F, while the lens diameter is denoted as D. The parameter $\frac{F}{D}$ is an important factor for the optimization of the system design, with typical values ranging between 1 and 1.2 in other case studies present in the literature. In order to limit the overall dimensions of the structure it is necessary to reduce this ratio.

In this work, the focus is on the lens design and a simple circular horn antenna has been selected as feed source. To achieve the overall design objectives, an initial detailed unit cell study was performed, succeeded by the analysis of the structure's performance under single-pointing configurations. To conclude, a design proposal is presented, demonstrating how the beam steering can be implemented through the controlled displacement of the feed source.

Chapter 3

Transmitarray Design

3.1 Introduction

A transmitarray (TA) antenna consists of an illuminating feed source and a thin transmitting planar surface that transforms the incoming wave into a desired outgoing one (as reported in Fig. 3.1).

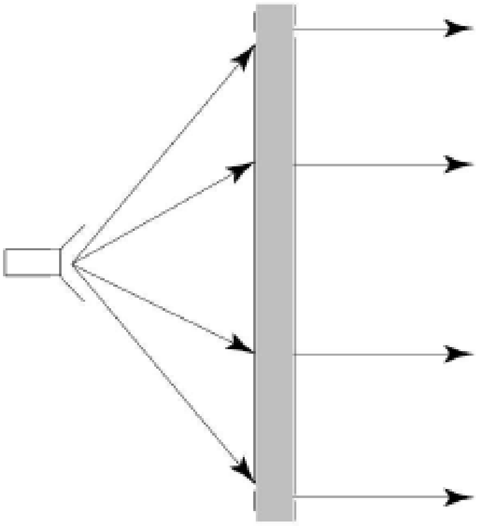

Figure 3.1: Transmitarray concept [22].

Thanks to its characteristics, which allow to exploit the advantages of lenses and phased arrays, the TA technology is a possible solution to be integrated in a low-cost antenna for satellite communication operating in Ku-band and Ka-band.
Compared to reflectarrays (RA), transmitarrays eliminate feed blockage and exhibit greater tolerance to surface errors. The analogy between the two systems is the

same as thhat between a lens and a mirror; while transmitarrays draw inspiration from reflectarrays, they introduce additional challenges.

As shown in Fig. 3.2, the reflectarray configuration relies on a metallic ground plane that ensures nearly total reflection, leading to a reflection coefficient $|S_{11}| \approx 1$. Consequently, only the reflected phase must be controlled. In contrast, a transmitarray must regulate both the magnitude of the transmitted wave, aiming for $|S_{21}| \approx 1$, and its phase $\angle S_{21}$ to properly compensate the phase of the incident field. It is possible to observein in Fig. 3.2 a systemic enlarged view of one of the transmitarray cells. It can be modeled as single-block system that introduces a delay $\Delta\phi(m, n)$ to the phase of the input incident field on the element, producing a controlled and shifted output that contributes to the creation of a focused beam.

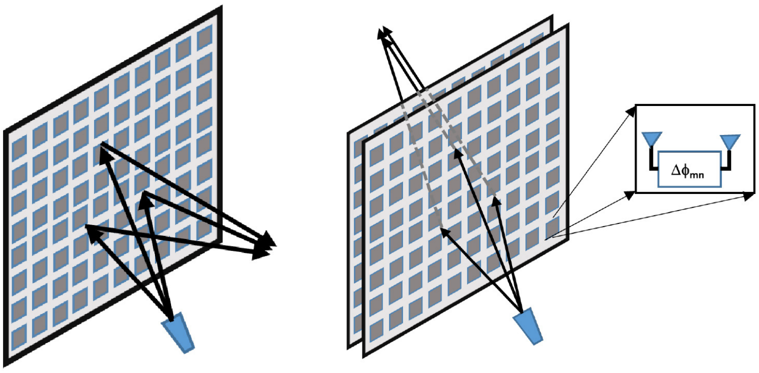

(a)

(b)

Figure 3.2: Illustration of **(a)** Reflectarray antenna and **(b)** Transmitarray antenna geometries [23].

3.2 State of the Art

In recent years, transmitarray antennas (TAs) have attracted growing attention in the scientific community due to their ability to combine the high gain performance of reflective antennas with the low-profile and design flexibility of planar metasurfaces. These surfaces are illuminated by a feeding antenna are essentially composed of subwavelength unit cells that introduce a specific phase delay to the transmitted wave. By properly engineering the phase distribution, it is possible to form highly directive and focused beams.

The theoretical framework for the design and analysis of transmitarray antennas was established by Abdelrahman *et al.* [22], who provided a detailed overview of the electromagnetic principles governing their operation. "Early transmitarrays were typically based on multilayer printed circuit structures capable of introducing a

360° transmission phase shift, although their operation bandwidth was narrow and they lacked electronic tunability. Gain and bandwidth enhancement remain the key research challenges in transmitarray development. Traditional designs exhibit strong frequency dispersion, leading to narrowband operation" [22].

A first contribution to the planar realization of transmitarrays was presented by Pozar in 1996 [22], who established the "receive-transmit" array concept. As illustrated in Fig. 3.3, this foundational unit cell is based on two microstrip patches located on opposite sides of a common ground plane. The energy is coupled between the patches with a slot and the phase compensation is obtained with the variation of the length of a delay line that connects the receiving and transmitting elements. The True Time Delay (TTD) effect exploited with this topology is able to provide an accurate phase control, but the adoption of transmission lines can introduce high insertion losses.

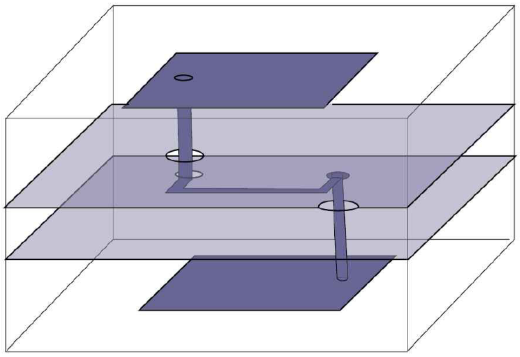

Figure 3.3: Geometry of the aperture-coupled microstrip unit cell based on a variable-length delay line [22].

Building upon the foundational receiver-transmitter principle established by Pozar, contemporary research has focused on reducing the volumetric footprint of these systems while introducing advanced polarization control. A notable evolution of this structure is the Circularly Polarized Double-Folded Transmitarray (DFTA) proposed by Li et al. [24].

While traditional TA require a significant focal distance, this design exploits a folded optical path in order to obtain a low-profile structure. The metasurface used in this architecture acts not only as a focusing lens but also as a polarization converter. Specifically, the system is fed by a linearly polarized source and the unit cells are able to apply the required phase shift with a transmitted circularly polarized waves. Experimental validation of this folded architecture demonstrated a peak gain of 21.8 dBic at 9.8 GHz. Despite the complexity of the double-folding mechanism, the prototype achieved a maximum aperture efficiency of 40% and a

-1 dB gain bandwidth of approximately 6%.

To overcome the bandwidth limitations and the fabrication complexity of via-based structures, Ryan et al. [25] proposed a distinct topological approach based on the Frequency Selective Surface (FSS) principle. This work represents a classic "scatterer-based" design and the unit cell is made of different dielectric layers with concentric double square rings as it can be seen in Fig. 3.4. The multi-layer structure is able to guarantee a wideband phase control without the need of metallized vias.

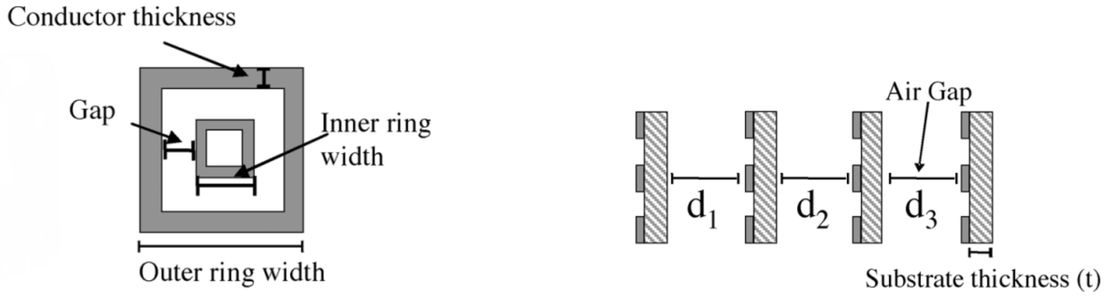

(a) **(b)**

Figure 3.4: Topology of the wideband transmitarray element proposed in [25]: **(a)** double square ring element geometry and **(b)** arrangement of the multilayer transmitarray stack-up.

The structure exploits a dual-resonant mechanism: unlike single square rings, the double-ring geometry excites two adjacent resonant modes. This interaction allows to expand the frequency behavior of the transmission magnitude with an almost linear phase response. Figure 3.5 shows the two results as a function of the inner ring width for the proposed four-layer structure. The analysis covers the frequency band from 28 GHz to 31 GHz. As illustrated, a phase tuning range exceeding 270° is consistently achieved at each frequency point across the bandwidth. Concurrently, the transmission magnitude is no lower than -1 dB within the operating range. The design exploits another similar unit cell configuration with a different thickness of the dielectric layers in order to cover the remaining phase range.

A fundamental understanding of transmitarray technology can be derived from the two analyzed implementations. The first configuration ensures phase precision and polarization agility but it suffers from significant ohmic losses and fabrication complexity due to the use of physical vias inside the structure. The second approach improves bandwidth performance but introduces mechanical challenges related to layer alignment and structural thickness.

The analyzed structures cannot reach the performance of phased arrays available on the market. They occupy a relevant volume and the beam is focused with a

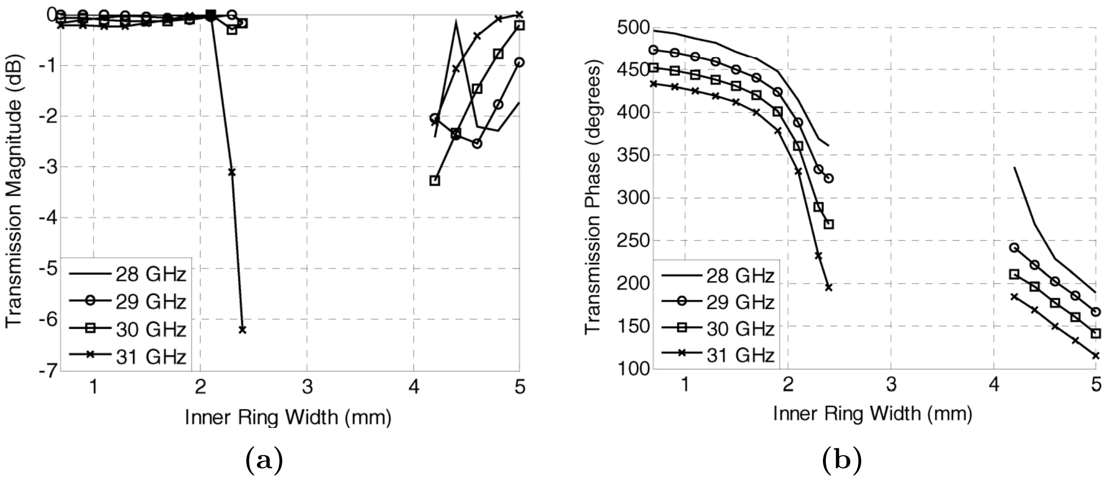

(a) **(b)**

Figure 3.5: Transmission phase **(a)** and magnitude **(b)** versus inner ring width for a four-layer structure for several different frequencies [25].

fixed pointing direction. Other case studies will be covered in Chapter 5, where the beam-steering mechanism implemented with this technology will be analyzed in detail.

In this context, the present work studies a simple antenna structure with an all-dielectric TA design rather than complex multi-layer architectures with metal components. The surface is completely passive and the elimination of conducting elements can reduce ohmic losses and fabrication costs.

3.3 Space-fed Array Design Method

The following subsection presents the design of a transmitarray antenna as reported in [22].
First of all it is necessary to analyze the phase distribution over the surface, with the selection of a suitable unit cells. Several analyses are then carried out starting from the discussed design theory, comparing the radiation results obtained through numerical simulations in CST Microwave Studio with those based on the well-known array theory model.

3.3.1 Phase distribution on transmitarray aperture

The fundamental assumption for establishing the theory under study is that the elements of the transmitarray are sufficiently distant from the source. This requires positioning the surface in the far-field region of the feed source, which is centrally located as illustrated in Figure 3.6.

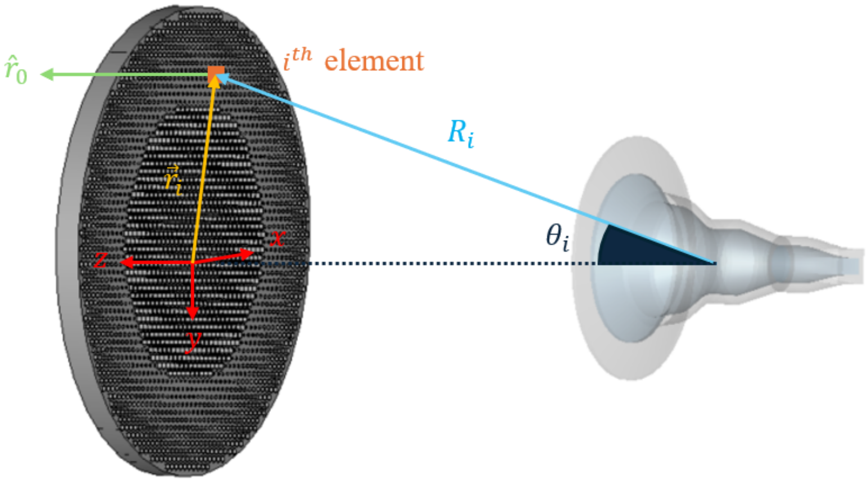

Figure 3.6: Phase compensation of a TA antenna.

Under these conditions, the incident electric field on each TA element can be locally treated as a plane wave traveling with a specific angle. Consequently, the phase of the incident field becomes directly proportional to the distance R_i from the phase center of the feed.
The core principle involves designing each unit cell of the TA such that its transmission phase precisely compensates the spatial phase delay between the feed horn and that specific element, directing the beam toward a desired angular direction.

Equation 3.1 establishes the required phase ψ_i to be applied to each unit cell of the transmitarray for an accurate focusing and steering of the transmitted wavefront [22]:

$$\psi_i = k\left(R_i - \vec{r}_i \cdot \hat{r}_0\right) + \psi_0 \tag{3.1}$$

- R_i is the distance from the feed to the i-th element;
- $\vec{r}_i \cdot \hat{r}_0$ represents the projection of the element position along the desired radiation direction;
- k is the propagation constant in free-space;
- ψ_0 is a reference phase, that can be arbitrary selected.

For large focal distances, the incident wave can be approximated as a plane wave and the required phase compensation varies slowly across the lens surface. In the case of compact and low-profile architectures the incident field can be seen as a spherical wavefront and the required phase distribution wrap around 360° multiple times over short distances. This geometric constraint necessitates the use of unit cells that provide full phase coverage (0° to 360°) in order to synthesize the required phase delay of the TA.

3.3.2 Unit cell definition

Independently from the technology used for its realization, UCs have a maximum size of $\lambda/2$ at the design frequency that in the present case is equal to 30 GHz.
Moreover, it is characterized by one or more geometrical free parameters that are used to control the unit cell performance, i.e. the amplitude and phase of S_{21} and the amplitude of the reflection coefficient S_{11}. What one would like to obtain is $|S_{21}| \approx 1$, $|S_{11}| \approx 0$ and $\angle S_{21}$ which varies almost linearly over a range of 360° as a function of the free parameter(s).
In order to realize these unit cells in practice, different fabrication techniques can be adopted, depending on the target frequency, desired phase range, and whether reconfigurability is required.
A possibility is to use fully dielectric unit cells. In this configuration, the cell behaves like a small refractive element: by shaping its geometry—such as varying thickness or introducing air holes— it is possible to control the phase delay of the transmitted wave. For example, Massaccesi and Pirinoli designed a three-layer dielectric unit cell with tapered layers in order to improve the air-matching [26, 27]. This type of cells can also be produced using 3D printing and AM techniques.
Another strategy is based on metallic resonators or patches with dielectric substrate. In this case the geometry of the metal and the gap between the layers determine

the phase shift of the transmitted wave. These unit cells can be easily fabricated using standard PCB processes. An example characterized by multiple dielectric layers was previously discussed with the study of Ryan et al. [25]. Sakurai et al. [28] demonstrated instead a simpler TA structure with two metallic patches separated by a single dielectric substrate.
In order to obtain a dynamic beam pointing, active components such as PIN diodes or varactors can be integrated within the unit cells. The surface can be seen in this way as an active device, able to modify electronically the phase of the transmitted wave. For example, Li et al. [29] proposed a unit-cell architecture that consists of a receiving element, a tunable phase-shifting network, and a radiating element. The field is redirected with the variation of the supply voltages of PIN diodes and varactors in the transmitarray, that allows a fast and programmable beam steering without mechanical movements.
Recent studies exploit more complex solutions in order to obtain the desired reconfigurability. For instance, Erdil et al. [30] demonstrated "a microfluidic X-band unit cell with nested split-ring resonators embedded in PDMS". The single elements of the TA can be rotated by displacing a liquid metal within dedicated channels. With this strategy it is possible to modify dynamically the geometry of the resonant structures.
Lastly, Phase-Change Materials (PCM) offer another way to achieve reconfigurability. Gharbieh et al. [32] presented a TA composed by "Phase-Change Materials" (PCM). These elements can switch between amorphous and crystalline physical states in response to an external pulse in the form of heat or voltage. The different properties of the material affect the transmitted electromagnetic wave, obtaining the desired phase modulation without moving parts.
Overall, the structure and fabrication technique of each unit cell strongly influence the performance of a transmitarray. In all the analyzed scenarios, structural degrees of freedom are utilized to obtain specific phase compensations of the transmitted field.

In this technological context, the proposed design employs a fully dielectric unit cell arranged in a hexagonal lattice. This configuration enables the implementation of a radially symmetric lens profile, which is particularly suitable for conical beam steering.
The study of a fully dielectric cell can lead to a significant simplification of the structure. "For transmission applications, the material's low-loss property is crucial to enhance antenna efficiency and reduce heating within the dielectric component" [3].
In addition to low losses, the material requires a high relative permittivity. The dependency can be obtained with the analysis of the phase delay introduced by a dielectric unit cell with a thickness H and a relative permittivity ε_r. This quantity

can be expressed as shown in Equation (3.2).

$$\phi = kH = \frac{2\pi}{\lambda}\, n\, H = \frac{2\pi}{\lambda}\, \sqrt{\varepsilon_r}\, H, \tag{3.2}$$

It is possible to identify two key parameters: the free-space wavelength λ and the refractive index of the material $n = \sqrt{\varepsilon_r}$.
Based on expression 3.2, the required phase delay can be set as ϕ_0, leading to the relationship between the cell thickness H and the material's relative permittivity ε_r expressed in Equation (3.3).

$$H = \frac{\phi_0\, \lambda}{2\pi\sqrt{\varepsilon_r}}. \tag{3.3}$$

With this formulation it is possible to conclude that materials with higher relative permittivity ε_r allow to reduce the unit cell thickness for a given phase compensation requirement.
The investigation considers the interaction between electromagnetic waves and the cell. The selected material is purely dielectric, specifically Preperm ABS1000, with initial properties of $\epsilon_r = 8.0$ and $\tan\delta = 0.0066$. Since different grades vary in filler type and quantity, alternative formulations were analyzed, leading to the adoption of a better filament with $\epsilon_r = 9.6$ and $\tan\delta = 0.02$.
This material exhibits minimal frequency dispersion, enabling effective wave propagation delay with the expected reduction of the component thickness due to its high permittivity characteristics. Additionally, the dielectric composite filaments are fully compatible with fused deposition modeling (FDM) technology.

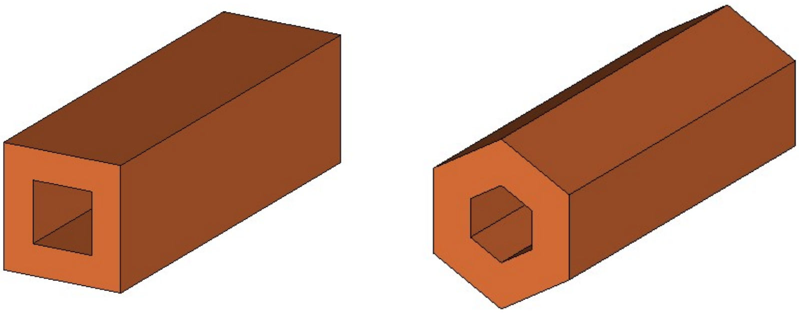

(a) **(b)**

Figure 3.7: Analyzed lattice configurations: **(a)** Squared UC, **(b)** hexagonal UC.

Figure 3.7 illustrates the two types of lattice configurations evaluated at this point of the research: rectangular and hexagonal. The rectangular lattice is frequently seen in literature-based solutions (e.g., [33], [34], [35]). "For innovation, inspiration was drawn from nature, where the hexagonal lattice geometry is employed" [36]. This unique design provides enhanced surface discretization, promoting uniform behavior radially from the structure's center.
The structure is seen as a symmetrical device and its behavior is analyzed when incident plane waves at varying angles θ reach one face of the cell. Considering the system a two-port equivalent structure, it is possible to analyze the behavior of the reflection (S_{11}) and transmission (S_{21}) coefficients. These scattering parameters are essential for the definition of the optimization objectives:

- Ensuring at least 360° coverage of $\angle S_{21}$, in order to achieve any desired phase compensation according to the project requirements.
- Maximize the transmission coefficient $|S_{21}|$ to reduce the attenuation of the incident electric field generated by the feed.
- Minimize the reflection coefficient $|S_{11}|$ to avoid undesired electromagnetic return disturbances on the array and to improve radiation efficiency.

These scattering coefficients depend on three major factors: the material, previously highlighted for its strong phase delay capability; the selected operating frequency centered at $f_0 = 30$ GHz with an analyzed bandwidth between 29 and 31 GHz; and structural dimensions, that influence ϵ_r with the manipulation of solid and void spaces. A key structural parameter d is varied across the surface to achieve the desired phase delays while leaving other parameters fixed. Pillar-shaped cells and more intricate geometries introduce additional degrees of freedom, intensifying optimization challenges as dimensional complexity increases. The unit-cells have been assumed to be embedded in a periodic lattice, including the effect of mutual coupling between the elements. However, due to limitations in CST Microwave Studio, periodic lattices are confined to square shapes. Consequently, the desired hexagonal configuration is approximated using a rhomboidal pattern derived using spacing values determined from the Law of Cosines (illustrated in figure 3.8 and 3.9).

$$c = \sqrt{a^2 + b^2 - 2ab\cos 120^\circ}$$

$$c = \sqrt{\left(\frac{L}{2}\right)^2 + \left(\frac{L}{2}\right)^2 - 2\left(\frac{L}{2}\right)\left(\frac{L}{2}\right)\cos 120^\circ}$$

$$c = \sqrt{\frac{(2L)^2}{4} + \frac{L^2}{4}} = \frac{\sqrt{3}}{2}L$$

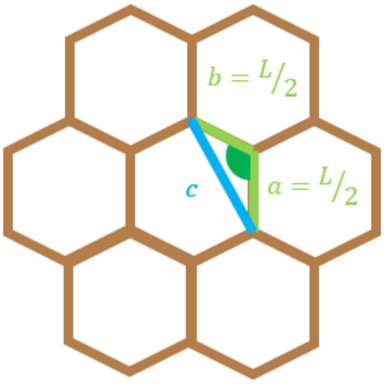

Figure 3.8: Hexagonal periodicity derivation.

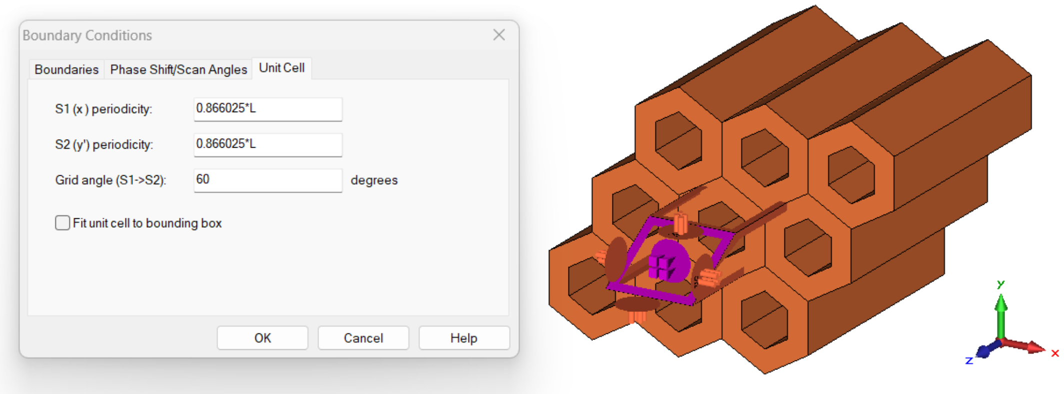

S1 (x) periodicity: 0.866025*L

S2 (y') periodicity: 0.866025*L

Grid angle (S1->S2): 60 degrees

☐ Fit unit cell to bounding box

Figure 3.9: Hexagonal grid setup.

Simulations were carried out using CST Microwave Studio to compute $|S_{11}|$, $|S_{21}|$, and $\angle S_{21}$ across frequencies from 29 to 31 GHz (Ka-band range) and incident angles spanning in the angular range $[0, 40]^\circ$. The lattice dimension L, correlating uniquely with each cell's height, was chosen near $\lambda_0/5$ to optimize performance while ensuring the structure's dimensions remain below $\lambda_0/2$. This constraint reduces diffraction effects and achieves an effective metasurface discretization with a complete 360° coverage of $\angle S_{21}$ without exceeding computational limits during simulations. In the following the optimized results of different unit cells with the first type of filament ($\epsilon_r = 8.0$ and $\tan\delta = 0.0066$) are presented. The choice of different structural configurations significantly affects the behavior of the scattering coefficients with respect to the variation of the free parameter d. The objective is therefore to identify the unit cell that provides the best overall performance, achieving optimal impedance matching along with wide transmission phase coverage.

Parameter	**Value**
Preperm ABS1000	$\epsilon_r = 8.0$, $\tan\delta = 0.0066$
L	$0.28\,\lambda_0 = 2.8$ mm
H	$0.67\,\lambda_0 = 6.7$ mm
d	$0.5 \text{ mm} < d < 2.7$ mm

Table 3.1: Case 1: Square hole, Parameters.

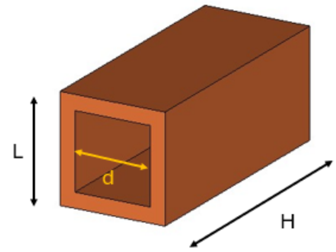

Figure 3.10: Case 1: Square hole, Unit cell structure.

Figure 3.10 shows the first analyzed unit cell configuration along with the selected dimensions in table 3.1. It consists of a simple square hole, designed to be implemented on a rectangular lattice. Figure 3.11 illustrates the reflection coefficient $|S_{11}|$ as a function of the free parameter d. A reasonably stable in-band behavior can be observed. Within the considered range, the curves exhibit two minimum values at approximately $d = 1.6$ and $d = 2.4$ mm, with values around -30 dB. At these points, the unit cell is optimized for minimal reflection, whereas the worst performance occurs for $d < 1.5$ mm, with a reflection of approximately -3 dB.
Figure 3.12 reports the behavior of $|S_{21}|$, which achieves optimal transmission values of about -0.3 dB only for maximum d values between 2.3 and 2.7 mm. The curve shows two minima, ensuring that for $d > 1.5$ mm the transmission remains above -3 dB for all angles of incidence, while reaching a minimum of -5.8 dB at the lowest frequency of 29 GHz for the minimum d value.
Figure 3.13 presents the trends of the transmission phase $\angle S_{21}$ as a function of the variable parameter d. A detailed analysis of the curves reveals a strictly monotonic increasing behavior characterized by a quasi-linear slope across the entire tuning range. This linearity is an important feature for the design process, as it ensures a uniform sensitivity to fabrication tolerances and allows for a straightforward inversion of the phase-to-dimension mapping. Furthermore, the unit cell exhibits excellent in-band stability and achieves an overall angular coverage of 370°.

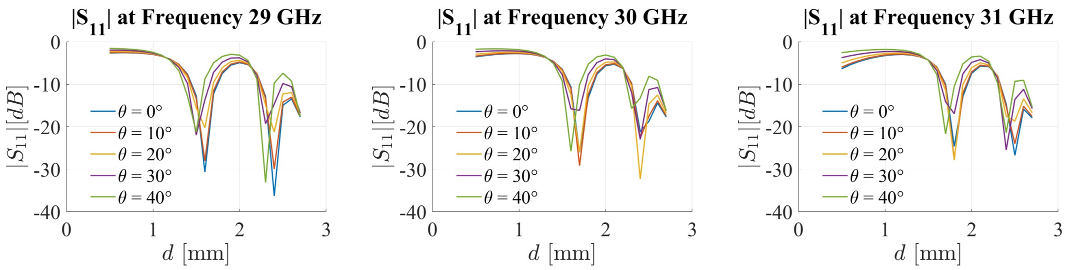

Figure 3.11: Case 1: Square hole. $|S_{11}|$ at 29, 30, and 31 GHz as a function of d and incidence angle θ.

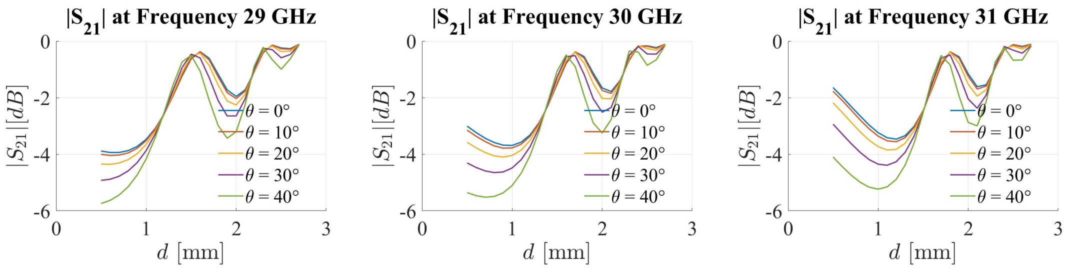

Figure 3.12: Case 1: Square hole. $|S_{21}|$ at 29, 30, and 31 GHz as a function of d and incidence angle θ.

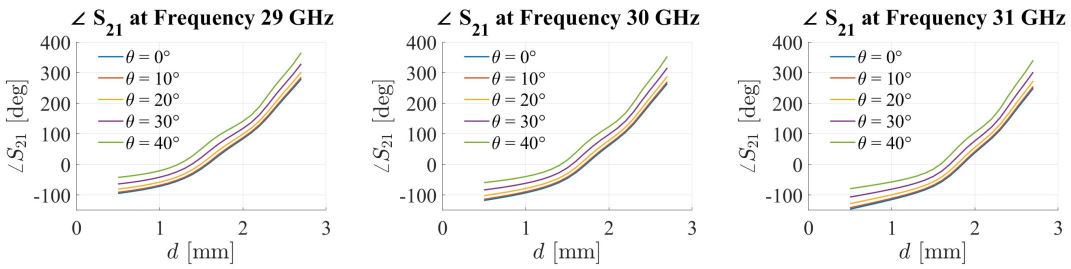

Figure 3.13: Case 1: Square hole. Phase $\angle S_{21}$ at 29, 30, and 31 GHz as a function of d and incidence angle θ.

The second studied configuration is shown in Figure 3.14, representing a hexagonal hole within a hexagonal lattice. The structural dimensions, as reported in table 3.2, are the same as those of the dual case with a square aperture. The behaviors in the frequency band of interest of $|S_{11}|$, $|S_{21}|$, and $\angle S_{21}$ as a function of d are reported in Figures 3.15, 3.16, and 3.17, respectively. As observed, the performance of the new configuration is comparable to that of the previously examined square-aperture unit cell. This equivalence is a crucial finding, as it confirms that the structural modification preserves the electromagnetic characteristics.

Parameter	**Value**
Preperm ABS1000	$\epsilon_r = 8.0$, $\tan\delta = 0.0066$
L	$0.28\,\lambda_0 = 2.8$ mm
H	$0.67\,\lambda_0 = 6.7$ mm
d	0.5 mm $< d <$ 2.7 mm

Table 3.2: Case 2: Hexagonal hole, Parameters.

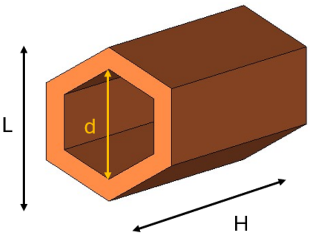

Figure 3.14: Case 2: Hexagonal hole, Unit cell structure.

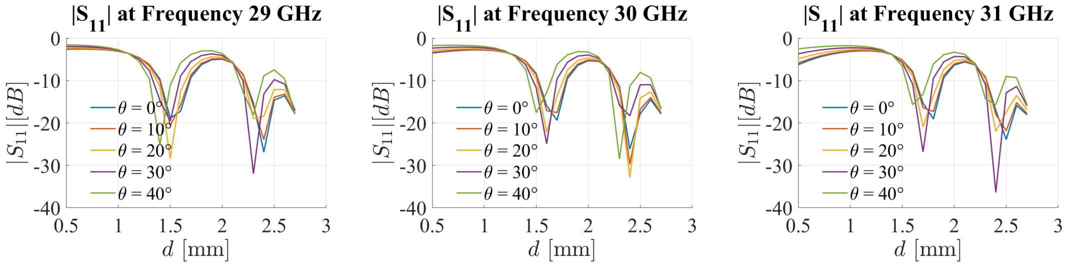

Figure 3.15: Case 2: Hexagonal hole. $|S_{11}|$ at 29, 30, and 31 GHz as a function of d and incidence angle θ.

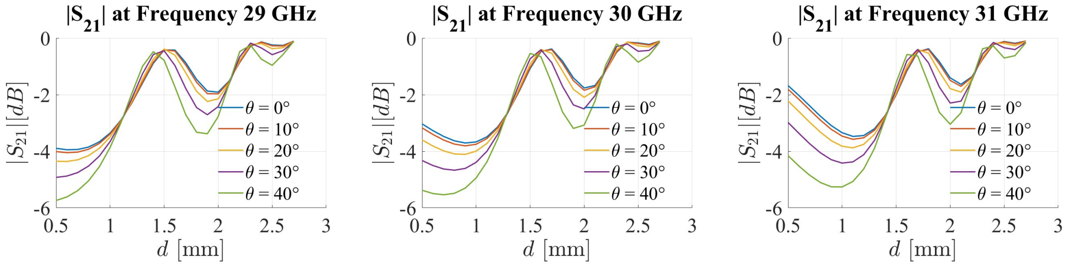

Figure 3.16: Case 2: Hexagonal hole. $|S_{21}|$ at 29, 30, and 31 GHz as a function of d and incidence angle θ.

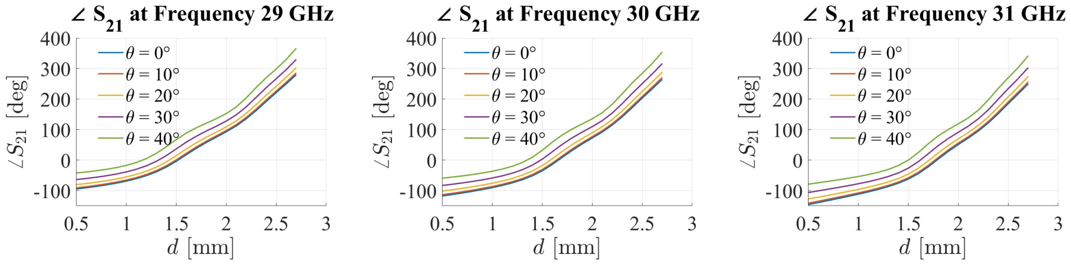

Figure 3.17: Case 2: Hexagonal hole. Phase $\angle S_{21}$ at 29, 30, and 31 GHz as a function of d and incidence angle θ.

Parameter	**Value**
Preperm ABS1000	$\epsilon_r = 8.0$, $\tan\delta = 0.0066$
L	$0.28\,\lambda_0 = 2.8$ mm
H	$0.74\,\lambda_0 = 7.4$ mm
H_c	$0.32\,\lambda_0 = 3.2$ mm
H_b	$0.10\,\lambda_0 = 1.0$ mm
d	0.5 mm $< d <$ 2.7 mm

Table 3.3: Case 3: Pillar in squared lattice, Parameters.

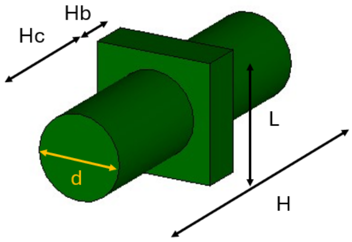

Figure 3.18: Case 3: Pillar in squared lattice, Unit cell structure.

The third unit cell case analyzed is shown in Figure 3.18. The structure consists of a pillar of height H_c with a circular base of diameter d. This diameter was selected as a free parameter with a variation in the range from 0.5 mm to 2.7 mm. To ensure greater structural rigidity and continuity of the entire surface, a square base with side L and depth H_b was added, resulting in a total thickness $H = H_b + 2H_c$. The dimensions of the unit cell, normalized with respect to the design wavelength (λ_0), are reported in Table 3.3.

Figure 3.19 shows the behavior of the reflection coefficient $|S_{11}|$, which remains around -2.5 dB for most of the d range, reaching a minimum of approximately -30 dB around $d = 2.5$ mm. Figure 3.20 reports the corresponding $|S_{21}|$ trends, which exhibit an optimal value of -0.5 dB only at the $|S_{11}|$ minimum previously identified. For the remaining portion of the free parameter d range, the transmission is generally below -3 dB, reaching a minimum of -5.2 dB at the smallest value of $d = 0.5$ mm.

Figure 3.21 presents the transmission phase curves within the band. These show a monotonically decreasing trend with minimal dependence on the incidence angle and a phase coverage of only 270°. This phase range is not enough for the practical usage of the studied cell in a TA surface.

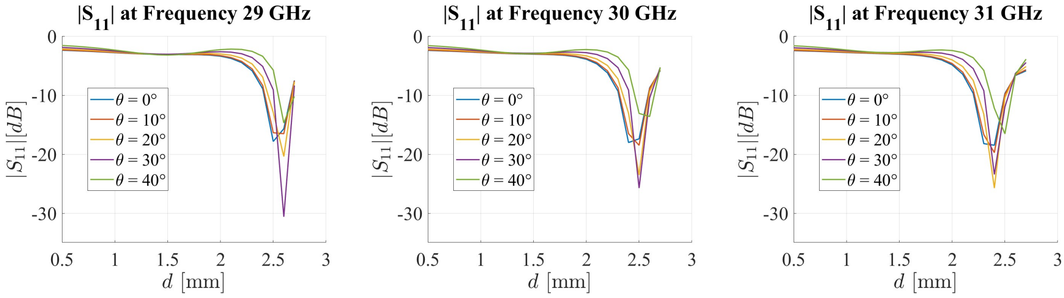

Figure 3.19: Case 3: Pillar in squared lattice. $|S_{11}|$ at 29, 30, and 31 GHz as a function of d and incidence angle θ.

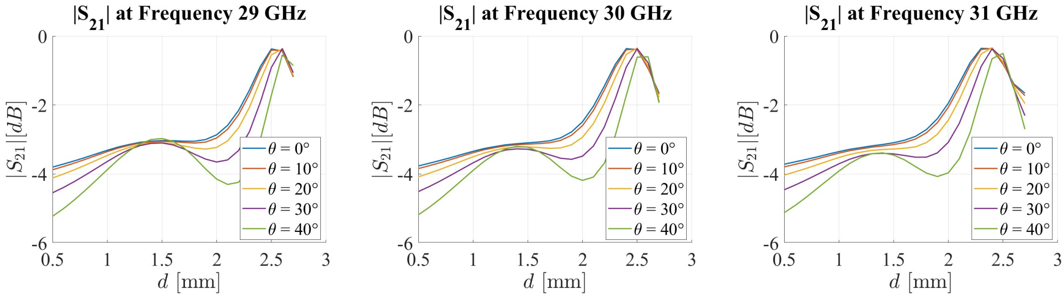

Figure 3.20: Case 3: Pillar in squared lattice. $|S_{21}|$ at 29, 30, and 31 GHz as a function of d and incidence angle θ.

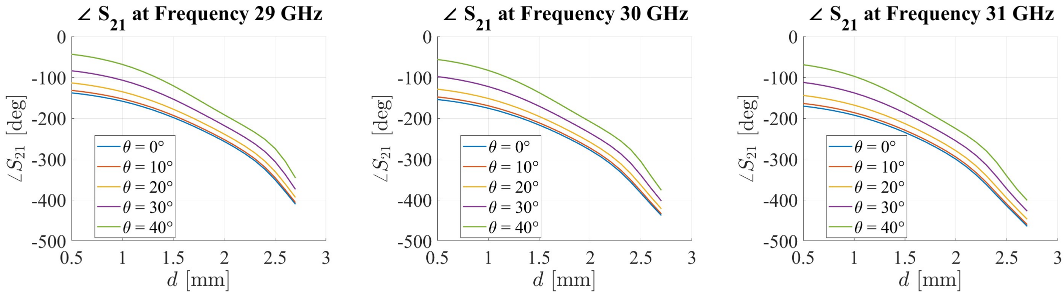

Figure 3.21: Case 3: Pillar in squared lattice. Phase $\angle S_{21}$ at 29, 30, and 31 GHz as a function of d and incidence angle θ.

Parameter	Value
Preperm ABS1000	$\epsilon_r = 8.0$, $\tan\delta = 0.0066$
L	$0.28\,\lambda_0 = 2.8$ mm
H	$0.74\,\lambda_0 = 7.4$ mm
H_c	$0.32\,\lambda_0 = 3.2$ mm
H_b	$0.10\,\lambda_0 = 1.0$ mm
d	0.5 mm $< d < 2.4$ mm

Table 3.4: Case 4: Pillar in hexagonal lattice, Parameters.

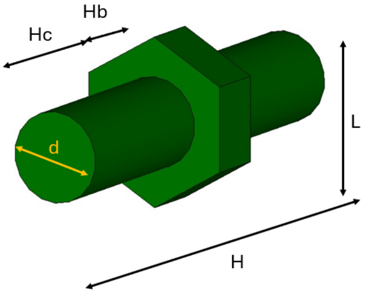

Figure 3.22: Case 4: Pillar in hexagonal lattice, Unit cell structure.

As previously studied, the analogous structure with a hexagonal base was also considered. Figure 3.22 shows the cell structure, and the selected dimensions are listed in Table 3.4. The configuration remains a pillar with a circular base of diameter d. The difference lies in the central component of thickness H_b, which is now defined as a hexagon inscribed in a circle of diameter L. Due to the new geometry of this cell component, the d variation range is limited to 2.4 mm.
As shown in Figure 3.23, the reflection coefficient $|S_{11}|$ remains constant at -3 dB, ensuring good matching for d values greater than 2 mm. The $|S_{21}|$ behavior, reported in Figure 3.24, is similar to the previously analyzed case. Efficient transmission with a coefficient of -0.5 dB is achieved only for $d = 2$ mm, with a second peak occurring at the higher frequency of 31 GHz.
The phase response $\angle S_{21}$, shown in Figure 3.25, is also monotonically decreasing, with a phase coverage of 320°. Although this represents an improvement over the square-base case, it remains insufficient for the TA design, where a full 360° phase coverage is required.

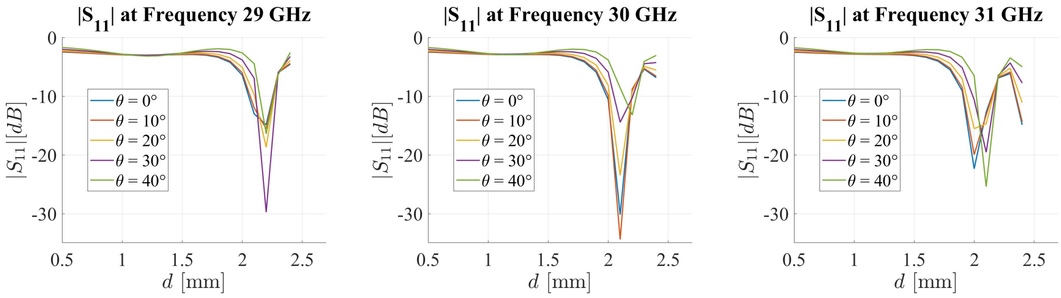

Figure 3.23: Case 4: Pillar in hexagonal lattice. $|S_{11}|$ at 29, 30, and 31 GHz as a function of d and incidence angle θ.

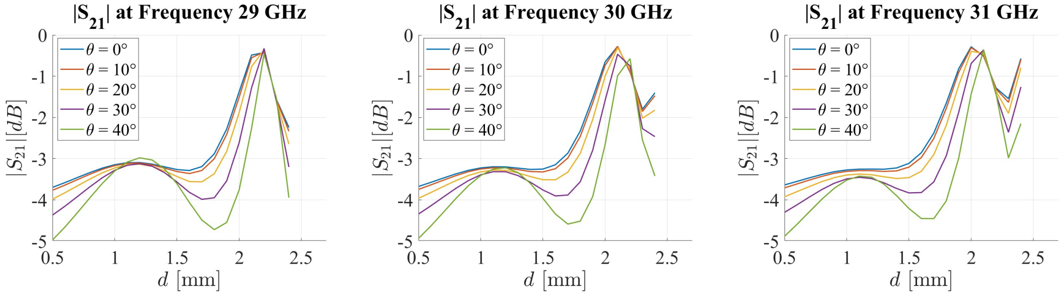

Figure 3.24: Case 4: Pillar in hexagonal lattice. $|S_{21}|$ at 29, 30, and 31 GHz as a function of d and incidence angle θ.

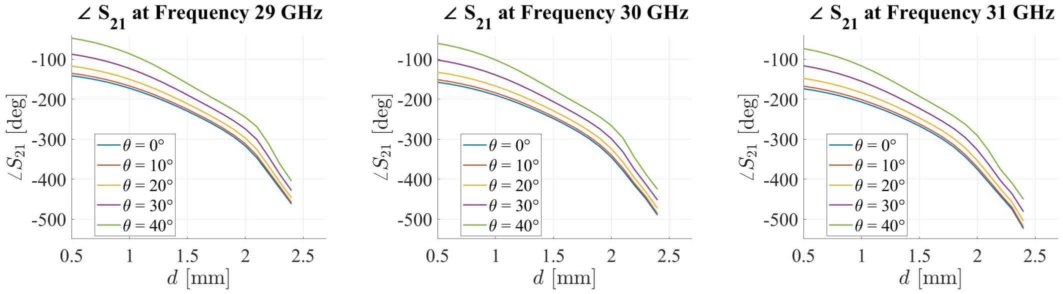

Figure 3.25: Case 4: Pillar in hexagonal lattice. Phase $\angle S_{21}$ at 29, 30, and 31 GHz as a function of d and incidence angle θ.

Parameter	**Value**
Preperm ABS1000	$\epsilon_r = 8.0$, $\tan\delta = 0.0066$
L	$0.28\,\lambda_0 = 2.8$ mm
H	$1.1\,\lambda_0 = 11$ mm
H_c	$0.45\,\lambda_0 = 4.5$ mm
H_b	$0.20\,\lambda_0 = 2.0$ mm
H_e	$0.13\,\lambda_0 = 1.3$ mm
cut	$0.04\,\lambda_0 = 0.4$ mm
d	0.5 mm $< d < 2.7$ mm

Table 3.5: Case 5: Tapered pillar in squared lattice, Parameters.

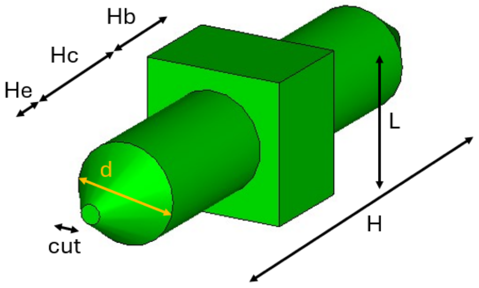

Figure 3.26: Case 5: Tapered pillar in squared lattice, Unit cell structure.

Starting from the analysis of the unit cell composed of a pillar, a further case study was conducted by introducing a tapering in the cylindrical structure. The configuration is illustrated in Figure 3.26, where the pointed profile imposed at both ends can be observed. The structural base has a square shape, while the pillar features a circular cross-section. As reported in Table 3.5, new design parameters

were added in addition to the previous ones, including the height of the tapered section H_e and the tip diameter *cut*. The total height of the structure is therefore given by $H = 2H_e + 2H_c + H_b$.
Figure 3.27 shows the behavior of $|S_{11}|$, which remains approximately constant up to $d = 2.5$ mm, where a good matching is achieved with a minimum peak value of about -35 dB. As the frequency increases, the constant portion of the curve rises from approximately -10 dB to around -5 dB. These values are improved compared to the previously analyzed configuration, mainly due to the introduction of the pillar tapering.
Figure 3.28 presents the variation of $|S_{21}|$ across the frequency band. The structure provides better performance compared to the previously studied cases, exhibiting transmission levels consistently above -3 dB throughout the entire d variation range. It is important to note that the power balance condition is always satisfied, as observed from the combined behavior of $|S_{11}|$ and $|S_{21}|$. For $d < 2$ mm, a good transmission of approximately -0.5 dB can be obtained at 29 GHz, while at the higher frequency of 31 GHz, a reduction to about -1.5 dB is observed. The transmission peak occurs for $d > 2.5$ mm, reaching a value of -0.5 dB.
The phase response $\angle S_{21}$ is shown in Figure 3.29. It exhibits a monotonically decreasing trend with a phase coverage of approximately 300°.

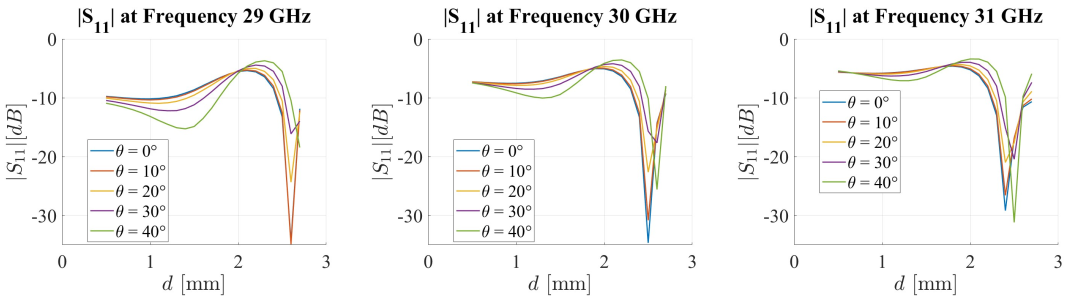

Figure 3.27: Case 5: Tapered pillar in squared lattice. $|S_{11}|$ at 29, 30, and 31 GHz as a function of d and incidence angle θ.

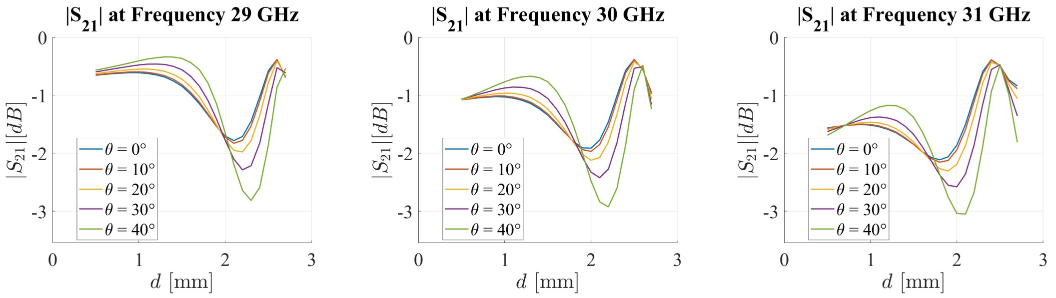

Figure 3.28: Case 5: Tapered pillar in squared lattice. $|S_{21}|$ at 29, 30, and 31 GHz as a function of d and incidence angle θ.

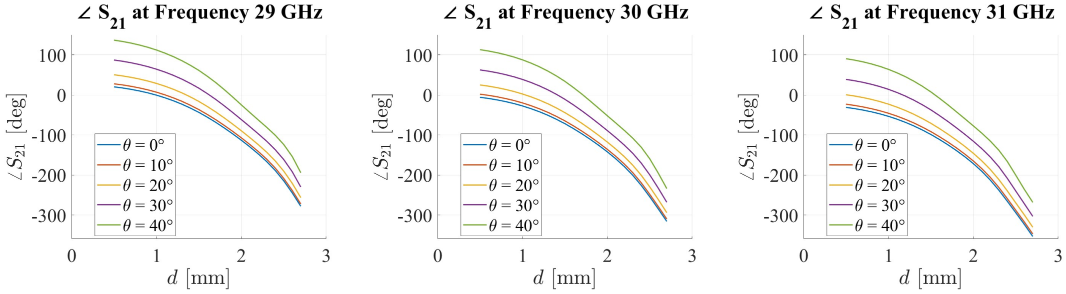

Figure 3.29: Case 5: Tapered pillar in squared lattice. Phase $\angle S_{21}$ at 29, 30, and 31 GHz as a function of d and incidence angle θ.

Parameter	**Value**
Preperm ABS1000	$\epsilon_r = 8.0$, $\tan\delta = 0.0066$
L	$0.28\,\lambda_0 = 2.8$ mm
H	$0.92\,\lambda_0 = 9.2$ mm
H_c	$0.42\,\lambda_0 = 4.2$ mm
H_b	$0.08\,\lambda_0 = 0.8$ mm
H_e	$0.10\,\lambda_0 = 1.0$ mm
cut	$0.02\,\lambda_0 = 0.2$ mm
d	0.5 mm $< d < 2.4$ mm

Table 3.6: Case 6: Tapered pillar in hexagonal lattice, Parameters.

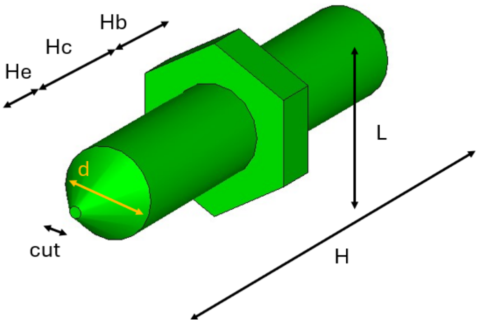

Figure 3.30: Case 6: Tapered pillar in hexagonal lattice, Unit cell structure.

The last analyzed configuration corresponds to the dual case of the previously discussed tapered-profile structure. As shown in Figure 3.30, it features a hexagonal base to enable the integration of the cell within a hexagonal lattice. The design parameters were re-optimized for this configuration and are reported in Table 3.6. The behavior of the reflection coefficient $|S_{11}|$ is presented in Figure 3.31. It remains constant at around -3 dB up to $d = 2$ mm, beyond which a better matching is achieved, showing a double minimum at higher frequencies. The magnitude of the transmission coefficient $|S_{21}|$, reported in Figure 3.32, assumes an absolute value of approximately -3.5 dB for $d < 1.7$ mm. For higher values of the free parameter ($d > 2$ mm), the transmission improves to around -0.5 dB. The phase response of this coefficient, shown in Figure 3.33, allows for an in-band phase coverage of approximately 360°.

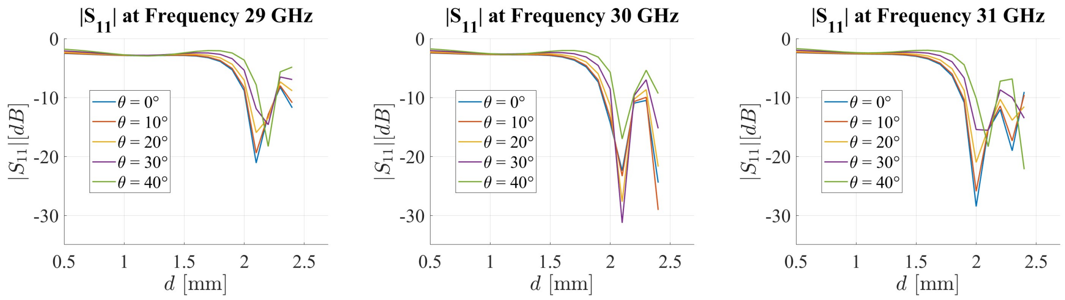

Figure 3.31: Case 6: Tapered pillar in hexagonal lattice. $|S_{11}|$ at 29, 30, and 31 GHz as a function of d and incidence angle θ.

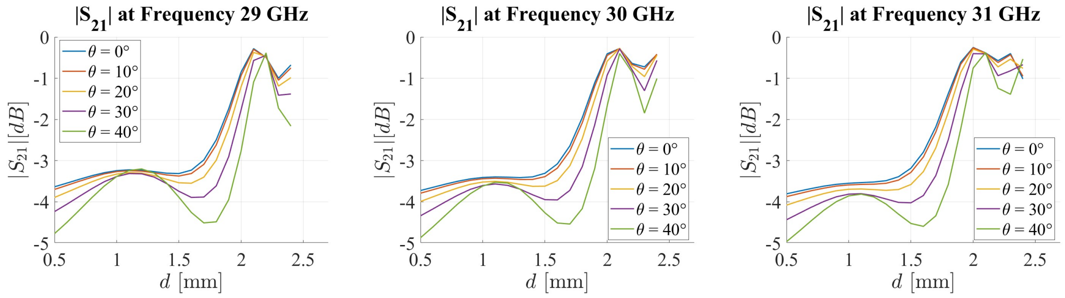

Figure 3.32: Case 6: Tapered pillar in hexagonal lattice. $|S_{21}|$ at 29, 30, and 31 GHz as a function of d and incidence angle θ.

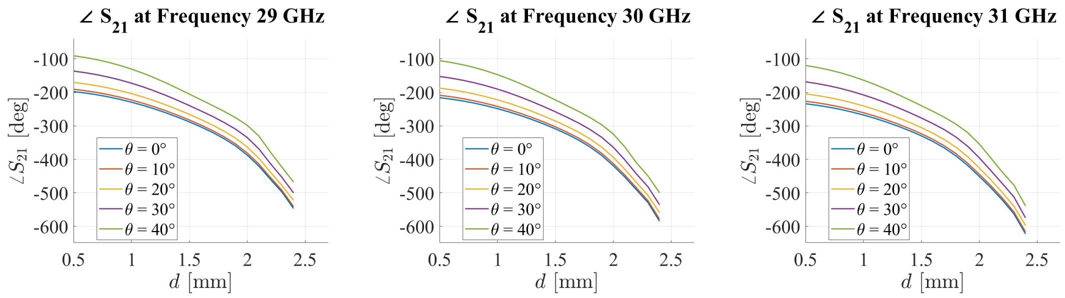

Figure 3.33: Case 6: Tapered pillar in hexagonal lattice. Phase $\angle S_{21}$ at 29, 30, and 31 GHz as a function of d and incidence angle θ.

The results presented above were obtained through an optimization process focusing on parameter sweeps of the structural dimensions, excluding the free parameter d. This variation of parameters led to distinct observations. Increasing the cell depth H enhanced the phase coverage range for $\angle S_{21}$ and significantly reduced the reflection coefficient $|S_{11}|$. However, this improvement came at the expense of the transmission coefficient $|S_{21}|$, which showed a notable reduction. Conversely, increasing the parameter L yielded no beneficial results, as it elevated $|S_{11}|$, diminished $|S_{21}|$ and restricted the phase range of $\angle S_{21}$.

In the study of pillar configurations the selection of the optimal structural parameters is more complex due to the presence of more degrees of freedom, including surface thickness H_b and cylinder height H_c. Adding tapering with depth H_e to the cylinder created a profiled geometry that improved air matching, effectively reducing $|S_{11}|$. This configuration also ensures a stable behavior for $|S_{21}|$, but it negatively affects the slope of the phase curves of $\angle S_{21}$. Consequently, the depth H reached values around $\lambda_0 = 10$ mm to meet angular coverage requirements, at the expense of size. As structural parameters expanded, the adopted optimization process increases its complexity, favoring simpler configurations like those with perforations. For cells of identical dimensions, scattering coefficients remain stable regardless of whether a rectangular or hexagonal lattice is employed, promoting the hexagonal design as an efficient choice to discretize the metasurface without loss in performance.

Furthermore, the results demonstrated low sensitivity to frequency variations and minimal dependence on incidence angles, considerations that will nonetheless be addressed to ensure high design accuracy. Based on these observations, hole-type cells were selected as promising candidates due to their structural robustness, minimal degrees of freedom that are easy to optimize, and straightforward compatibility with 3D printing using the FDM method.

Building on this analysis, the next step involved examining a hexagonal perforated cell —identified as the target configuration— realized with the available Preperm ABS1000 filament ($\epsilon_r = 9.6$ and $\tan\delta = 0.02$). As a consequence, in this study the free parameter d is the diameter of the internal hexagonal hole. The new optimization cycle of the parameters H and L enabled the identification of two reference cells for the design (hereafter denoted as UC1 and UC2).

They present a reduced height L on the order of $\lambda_0/5$, linked to the surface periodicity, which allows for a significant improvement of the scattering coefficients in agreement with the findings of the previous analysis. This value cannot be further reduced in order to mitigate the complexity of the metasurface discretization. Furthermore, due to the higher permittivity, this material enables the design goals to be achieved with a smaller thickness H with respect to the previously analyzed cases.

Parameter	**Value**
Preperm ABS1000	$\epsilon_r = 9.6$, $\tan\delta = 0.02$
L	$0.22\,\lambda_0 = 2.2$ mm
H	$0.55\,\lambda_0 = 5.5$ mm
d	0.5 mm $< d < 2.1$ mm

Table 3.7: UC1: Hexagonal hole, Parameters.

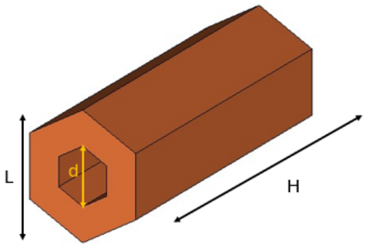

Figure 3.34: UC1: Hexagonal hole, Unit cell structure.

Figure 3.34 shows the simple structure of UC1, defined by the dimensions L, representing the side length of the hexagonal base, H, the cell depth, and the free parameter d, the diameter of the internal hexagonal hole. These values are listed in Table 3.7. Figure 3.35 illustrates the broadband behavior of $|S_{11}|$, which exhibits three minima corresponding to good impedance matching. These minima shift toward higher values of d as the frequency increases. Between the first and second minimum, the worst matching condition can be identified, corresponding to approximately –3 dB. The behavior of $|S_{21}|$, reported in Figure 3.36, shows peak values of –1 dB and –0.5 dB for larger values of d, while remaining above –5 dB across the entire operational range of the cell. The phase of this coefficient, shown in Figure 3.37, exhibits a monotonic increasing trend with respect to d, remaining relatively stable in frequency and with varying incidence angles. This configuration allows for a total phase coverage of approximately 360°.

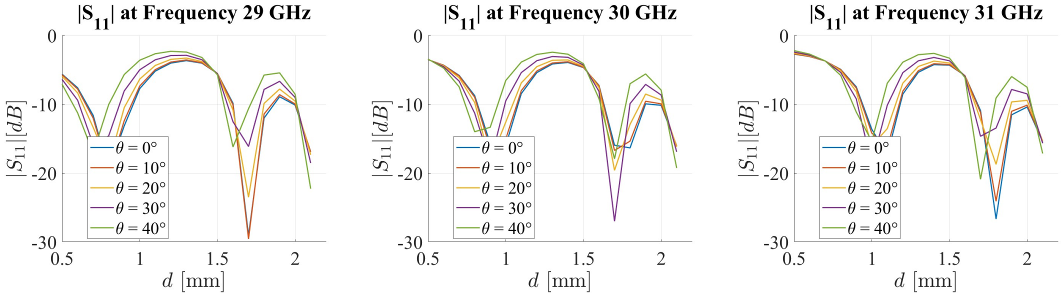

Figure 3.35: UC1: Hexagonal hole. $|S_{11}|$ at 29, 30, and 31 GHz as a function of d and incidence angle θ.

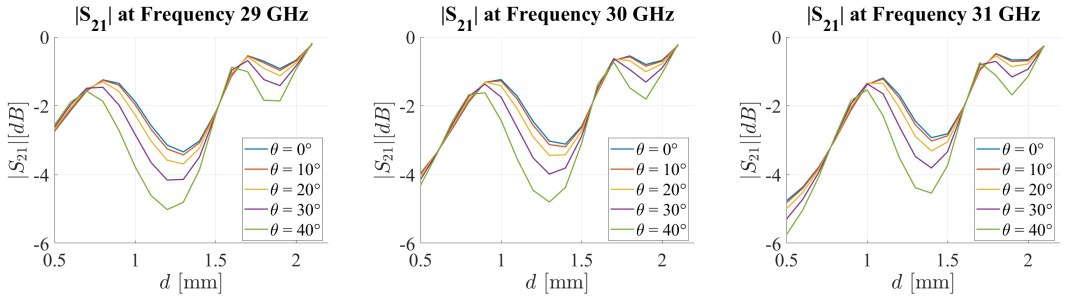

Figure 3.36: UC1: Hexagonal hole. $|S_{21}|$ at 29, 30, and 31 GHz as a function of d and incidence angle θ.

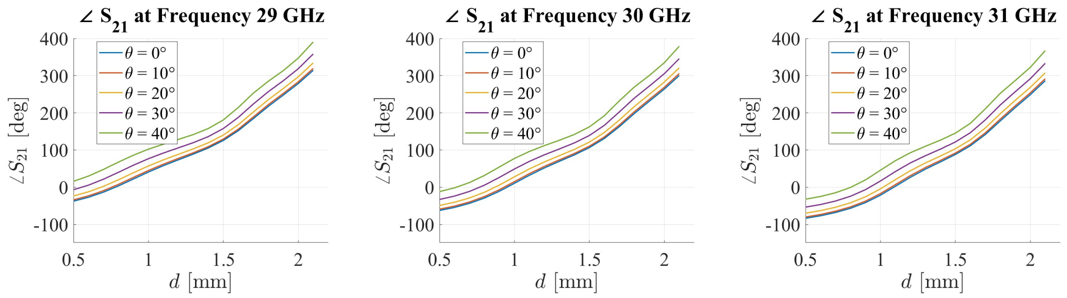

Figure 3.37: UC1: Hexagonal hole. Phase $\angle S_{21}$ at 29, 30, and 31 GHz as a function of d and incidence angle θ.

Parameter	**Value**
Preperm ABS1000	$\epsilon_r = 9.6$, $\tan\delta = 0.02$
L	$0.20\,\lambda_0 = 2.0$ mm
H	$0.65\,\lambda_0 = 6.5$ mm
d	0.5 mm $< d <$ 1.9 mm

Table 3.8: UC2: Square hole, Parameters.

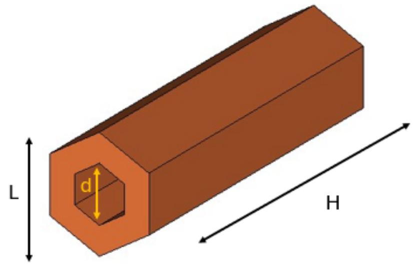

Figure 3.38: UC2: Square hole, Unit cell structure.

The second configuration under study, denoted as UC2, is illustrated in Figure 3.38. As reported in Table 3.8, it features a slightly greater thickness H and a smaller periodicity L. Figure 3.39 shows the entire variation of the coefficient $|S_{11}|$, which demonstrates good impedance matching for larger values of d. As in configuration UC1, three optimal points in terms of matching can be identified, particularly at higher frequencies. At lower frequencies and smaller d values, the worst matching condition occurs, corresponding to approximately –2 dB. The incidence angle marginally affects the behavior. Consequently, as illustrated in Figure 3.36, the worst transmission value of $|S_{21}|$ is around –6 dB for small d, with good transmission performance of –0.5 dB in the upper range of d variation. A better performance is achieved with low values of incidence angle. The total phase coverage of the transmission coefficient is approximately 390° with an almost linear behavior, as shown in Figure 3.37.

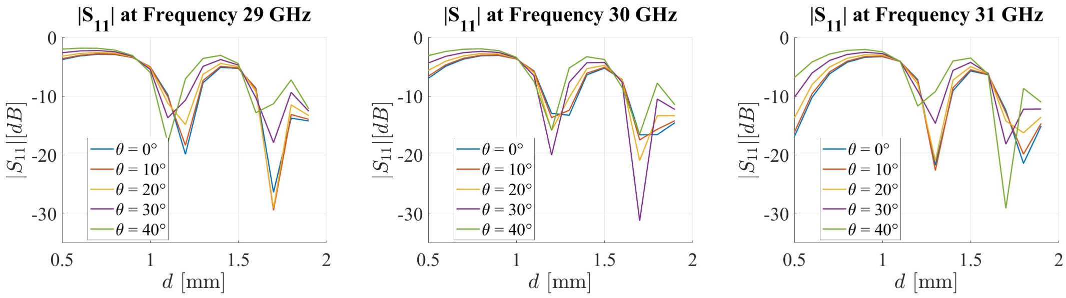

Figure 3.39: UC2: Square hole. $|S_{11}|$ at 29, 30, and 31 GHz as a function of d and incidence angle θ.

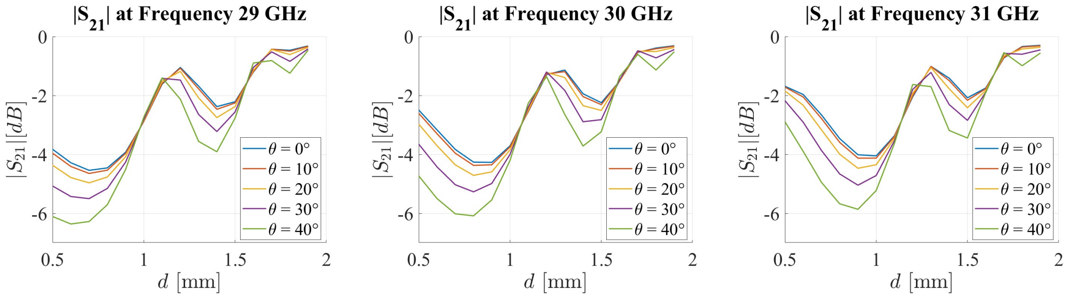

Figure 3.40: UC2: Square hole. $|S_{21}|$ at 29, 30, and 31 GHz as a function of d and incidence angle θ.

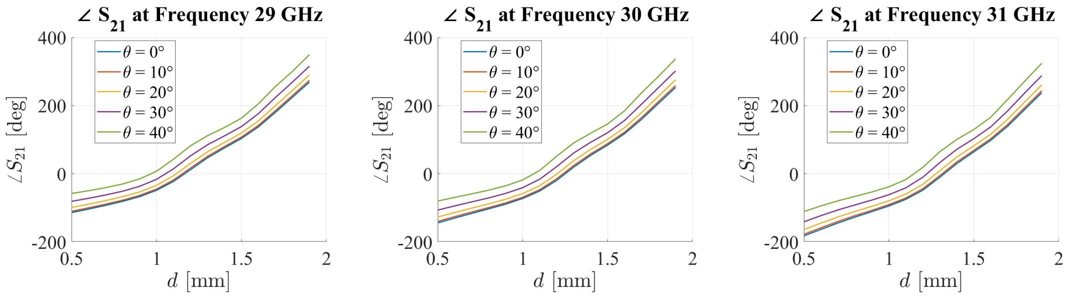

Figure 3.41: UC2: Square hole. Phase $\angle S_{21}$ at 29, 30, and 31 GHz as a function of d and incidence angle θ.

3.3.3 Optimization and final configuration

Starting from the two-unit cell results detailed in the previous section, further refinements can be introduced. These configurations are characterized by a uniform dielectric profile for the incident wave. According to transmission line theory, the bandwidth limitations of an impedance transformer can be addressed through the use of tapered transmission lines. By incorporating the design parameter H_e, which represents the recess depth, this enhancement can lead to an improved matching performance.

Consequently, the structure transitions from being viewed as a simple uniform dielectric to a three-layer unit cell. As previously indicated in the discussion regarding cylindrical unit cells, the introduction of an internal tapering to the hole significantly reduces $|S_{11}|$, enhancing the transmission efficiency of $|S_{21}|$. Additionally, meeting phase coverage specifications necessitates a slight increment of the thickness (H).

The free parameter is d, representing the diameter of the hexagonal hole of the intermediate layer of the structure. The external layers consist of hexagonal pyramids, where the larger base maintains a fixed diameter L and the smaller base is aligned with the internal diameter d for continuity. The height of each hexagonal pyramid correlates with H_e.

Parameter	**Value**
Preperm ABS1000	$\epsilon_r = 9.6$, $\tan\delta = 0.02$
L	$0.22\,\lambda_0 = 2.2$ mm
H	$0.86\,\lambda_0 = 8.6$ mm
H_e	$0.25\,\lambda_0 = 2.5$ mm
d	0.9 mm $< d < 2.1$ mm

Table 3.9: UC3: Tapered hexagonal hole, Parameters.

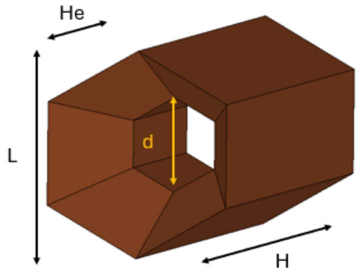

Figure 3.42: UC3: Tapered hexagonal hole, Unit cell structure.

In order to identify optimal values for the geometric parameters of the unit cells, a detailed analysis was performed by adjusting L, H, and H_e, reported in table 3.9. The resulting perforated unit cell, optimized through this parametric study, is illustrated in Fig. 3.42 and subsequently referred to as UC3.

Figure 3.43 shows the frequency response of $|S_{11}|$, which remains below -6 dB across the entire band. Optimal matching is achieved when d reaches its maximum value, as this configuration reduces the amount of dielectric material with a characteristic impedance closer to that of free space.

$|S_{21}|$ remains above -3 dB across all frequencies and angles of incidence covered by the analysis, as it can be seen in figure 3.44.

Finally, in figure 3.45 it is possible to observe that varying d within the range $[0.9; 2.1]$ mm yields a linear phase response capable of spanning approximately 390°. The data reveal low sensitivity to frequency variations and minimal dependence on the angle of incidence.

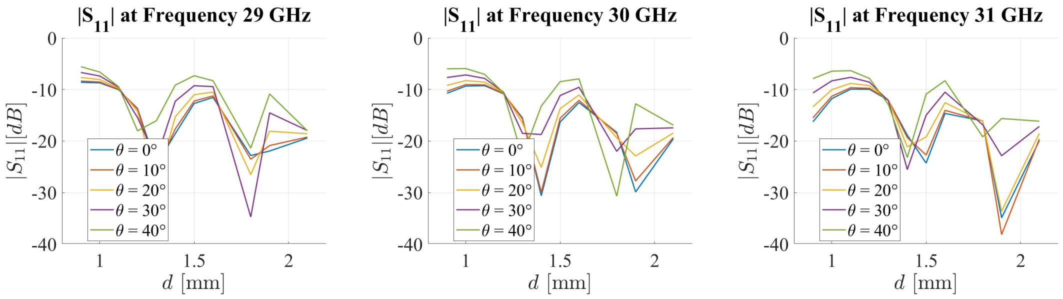

Figure 3.43: UC3: Tapered hexagonal hole. $|S_{11}|$ at 29, 30, and 31 GHz as a function of d and incidence angle θ.

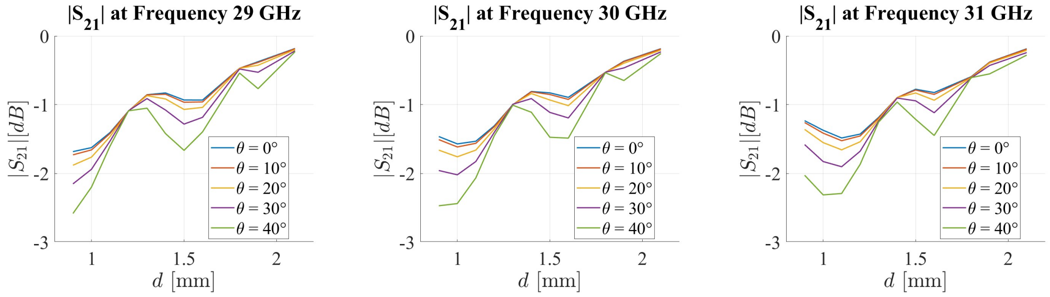

Figure 3.44: UC3: Tapered hexagonal hole. $|S_{21}|$ at 29, 30, and 31 GHz as a function of d and incidence angle θ.

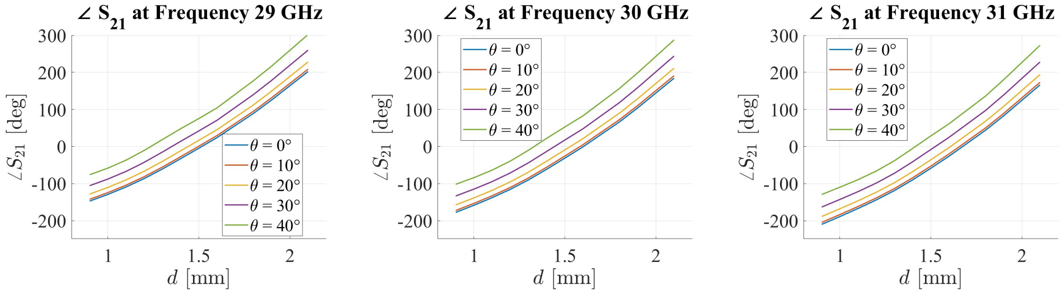

Figure 3.45: UC3: Tapered hexagonal hole. Phase $\angle S_{21}$ at 29, 30, and 31 GHz as a function of d and incidence angle θ.

3.3.4 3D modeling

Based on their characterized performance, the three cells, UC1, UC2, and UC3, will be employed as the fundamental building blocks for the corresponding transmitarrays evaluated in this work. These cells were initially designed in CST using simple geometric shapes such as cylinders and pyramids with hexagonal base, combined toghether to achieve their final profile. However, this design strategy cannot be directly applied to the metalens definition due to the unique parametrization required for each cell, determined by the variation of the free parameter d. To address this limitation, a more versatile approach is necessary—one that facilitates a straightforward and parametric modeling of the unit cells under consideration. To meet this requirement, two methods have been employed: generating `.dxf` or `.stl` files. These two 3D design methodologies are described in the Appendix, where their principles and implementation procedures are discussed in detail.

3.3.5 Unit Cell variable parameter selection

After determining the phase compensation required for each cell of the TA to achieve the intended pointing direction, the next step is to assign the corresponding free parameter d to each element. This process involves referencing the $\angle S_{21}$ curves obtained from the Unit Cell analysis detailed in the previous sections. These curves define the relation between the transmission phase and the free parameter range as a function of frequency and incidence angle θ, which varies based on the position of the i^{th} element. It is necessary to perform an inverse analysis, starting from the calculated phase values and proceeding backwards in order to obtain the corresponding geometrical value. At the reference frequency $f_0 = 30$ GHz, starting from discrete θ values ranging from 0° to 40° with a step of of 10°, interpolation techniques allow for the determination of the corresponding d values. An illustration of this process is provided in Fig. 3.46, which shows the phase plot of the unit cell configuration with tapered perforation UC3.

3.3.6 Criterion for Optimization

The relationship between the phase and the free parameter may lead to non-unique outcomes, primarily because phase curves exhibit a periodicity of 360°. As previously mentioned, the phase coverage of the Unit Cell UC3 spans approximately 390°. Due to the slope of these curves, in a worst-case scenario, two possible values of d could correspond to the same desired transmission phase ψ_i. This concept can be extended to accommodate a larger number of associations. The optimal selection strategy involves choosing the maximal feasible value of d, as increasing the inner cavity of the unit cell enhances the performance metrics S_{11} and S_{21}. This improvement is attributable to the reduced presence of dielectric material

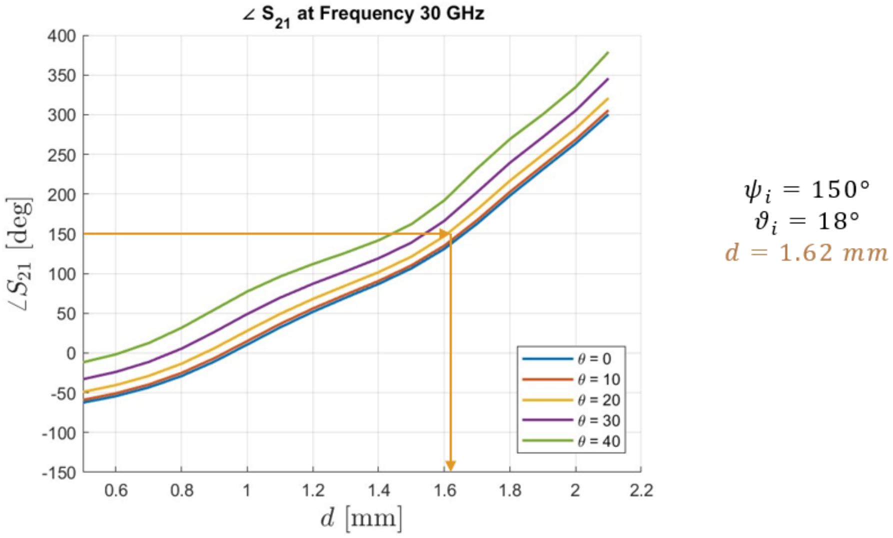

Figure 3.46: Case UC3: Example of determination of the free parameter d at $f_0 = 30$ GHz knowing θ_i and the required ψ_i of the i^{th} element.

within the cell, enabling better air coupling with reduced transmission losses. Optimization can also incorporate the arbitrary selection of the phase ψ_0, which effectively shifts the problem to higher values of the free parameter. However, this approach is constrained by the global behavior of the TA, as such compensation is uniformly applied across its entire surface.
In a TA with a diameter of $D = 10\lambda_0 = 100$ mm, the transmission phase across the surface does not fully span the 360° periodicity. This is not true with larger structures featuring a diameter of $D = 20\lambda_0 = 200$ mm, which are characterized by a complete and periodical phase coverage. In smaller configurations, it is possible to select a unique value of ψ_0 for each cell, optimizing the subrange of free parameters d utilized in the design process.

3.4 Radiation analysis using the array theory

The far-field radiation pattern of the transmitarray can be determined using conventional array theory. Specifically, for a 2D planar array comprising M×N elements, the radiation pattern can be computed as [22]:

$$\vec{E}(\hat{u}) = \sum_{m=1}^{M}\sum_{n=1}^{N} \vec{A}_{mn}(\hat{u}) \cdot \vec{I}_{mn}(\vec{r}_{mn}) \tag{3.4}$$

- $\vec{A}$: element pattern vector function;
- $\vec{I}$: element excitation vector function;
- $\vec{r}_{mn}$: position vector of the mn^{th} element.

In this setup, the coordinate system's origin is positioned at the center of the aperture, with the x and y axes situated on the aperture plane. A feed source illuminates the aperture plane from a height H above it. The feed source is offset and has its projection aligned along the y-axis. Consequently, the coordinates of the feed are $(0, -H\tan\alpha, -H)$, where α represents the offset angle.

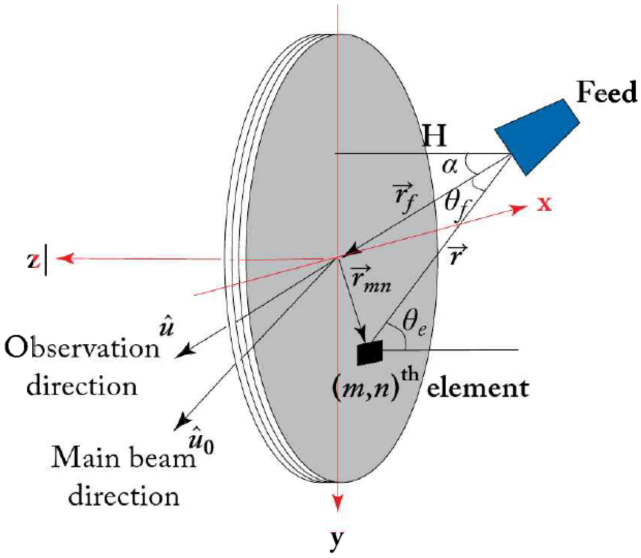

Figure 3.47: Coordinate system of the TA antenna [22].

The analysis depends on two principal factors, denoted as A and I, which encapsulate crucial information regarding the radiating element's characteristics and its interaction with the array itself, as represented through the array factor. For the sake of analytical simplicity, these variables are conventionally treated as scalar functions. Specifically, the element-pattern function A is modeled using a cosine-q formulation for each radiating component, assuming no dependence on azimuthal orientation.

$$A_{mn}(\theta, \phi) \approx (\cos\theta)^{q_e}\, e^{ik(\vec{r}_{mn} \cdot \hat{u})} \tag{3.5}$$

Here, q_e represents the power factor associated with the element's radiation pattern. Conversely, aperture illumination can be accurately approximated by employing another cosine-q modeling technique, which mirrors the feed horn's radiation pattern. This approximation further integrates the Euclidian distance between the feed horn and individual radiating elements to refine the representation of element excitation.

$$I(m, n) \approx \frac{(\cos\theta_f(m, n))^{q_f}}{|\vec{r}_{mn} - \vec{r}_f|}\, e^{-ik|\vec{r}_{mn} - \vec{r}_f|}\, |T_{mn}|\, e^{i\psi_{mn}} \tag{3.6}$$

- q_f : feed pattern power factor;
- $\vec{r}_f$: position vector of the feed;
- θ_f : spherical angle in the feed's coordinate system;
- $|T_{mn}|$: transmission magnitude of the mn^{th} element obtained from the unit-cell analysis;
- ψ_{mn} : required phase delay of the mn^{th} element to set the main beam in the $\hat{u}_0$ direction.

Building upon this model, the array analysis assumes periodic boundary conditions to approximate an infinitely large array. Such an approach enables an accurate consideration of mutual coupling effects between individual elements within the structure. Consequently, this formulation permits the simplification of Equation (3.4) into a scalar form that accommodates these interactions effectively.

$$E(\theta, \phi) = \sum_{m=1}^{M} \sum_{n=1}^{N} (\cos\theta)^{q_e} \frac{(\cos\theta_f(m, n))^{q_f}}{|\vec{r}_{mn} - \vec{r}_f|}\, e^{-ik\left(|\vec{r}_{mn} - \vec{r}_f| - \vec{r}_{mn} \cdot \hat{u}\right)}\, |T_{mn}|\, e^{i\psi_{mn}} \tag{3.7}$$

As previously addressed, the parameter F/D holds considerable significance in the design of a transmitarray. While this parameter does not explicitly feature in the governing equations, it has a direct impact on the phase distribution ψ_{mn} of the array elements, as well as their excitation levels $I(m, n)$.

3.5 Feed Antenna

To examine the preliminary transmitarray configurations, it is essential to choose a simplified version of the feed as the starting point. This method helps to establish the validity of the recently described mathematical design model while enabling a comparison of the array theory analysis with more detailed simulations conducted in CST software. For this purpose, the chosen feed is a circular horn that provides a gain of 17 dB at 30 GHz. It is described by a linear polarization and its geometry was defined through an optimization process performed at 30 GHz, as detailed in [37]. The three-dimensional representation of this structure is illustrated in Figure 3.48.

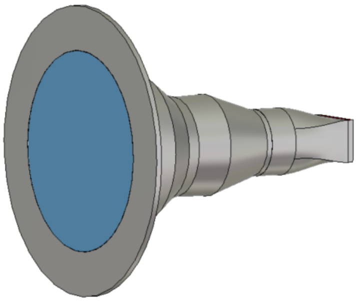

Figure 3.48: Circular horn antenna.

Its smooth-wall design was intentionally crafted for compatibility with the 3D printing employing selective laser melting (SLM). To facilitate antenna measurements, a WR28 rectangular-to-circular waveguide adapter is incorporated. The feed assembly measured 52 mm × 52 mm × 53.7 mm in total dimensions. The study in [37] simulated the horn using CST Microwave Studio and measured it in an anechoic chamber. Figure 3.49 compares measured and simulated radiation patterns in the ϕ-cuts 0° and 90° across the central, lower, and upper band frequencies. The strong alignment highlights the horn's manufacturing quality and its stable performance across frequencies.

These gain values as a function of the incidence angle θ will be used to provide initial constraints to the TA study, which will be discussed in detail in the next sections.

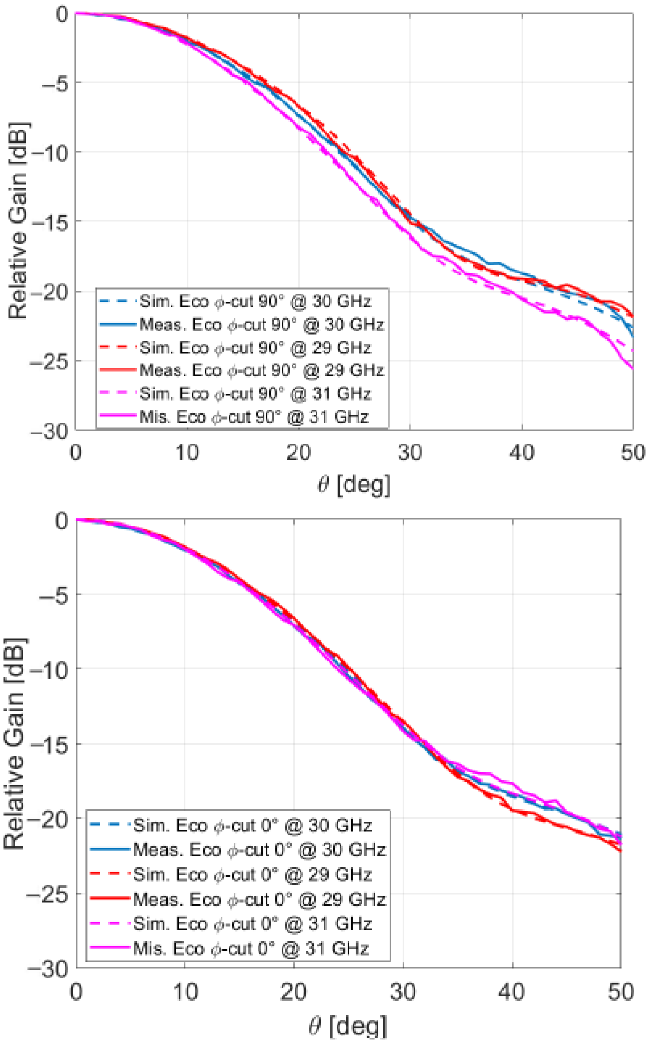

Figure 3.49: Radiation patterns of the optimized horn in the E (top) and H (bottom) planes for three frequencies within the specified band, based on measured and simulated data [37].

3.6 Fixed beam TA: Normal Incidence and boresight pointing with $\frac{F}{D} = 1.24$

After selecting the unit cells and the radiating element for the design, the TA theory described earlier is applied as a starting point. The initial focus involves analyzing three practical implementations of a circular metalens design. To simplify the simulations, the diameter of these structures is restricted to $D = 10\lambda_0 = 10$ mm at the design frequency $f_0 = 30$ GHz. The focal distance F is determined by examining the gain curves of the circular horn antenna depicted in Fig. 3.49. The selection of this distance must ensure a gain penalty no lower than -10 dB. Given that the gain curves are analyzed over a frequency range of [29, 31] GHz, the worst-case scenario at 29 GHz is used to calculate the maximum incidence angle. The gain remains relatively stable across the two reported ϕ-cuts, but the ϕ-cut at 0°, which demonstrates a steeper negative slope, is prioritized. From this evaluation, a maximum incidence angle at the edges of the metalens $\theta = 22°$ is identified as a suitable compromise in order to maintain the gain above -10 dB. Using straightforward geometric principles, the corresponding focal distance F satisfying this condition is derived.

$$F = \frac{\frac{D}{2}}{\tan\theta} = \frac{50\ mm}{\tan 22°} = 123.75\ mm \tag{3.8}$$

Thus, the maximum incidence angle, consistent across all three designs, is determined to be $\theta_{\max} = 21.54°$. To finalize the model configuration, the values of q_e and q_f are both set to 12.5 to achieve an optimal profile for the cosine factors present in the radiation formulas. The feed source is subsequently positioned at a negative z-coordinate along the predefined distance F in relation to the reference system (Fig. 3.47), centrally aligned with the TA. Given the chosen diameter and focal length, this yields a value of $\frac{F}{D} = 1.24$, which is comparatively large relative to previous studies but serves well as an initial basis for qualitative analysis.

The quantity $|S_{11}|^2 + |S_{21}|^2$ is finally evaluated in order to analyze the loss behavior of each unit cell. As well known, for an ideal lossless system, power conservation requires that the sum of the squared magnitudes of the scattering parameters is equal to one:

$$|S_{11}|^2 + |S_{21}|^2 = 1. \tag{3.9}$$

If the relation above results in a value lower than unity, the discrepancy can be attributed to dissipative mechanisms like in our case dielectric losses. This analysis provides a first-order estimate of the efficiency of the unit cells and enables a comparison between different geometries.

The subsequent section introduces additional analysis steps, including phase error evaluation, before summarizing results obtained from testing unit cell types UC1, UC2, and UC3.

3.6.1 Phase Error Introduction

An additional design consideration involves the integration of a phase error during the TA development. This adjustment reduces the free parameter range, refining it from the full interval assessed in the unit cell analysis. Optimization of the transmission parameter S_{21}, whose behavior reveals minima unsuitable for use, can be done with a proper definition of the subranges of d.

The procedure identifies the phase compensation required by each cell, starting from equation 3.1. After determining d via interpolation and inversion, its value is verified against the established subinterval. If d lies within permissible limits, no modifications are necessary; otherwise, it is positively saturated until it aligns with the nearest upper value within the constraints.

Saturation of the free parameter alters its transmission phase, introducing localized phase errors. These deviations are not analytically correct and influence radiation performance and losses. Their impact is then compared against results from the original system to evaluate their effects comprehensively.

3.6.2 TA design using UC1

In the initial study, the surface behavior was examined using the unit cell UC1 as the fundamental structural element. A total of 2395 elements were used to discretize the surface. The standard analysis involved evaluating the variation of the free parameter within the range $d \in [0.5, 2.1]\,\text{mm}$. To calculate the transmission phase, a reference value of $\psi_0 = 50°$ was employed to maximize as extensively as possible the distribution of high values of d over the surface.

The CST-based design is illustrated in Figure 3.50a, with its layout derived from the transmission phase values computed for each cell (Figure 3.51a).

The resulting radiation pattern at the operating frequency $f_0 = 30\,\text{GHz}$ is presented in Figure 3.50b, where predictions from the analytical model—built on array theory—are compared with CST simulation results. Notable consistency between the two approaches is observed, evidenced by the main beam being well-focused toward the broadside direction and sidelobe levels remaining below $-15\,\text{dB}$.

For further enhancement of global transmission, an alternative lens design was developed by introducing a controlled phase error. In this modified approach, two separate ranges were considered: $d \in [0.8, 1.1]\,\text{mm}$ and $d \in [1.6, 2.1]\,\text{mm}$. With these sub-ranges $|S_{21}|$ is no lower than -3 dB for all frequencies and incidences. The resulting phase error relative to the standard design is illustrated in Figure 3.51b. Optimization in the central part of the surface led to minimal deviations between the two models within this inner region. However, more pronounced phase discrepancies were observed near the edges of the transmitarray, where absolute phase differences reached up to 90° compared to the standard configuration.

Multiple cut planes were analyzed to evaluate the effectiveness of the applied

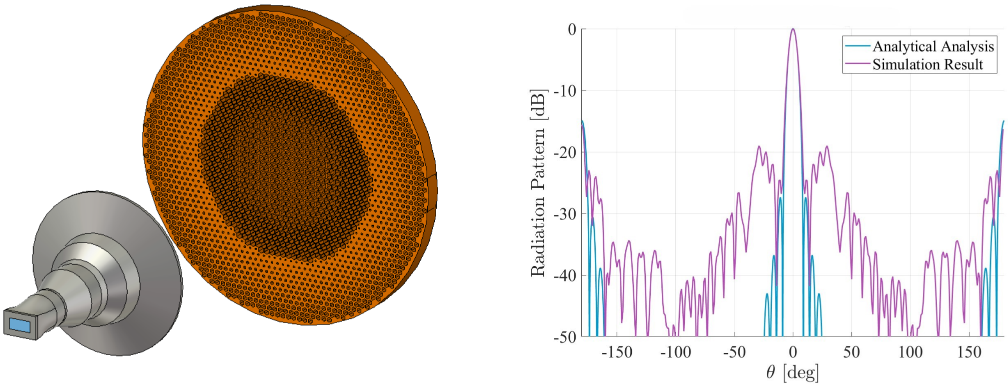

(a) **(b)**

Figure 3.50: UC1: **(a)** CST project layout **(b)** Radiation Pattern at $f_0 = 30$ GHz and ϕ-cut$= 0°$.

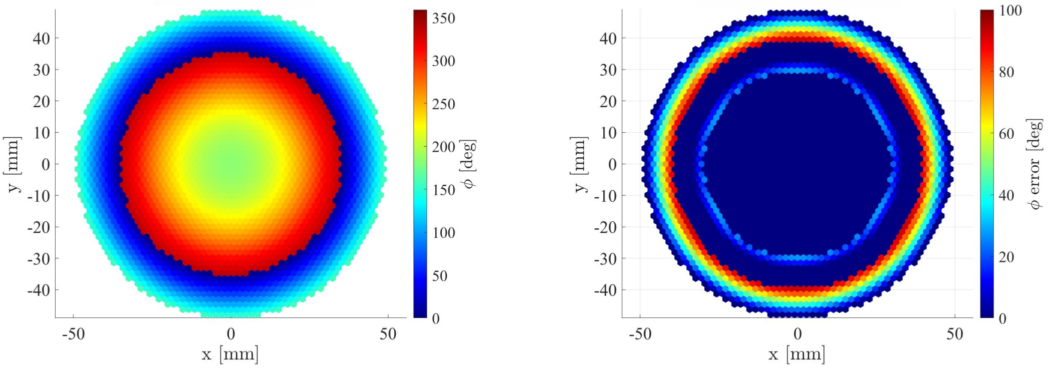

(a) **(b)**

Figure 3.51: UC1: **(a)** Transmission phase distribution, **(b)** Relative phase difference with phase error introduction.

hexagonal pattern. As exhibited in Figure 3.52, the radiation patterns from both design cases showed negligible variations with respect to the spherical coordinate ϕ. Given the symmetrical nature of the configuration, ϕ was defined within the interval 0° to 90°. Lastly, an analysis of the parameter $|S_{11}|^2 + |S_{21}|^2$ for the standard configuration at the design frequency was conducted. The minimum captured in Figure 3.53a indicates a lower bound of 0.75, attributed to elevated dielectric losses at the structure's edges due to an increased material presence. With the integration of phase errors, the minimum value is optimized with an increment of 0.05, as detailed in Figure 3.53b.

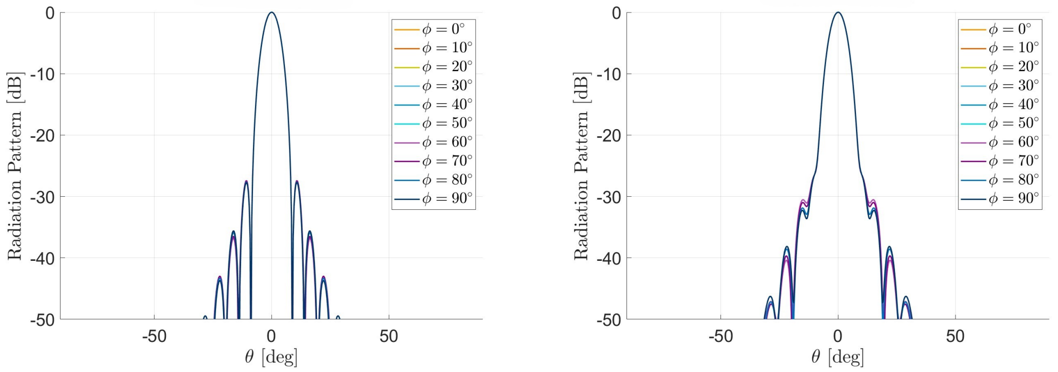

(a) **(b)**

Figure 3.52: UC1: Radiation pattern at $f_0 = 30$ GHz and different ϕ-cuts for **(a)** Standard layout **(b)** Layout with phase error introduction .

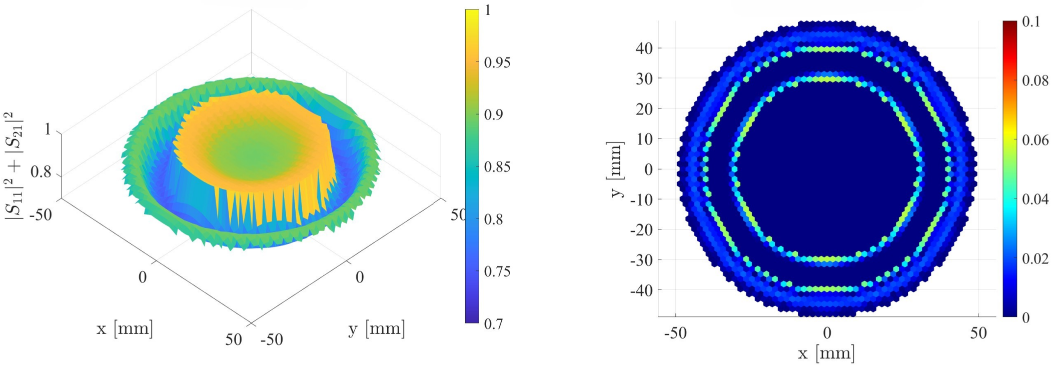

(a) **(b)**

Figure 3.53: UC1: **(a)** Losses 3D distribution, **(b)** Relative losses difference with phase error introduction.

3.6.3 TA design using UC2

The second study analyzes the surface behavior with the usage of the unit cell UC2 as the foundational structural element. A greater number of 2,905 elements was utilized to discretize the surface due to the smaller dimensions of the lattice in this instance. The analysis involved assessing the variation of the free parameter within the range $d \in [0.5, 1.9]$ mm. To optimize the distribution of high values of d across the surface, a baseline transmission phase of $\psi_0 = 150°$ was selected. The CST-based design is illustrated in Figure 3.54a, with its layout derived from the transmission phase values computed for each cell (Figure 3.55a). Compared to the

previous case, in this configuration the optimization allowed obtaining smaller values of d in the central section of the surface, progressively increasing in accordance with the phase curves toward the edges of the structure.
The resulting radiation pattern at $f_0 = 30\,\text{GHz}$ is presented in Figure 3.54b. A notable consistency between the two evaluations is observed, with sidelobe levels remaining below $-15\,\text{dB}$.

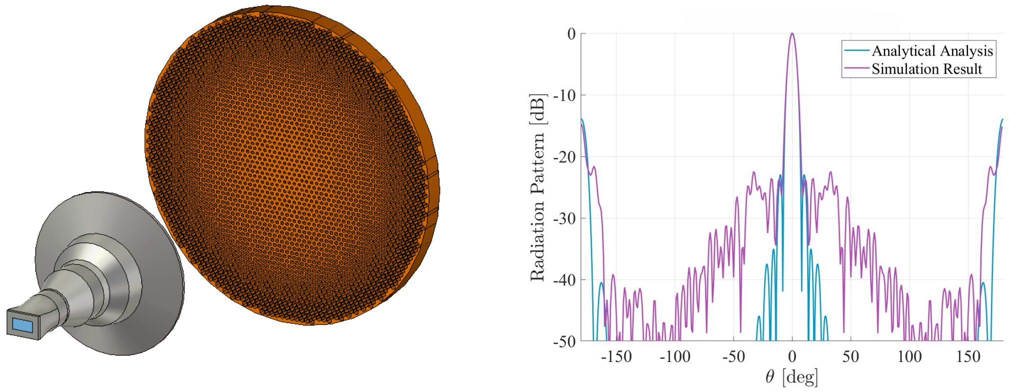

(a) **(b)**

Figure 3.54: UC2: **(a)** CST project layout **(b)** Radiation Pattern at $f_0 = 30$ GHz and ϕ-cut= 0°.

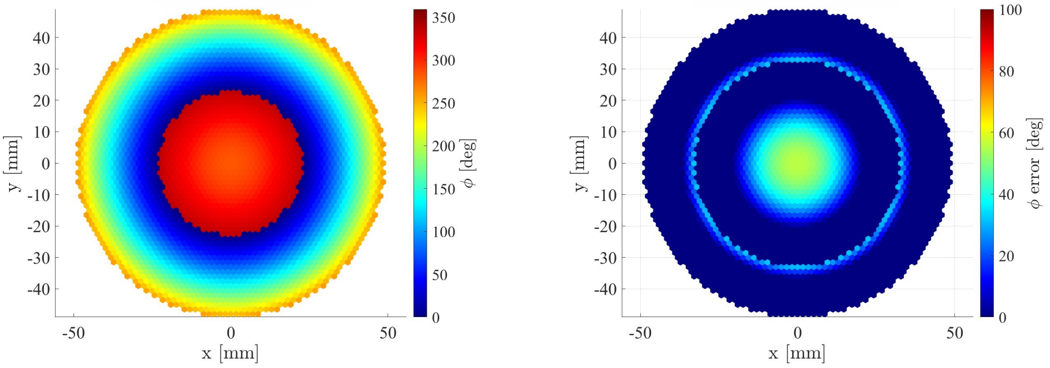

(a) **(b)**

Figure 3.55: UC2: **(a)** Transmission phase distribution, **(b)** Relative phase difference with phase error introduction.

With the introduction of a controlled phase error, the free parameter d is restricted to the sub-ranges $[1.2, 1.45]$ mm and $[1.55, 1.9]$ mm. The selection of these subranges

ensure a $|S_{21}|$ value no lower than -3 dB for all frequencies and incidences. The resulting phase error, shown in Fig. 3.55b, is negligible at the edges of the surface, while it becomes more pronounced in the central region, with an absolute difference of about 60° compared to the standard configuration.
Multiple cut planes confirmed that the radiation patterns remained largely unchanged with respect to the spherical coordinate ϕ, as shown in Figure 3.56.

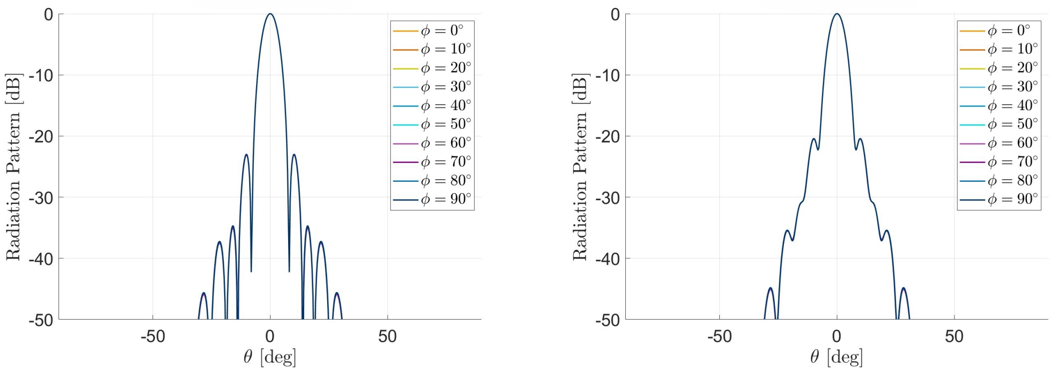

(a) **(b)**

Figure 3.56: UC2: Radiation pattern at $f_0 = 30$ GHz and different ϕ-cuts for **(a)** Standard layout **(b)** Layout with phase error introduction .

Finally, the evaluation of $|S_{11}|^2 + |S_{21}|^2$ showed a minimum of 0.80 for the standard configuration, due to higher dielectric losses at the center. A maximum increment of 0.06 could be reached when phase errors were introduced, as illustrated in Figures 3.57a and 3.57.

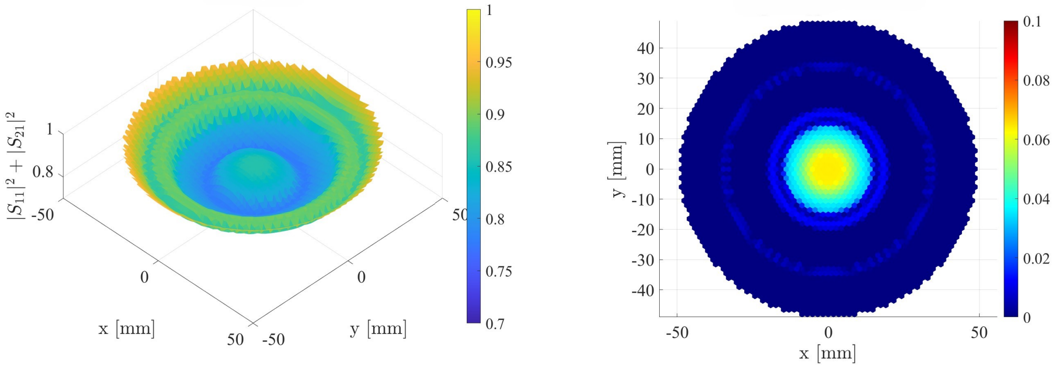

(a) **(b)**

Figure 3.57: UC2: **(a)** Losses 3D distribution, **(b)** Relative losses difference with phase error introduction.

3.6.4 TA design using UC3

In the last study, the surface was discretized using a total of 2,395 elements. It was designed using the final unit cell UC3 with the free parameter d varying within $[0.9, 2.1]$ mm and an arbitrary transmission phase $\psi_0 = 105°$. As in the previous project, this value allowed for an optimized distribution of d across the surface, resulting in smaller values in the central region and gradually increasing toward the edges. The radiation pattern at the design frequency $f_0 = 30$ GHz, shown in Fig. 3.58b, demonstrates again good agreement between the analytical model and CST simulations, with optimized sidelobe levels below -20 dB.

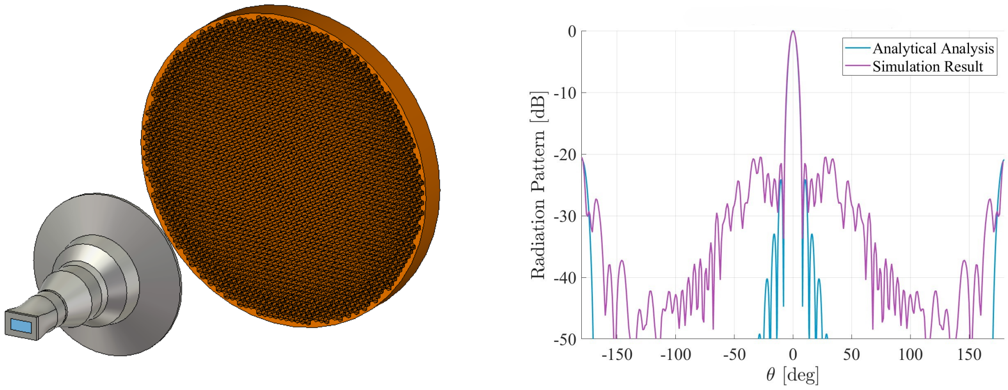

(a) **(b)**

Figure 3.58: UC3: **(a)** CST project layout **(b)** Radiation Pattern at $f_0 = 30$ GHz and ϕ-cut$= 0°$.

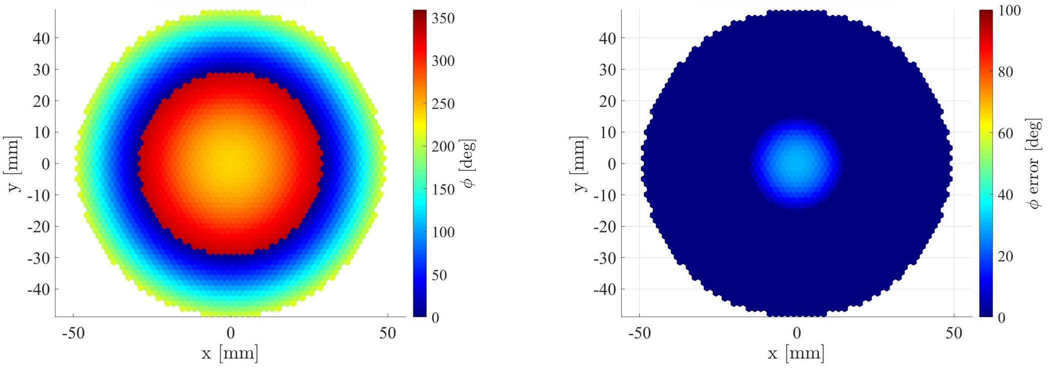

(a) **(b)**

Figure 3.59: UC3: **(a)** Transmission phase distribution, **(b)** Relative phase difference with phase error introduction.

A controlled phase error was introduced by constraining the free parameter d to the sub-range $[1.3, 2.1]$ mm. With these boundaries the $|S_{21}|$ values are no lower than -1.5 dB across all frequencies and incidence angles. As depicted in Fig. 3.59b, the induced phase error is evident only in the central region, reaching an absolute deviation of about 30° compared to the standard configuration.
As illustrated in Figure 3.60, the analysis across multiple cut planes indicates that the radiation patterns are largely similar with respect to the spherical coordinate ϕ. The two curves in 3.60a and 3.60b closely overlap, reflecting that the introduced phase variation is less pronounced in this case.
Finally, the analysis of $|S_{11}|^2 + |S_{21}|^2$ revealed an improved minimum value of 0.85 for the standard configuration and a very low maximum increment of 0.01 when the phase error is introduced, as reported in Figures 3.61.

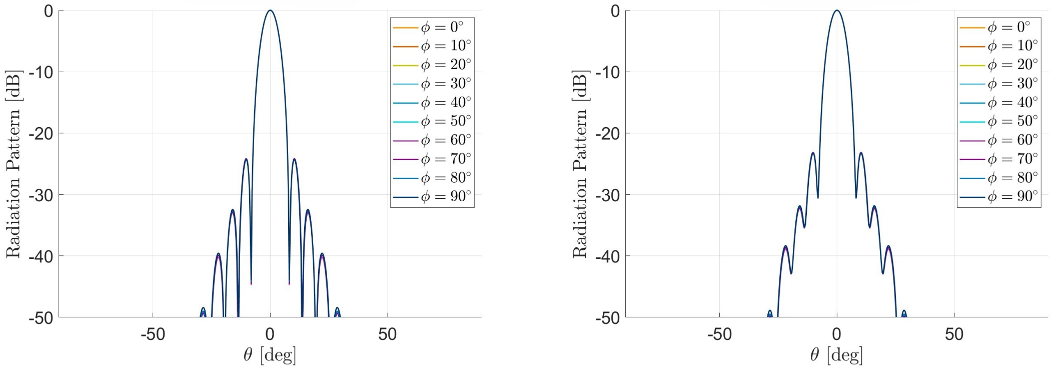

(a) **(b)**

Figure 3.60: UC3: Radiation pattern at $f_0 = 30$ GHz and different ϕ-cuts for **(a)** Standard layout **(b)** Layout with phase error introduction .

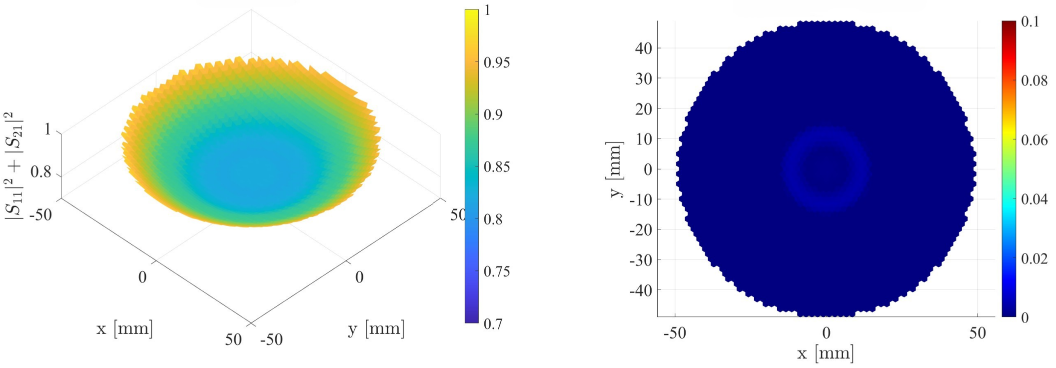

(a) **(b)**

Figure 3.61: UC3: **(a)** Losses 3D distribution, **(b)** Relative losses difference with phase error introduction.

Good radiation pattern results were obtained from the analysis performed on the three TA case studies. In all configurations, the introduction of a phase error marginally impacted the overall performance. This error primarily modifies the boresight radiation profile without altering the Side Lobe Levels or the radial symmetry of the beam. The adoption of this strategy demonstrated an influence on losses as well. The improvement is small since the optimization was only applied to the magnitude of the transmission coefficient. In order to achieve lower losses across the entire range of the free parameter variation, a more effective matching with air would be necessary to reduce the reflection coefficient. Consequently, conclusions can only be drawn regarding the standard configurations utilizing the three distinct unit cell types. The main results obtained from the full-wave simulations in CST MWS are summarized in Table 3.10.

Table 3.10: Results of Simulated TA configurations with $\frac{F}{D} = 1.24$

Unit Cell (UC)	Back Lobe Level (BLL)	Side Lobe Level (SLL)	$\min\{\lvert S_{11}\rvert^2 + \lvert S_{21}\rvert^2\}$
UC1	-16.5 dB	-18.2 dB	0.75
UC2	-15.3 dB	-23.1 dB	0.80
UC3	-21.2 dB	-21.0 dB	0.85

All three TA configurations exhibit excellent BLL and SLL values, which consistently remain below the -15 dB threshold. A deeper analysis of these levels reveals that the UC3 configuration yields, on average, superior results compared to the two simpler unit cell configurations (UC1 and UC2). Furthermore, the UC3 unit cell proves to be the most effective in terms of transmission efficiency. With $min\{|S_{11}|^2 + |S_{21}|^2\} = 0.85$, this cell type ensures lower losses across the array surface compared to the remaining cases. We can therefore conclude that the UC3 unit cell configuration provides the best overall performance trade-off between scattering characteristics and transmission efficiency. Consequently, this specific cell type will be exclusively employed in the subsequent TA analyses and design validation stages.

3.7 Fixed beam TA: Normal Incidence and non broadside pointing

The preceding section examined the focusing properties of the lens with a designed broadside beam. Building on this analysis, the current study introduces a new configuration aimed at steering the beam toward a specified spatial direction. Precise beam steering is essential for applications requiring accurate scanning capabilities, particularly in alignment with designated azimuth and elevation angles.

To explore this mechanism, it is necessary to examine again the phase distribution theory presented earlier. Beam steering is accomplished by adjusting the pointing vector $\hat{r}_0$, as defined in equation 3.1. Unlike the broadside configuration where the scalar product remains null ($\vec{r_i} \cdot \hat{r}_0 = 0$), the steering configuration incorporates an additional phase term essential for the generation of a linear phase front oriented in the desired direction.

This investigation and subsequent evaluations utilize the unit cell UC3, which has been previously identified as the optimal solution for the discretization. The design parameters align with those used in the broadside configuration, maintaining a lens diameter of $D = 10\lambda_0 = 100$ mm at the operational frequency $f_0 = 30$ GHz, along with a focal ratio of $\frac{F}{D} = 1.24$. To evaluate beam-steering capability, a horn antenna was positioned at the reference system's center, while the target beam direction was specified as 20° along the x-axis relative to the broadside (aligned with the z-axis).

Based on the phase distribution theory, a new transmission phase map was obtained for the surface, as illustrated in Figure 3.62a. The analysis employed array theory and was subsequently compared with respect to the CST MWS simulation result. The comparison of the radiation patterns obtained with the two methods is presented in Figure 3.62b and reveals substantial agreement between the two methodologies. The main beam exhibited effective focusing with an accurate steering toward the desired pointing direction. Specifically, predictions from array theory estimated the maximum radiation angle at 18.6°, whereas CST simulations reported a steering angle of 21.0°. In both cases, sidelobe levels were well-contained, maintaining values below -15 dB.

This study validates a simple beam steering technique with the proposed metalens structure. However, it is important to note that these results are restricted to specific structural configuration of the TA, designed to enable beam steering in a singular direction.

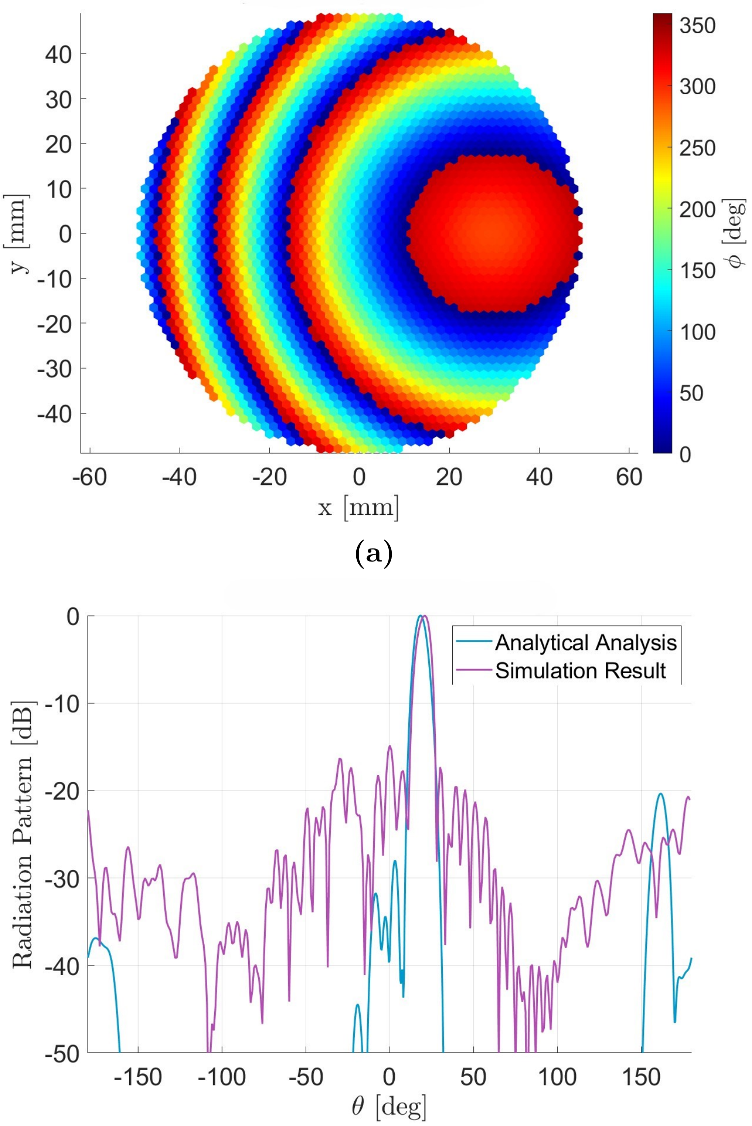

(a)

(b)

Figure 3.62: Centered feed and beam steering of 20° along x-axis: **(a)** Transmission phase distribution, **(b)** Radiation Pattern at $f_0 = 30$ GHz and ϕ-cut $= 0°$.

Chapter 4

Near-Field Analysis

In order to achieve a low-profile antenna design, the lens must be positioned within the near-field region of the feed.

In the context of antenna theory, the radiated electromagnetic field is conventionally categorized into two principal regions: the near field and the far field. The near field refers to the spatial region proximate to the radiating structure, where the field distribution deviates significantly from that of a plane wave and exhibits complex behavior. Within this domain, the amplitude and phase of the electromagnetic field are subject to pronounced spatial variations, making the near-field characteristics strongly influenced by the structural geometry and the relative positioning of the observation point.

Theoretical delineation of the boundary between near and far field regions is typically described as a function of the maximum aperture dimension D of the feed element and the operational wavelength λ_0. The transition is commonly defined by the relationship in 4.1.

$$R \leq \frac{2D^2}{\lambda} \tag{4.1}$$

In this formulation, R denotes the observation distance from the antenna. In our case study, the focal distance F between the feed and the TA is chosen to be smaller than this threshold. For this reason, the system operates under a near-field condition. Conversely, for distances greater than this limit, the system would fall within the far-field domain.

Subsequent sections will detail the theoretical framework describing this near-field analysis, accompanied by a presentation of key results derived from projects.

4.1 Near-Field Phase Compensation

By positioning the TA closer to the source field, near-field effects cannot be disregarded as they were in the earlier far field design. Consequently, it becomes necessary to adjust the model used to determine the transmission phase of the structure's elements. Under near field conditions, the phase of the incident field cannot simply be calculated based on its relationship to the distance R_i between each element and the feed. It is necessary to derive in another way the phase term kR_i introduced in equation (3.1). The recalculated value is directly influenced by the specific field source employed—in this case, the circular horn detailed in the preceding chapter. To obtain this phase term, an analysis of the electric field generated by the source in the near field region must be carried out.

This electric field is sampled over an (x, y) plane at a constant z, which coincides with the incidence plane of the TA, and is expressed through its three complex components. The field can be described as follows:

$$\vec{E}(\vec{r}) = \hat{x}\, E_x(\vec{r}) + \hat{y}\, E_y(\vec{r}) + \hat{z}\, E_z(\vec{r}), \tag{4.2}$$

Where each component can be expressed in complex form as:

$$E_i(\vec{r}) = |E_i(\vec{r})| e^{j\phi_i(\vec{r})}, \quad i \in \{x, y, z\}. \tag{4.3}$$

Since the feed horn generates an electric field with linear polarization primarily along its E_y component, this specific phase can be extracted and utilized for phase compensation.

Accordingly, the revised model that allows to compute the transmission phase is expressed in the equation 4.4.

$$\psi_i = (-\arg\{E_y(\vec{r_i}, F)\} - k\, \vec{r_i} \cdot \hat{r}_0) + \psi_0 \tag{4.4}$$

Here, the negative sign of the correction term represents the phase contribution that must be compensated. This compensated phase term is dependent on the (x, y) coordinates of the structure, combined into the vector $\vec{r_i}$, and on the focal distance F along the z-axis.

Furthermore, changes are required for analyzing radiation through array theory. In this analysis, the excitation term I from equation 3.6 includes an exponential factor describing the incident phase of each element, approximated for far field conditions as $(e^{-ik|\vec{r}_{mn}-\vec{r}_f|})$. To maintain consistency in near field scenarios, this phase contribution should instead be replaced by $\arg\{E_y(\vec{r_i}, F)\}$.

4.1.1 Evaluation of Near Field Effects on Phase Distribution

The initial study of the transmission phase required by the TA was carried out using a reduced diameter of $D = 100\,\text{mm}$. In this section, the goal is to compare results obtained using the earlier far field approximation model (equation 3.1) with those derived from the updated near field model (equation 4.4). To this end, three focal distances were analyzed: 200 mm, 123.75 mm, and 50 mm, as illustrated in Figure 4.1.

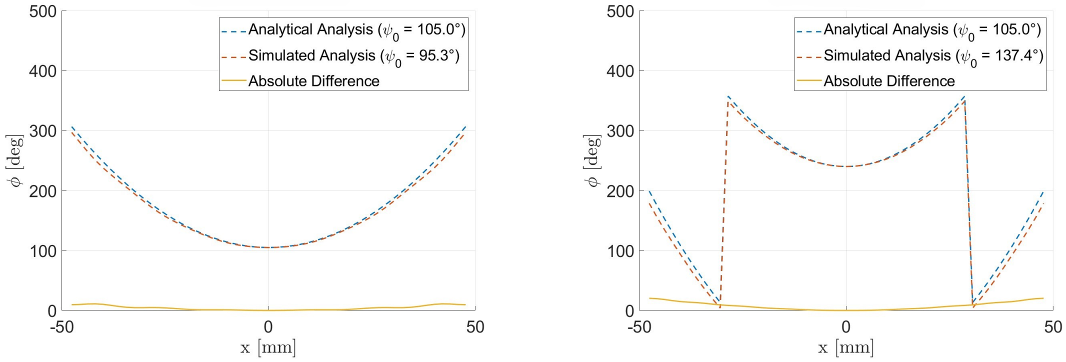

(a) $F = 200$ mm **(b)** $F = 123.75$ mm

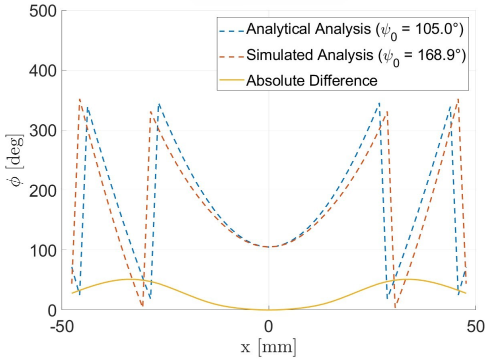

(c) $F = 50$ mm

Figure 4.1: Transmission phase difference at different focal lengths.

The absolute differences between the far field method, labeled as Analytical Analysis in the legend, and the near field method, labeled Simulated Analysis, become increasingly significant as F decreases. To compute this difference in a meaningful way, the two phase distributions were aligned with respect to the central point of the surface through a precise tuning of the term ψ_0 in the near field case, while keeping the far-field case fixed at the value of 150°, as established in the previous chapter. For a focal distance of $F = 200\,\text{mm}$, the maximum deviation is 20°. At $F = 123.75\,\text{mm}$ the difference increases to 30°, while the maximum deviation of 50° is obtained with $F = 50\,\text{mm}$.

This comparison confirms the validity of the near field model introduced earlier. It demonstrates its ability to support smaller focal distances while minimizing approximation errors, providing a more accurate approach for scenarios involving strong near field effects.

4.2 Normal Incidence and Boresight pointing ($\frac{F}{D} = 0.25$)

In light of the previously described theory, a new TA design has been developed using the unit cell UC3. The source is a circular horn, centrally positioned with respect to the surface and set at a reduced focal distance of $F = 50$ mm. The surface diameter has been doubled, resulting in $D = 20\lambda_0 = 200\,\text{mm}$, which leads to a lower focal-to-diameter ratio of $\frac{F}{D} = 0.25$ compared to precedent studies.

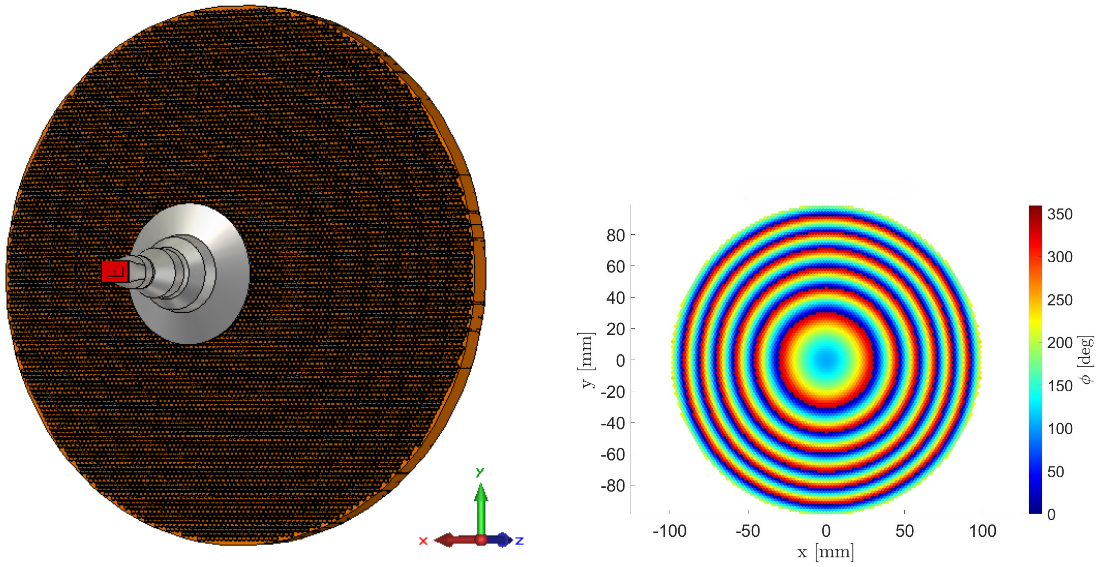

(a) **(b)**

Figure 4.2: Project at $f_0 = 30$ GHz with $D = 200$ mm and $F = 50$ mm: **(a)** CST project layout, **(b)** Transmission phase distribution.

A total number of 9745 elements were employed for the discretization of the entire surface. Given the computational complexity associated with the design and analysis of this lattice, GPU acceleration techniques were applied to reduce simulation time by half. The design itself, illustrated in Figure 4.2a, aimed to achieve beam focusing in the simplest broadside direction.

The electric field generated by the single horn was sampled on the (x, y) plane at a distance $z = 50$ mm, where only the complex component E_y was extracted to determine the desired incident phase. Subsequently, the transmission phase of each element was calculated via equation 4.4, assuming the phase contribution from the scalar product to be zero due to the straightforward orientation of the beam. The obtained phase distribution is depicted in Figure 4.2b, clearly demonstrating pronounced phase periodicity resulting from the expanded TA dimensions and reduced focal distance F.

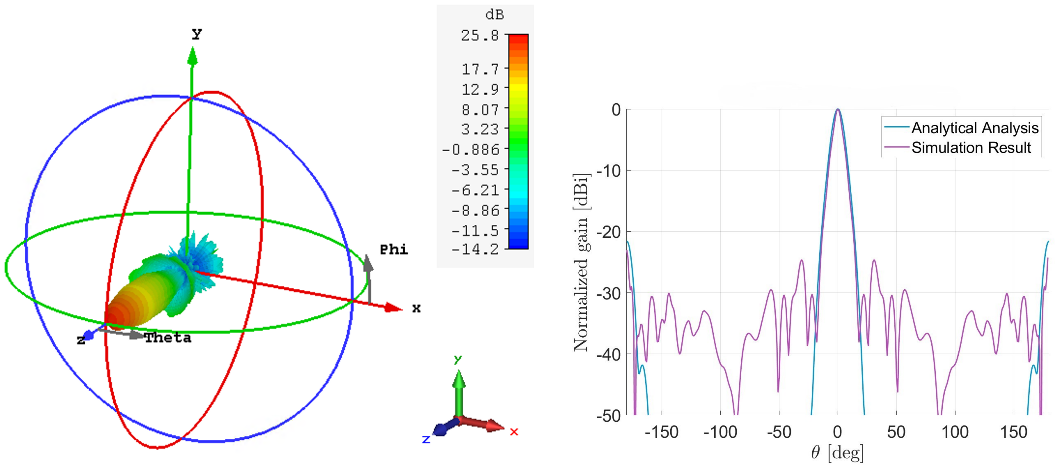

(a) **(b)**

Figure 4.3: Project at $f_0 = 30$ GHz with $D = 200$ mm and $F = 50$ mm: **(a)** 3D visualization of the gain of the system, **(b)** Radiation Pattern at $f_0 = 30$ GHz and ϕ-cut$= 0°$.

Figure 4.3 presents simulation results at the design frequency $f_0 = 30$ GHz. As visible in Figure 4.3b, the array-theory-based model closely approximates the main lobe of the radiation pattern. On the horizontal plane, the main beam exhibits a notable widening compared to earlier designs, attributed to the feed's closer placement. The SLLs were optimized to remain below -25 dB in the normalized pattern, while the BLL is lower than -20 dB. At this frequency, the gain achieved is 25.8 dB.

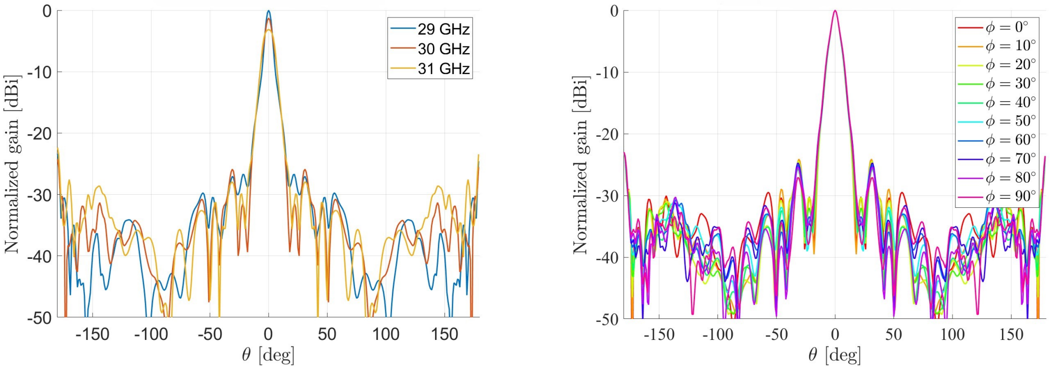

(a) **(b)**

Figure 4.4: Project at $f_0 = 30$ GHz with $D = 200$ mm and $F = 50$ mm: **(a)** Radiation Pattern in the frequency band of interest, **(b)** Radiation Pattern at $f_0 = 30$ at different ϕ-cuts.

A further analysis of the radiation pattern on the horizontal plane across the frequency band of interest is illustrated in Figure 4.4a. Superior radiation performance was observed at 29 GHz, while a loss of approximately -3 dB is obtained at 31 GHz. Notably, SLLs and BLLs remained consistent in the frequency band. Figure 4.4b provides a comparison of the radiation pattern at the design frequency, showcasing symmetrical beam properties across different ϕ-planes. Expanding the frequency analysis to the range of 27 GHz to 31 GHz facilitated an evaluation of the gain behavior across the band (Fig. 4.5a). As it can be observed the parameter follows a bell-shaped curve, with a peak of 27.2 dB at 28.8 GHz. Higher frequencies exhibited approximately a 3 dB reduction by 31 GHz.

Radiation efficiency (Fig. 4.5b) peaked at 86.4% at 28.2 GHz, with a maximum reduction of around 3% across the band.

Lastly, the reflection coefficient of the system (Fig. 4.5c) demonstrated values below -15 dB throughout the band, with particularly strong optimization around the design frequency of 30 GHz.

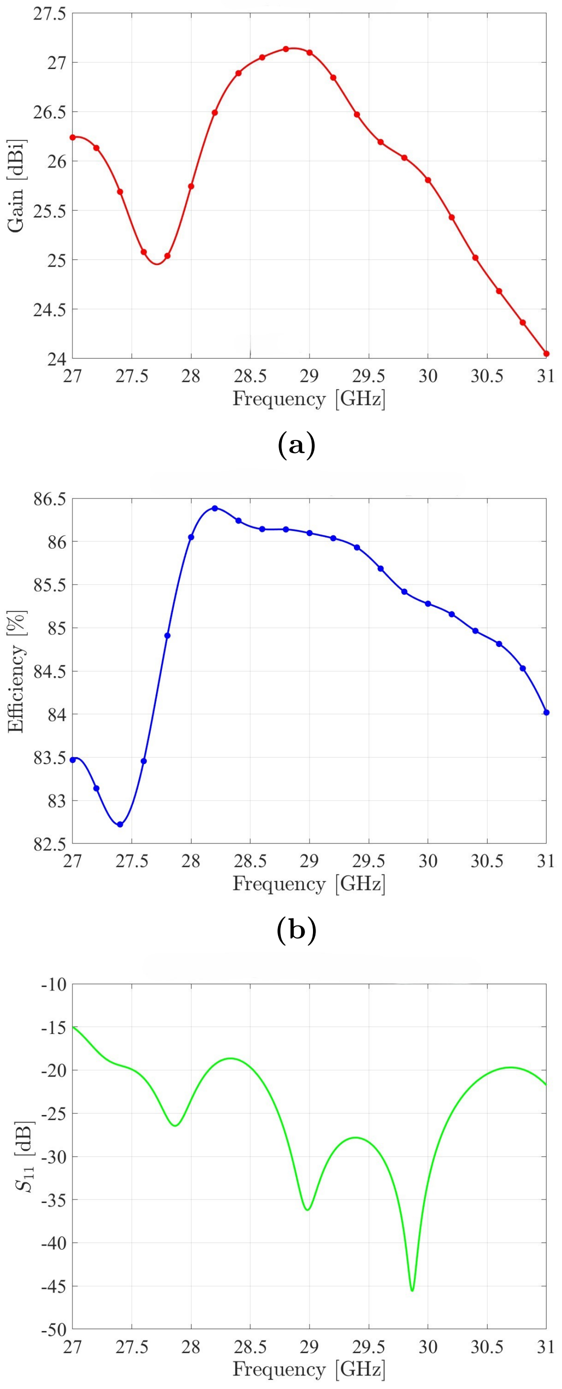

(a)

(b)

(c)

Figure 4.5: Project at $f_0 = 30$ GHz with $D = 200$ mm and $F = 50$ mm: **(a)** Gain versus frequency, **(b)** Radiation efficiency versus frequency, **(c)** Reflection coefficient S_{11} versus frequency.

4.2.1 ε_r variation

This analysis delves into the variation of the material's electric permittivity, a key structural parameter initially set to $\varepsilon_r = 9.6$, based on the characteristics of PREPERMABS1000. The study explores the impact of adjusting this parameter within the range $\varepsilon_r \in [9.5,10]$ on the previously evaluated performance metrics.
Figure 4.6a presents the radiation pattern at the design frequency on the horizontal plane of the system under investigation. The main beam remains unaltered in direction and shape, with only minimal deviations observed in the overall radiation pattern. This robust behavior is a key finding, as these slight variations do not significantly influence the previously established SLL and BLL levels.

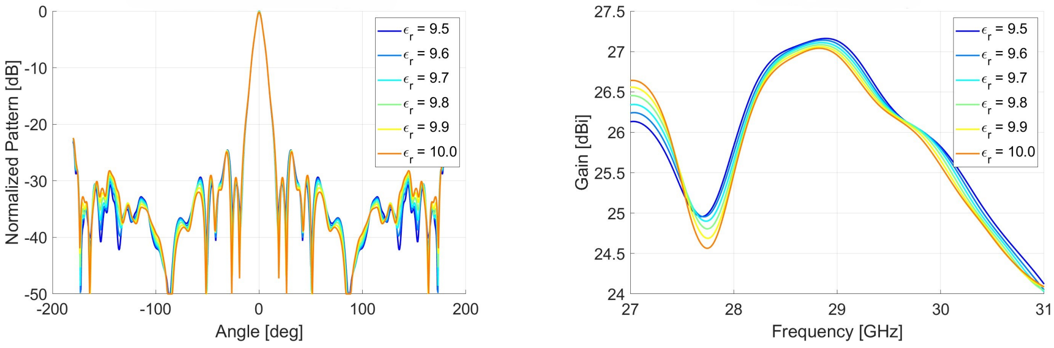

(a) **(b)**

Figure 4.6: Effect of ε_r variation in the interval [9.5,10]: **(a)** Radiation Pattern at $f_0 = 30$ GHz and ϕ-cut= 0°, **(b)** Gain versus frequency.

Figure 4.6b reveals that the gain exhibits a maximum penalty of 0.5 dB at low frequencies. Crucially, the deviations between 29 GHz and 30 GHz remain minor, measuring less than 0.2 dB when compared to the previously analyzed characteristic curve. Figure 4.7b shows a minimal reduction around 30 GHz of the reflection coefficient working point with an higher permittivity. The variation of the material affects radiation efficiency, with an observed in-band degradation of approximately 1%, as highlighted in Figure 4.7a.
The findings highlight a meaningful indication of fabrication tolerance, allowing for an error margin greater than what manufacturers typically guarantee. Considering typical electric permittivity deviations of 0.1 to 0.2, this analysis demonstrates that such uncertainties can be effectively accommodated without significant performance risks.

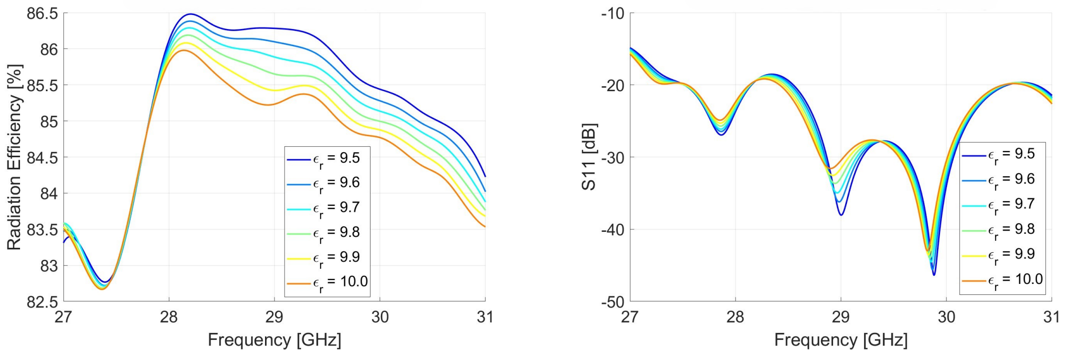

(a) **(b)**

Figure 4.7: ε_r variation in the interval [9.5,10]: **(a)** Radiation efficiency versus frequency, **(b)** Reflection coefficient S_{11} versus frequency.

4.3 Oblique incidence and pointing ($\frac{F}{D} = 0.25$)

Previously, the feed was positioned at the focal distance F and the surface was configured specifically for perpendicular beam propagation.

This final analysis focuses on a critical aspect of TA design: the strong correlation between the incident phase on the surface and the focal point. This spatial dependency was further validated by rotating the feed around its phase center. By definition, an antenna's phase center is the spatial point with respect to which the phase of the radiated field remains invariant across different observation directions. The electromagnetic field emitted by the antenna produces spherical wavefronts that are concentric with respect to this particular point, which identifies the effective source location. In view of this consideration, the circular horn antenna was placed at the same focal point F, aligned with its phase center, and rigidly rotated by 20° around the y-axis.

In this particular arrangement, the TA was specifically configured for an oblique incidence angle $\theta_{\text{inc}} = 20°$, achieving a maximum radiation angle $\theta_{\text{max}} = 10°$. The system is designed to operate at the central frequency of 30 GHz and utilizes a circular aperture with a diameter $D = 200$ mm $= 20\lambda_0$. The TA employs the optimal UC3 unit cell structure and a focal-to-diameter ratio $F/D = 0.25$ is selected, with the illumination provided by a circular horn feed.

In Figure 4.8 it is possible to observe the configuration of the system and the design conventions adopted throughout the analysis.

Within this configuration, the transmission phase map necessary to accomplish the intended beam steering demonstrates a unique profile, as captured in Figure 4.9a. The radiation pattern of this configuration is analyzed with respect to the TA reference frame.

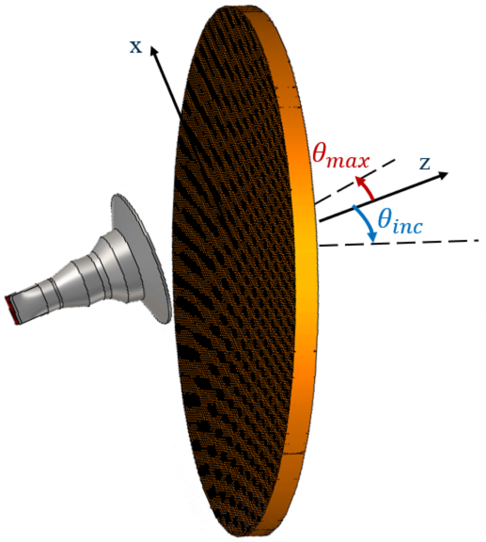

Figure 4.8: Oblique incidence and pointing configuration.

The resulting performance indicates an anticipated beam steering effect of approximately 30° along the horizontal plane, aligning with the theoretical prediction ($\theta_{\text{inc}} + \theta_{\text{max}}$ with the defined convention). As shown in Figure 4.9b, the radiation pattern is stable in the frequency band of interest. The main beam is located at $\theta = 32.00°$ and the SLL is lower than -18 dB.

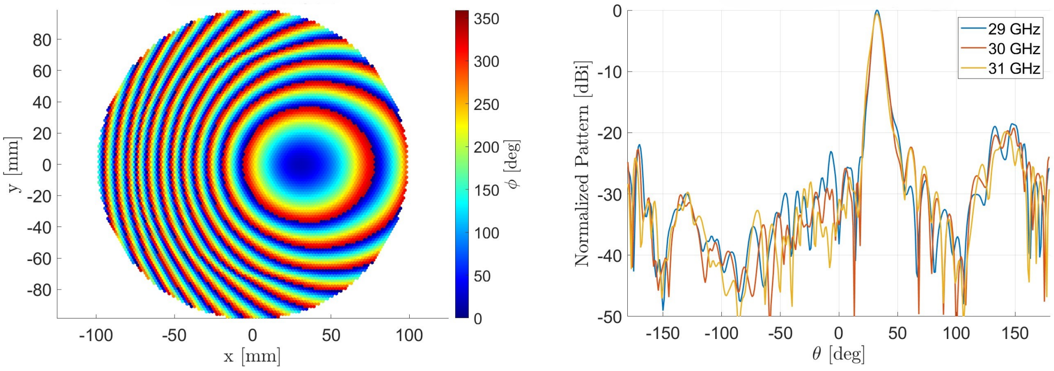

(a) **(b)**

Figure 4.9: Oblique incidence and pointing: **(a)** Transmission phase distribution, **(b)** Radiation Pattern in the frequency band of interest.

Figure 4.10 illustrates the antenna gain performance in the frequency range of $[29, 31]$ GHz. The gain exhibits a peak value of 24.76 dB at 29.4 GHz and it is characterized by a variation of less than 0.65 dB throughout the entire considered frequency range.

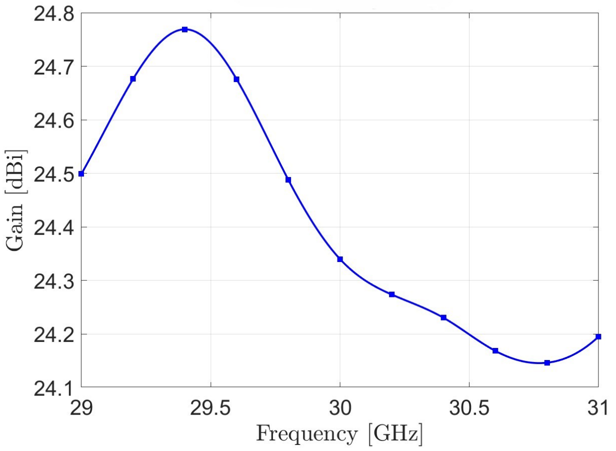

Figure 4.10: Oblique incidence and pointing: Gain versus frequency.

Chapter 5

Beam Steering Mechanism

This chapter illustrates and analyzes two distinct design solutions formulated to implement beam steering functionality. Both of them are based on the design of a bifocal lens structure, which is a particularly effective methodology for the optimization of the overall system performance.
These two concepts currently represent preliminary proposals, based on the integration of a mechanical structure in order to obtain the desired beam-steering. This design orientation aligns with the trends emerging from the state-of-the-art in transmitarrays. Specifically, the introduction of a dynamic degree of freedom, realized through physical movement, is demonstrated to be an essential factor in order to achieve optimal results in terms of both in-band gain and maximum scan capability.

5.1 State Of the Art

A central functionality of transmitarrays is the beam steering, which enables dynamic control of the radiation direction.
To better illustrate the current design strategies and performance trade-offs, different representative transmitarray prototypes from recent literature are reviewed in this section.
In figure 5.1 is presented a dual-band TA from Pham *et al.* [33]. The structure consists of two subarrays: one operates at 19.5 GHz in down-link while the other operates in up-link at 29 GHz. The unit cells have a square shape, arranged in a rectangular lattice and decoupled in the down- and up-links. Two different feed sources are employed, shifting along several focal points in one direction. The TA beam can be scanned up to ±40° independently in each band with a scan loss lower than -2 dB. The phase layout is optimized with a bifocal phase distribution

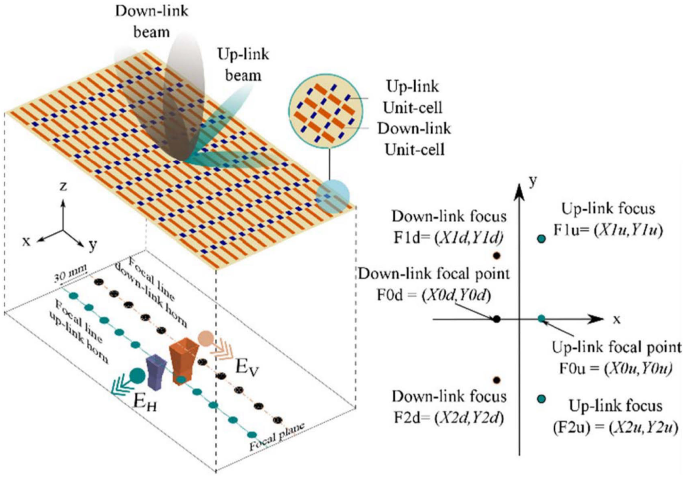

Figure 5.1: Dual-band TA architecture with independent beam scanning and different focal points (Image reproduced from Pham *et al.* [33]).

reported in Eq. (5.1).

$$\phi_{lens}^{bifocal} = \frac{A_1\phi_1^{unifocal} + A_2\phi_2^{unifocal}}{A_1 + A_2} \tag{5.1}$$

This type of solution has been studied by Matos *et al.* [38] with a steering mechanism based on in-plane lens translation in front of a stationary feed. The solution achieves 41 dBi directivity, with a scan loss better than -3 dB and side lobes level below -15 dB for a scan angle ranging from 16° and 56°.

The study sustain that "mechanical steering antennas tend to be a more affordable option with respect to the electronic steering counterparts, at the cost of having bulkier solutions"[38] . The same design is presented by Lima *et al.* [39], with a lens dimensions of 195 mm x 145 mm, weight of 215g and a total antenna height of 84 mm. The unit cell type is based on few dielectric layers with sub-wavelength capacitive square printed patches able to cover the desired 360° phase range. In figure 5.2 the described structure is shown, where the number of layers contributes to the phase shift. The unit cell is symmetrical and it is composed of two pairs of $L1$ and $L2$ patches with a single central $L3$ patch.

This configuration allows to obtain polarization independence, necessary for the rigid rotation of the lens with respect to the source for a full azimuth coverage. In the research is also presented a new strategy for the effective $\frac{F}{D}$ reduction of the focusing system. "A virtual focus is created below the feed phase center with the use of a small flat lens positioned on top of the primary feed"[39].

A mechanical beam scanning technology is also selected in the structure reported in figure 5.3 and proposed by Madi *et al.* [40], which integrates a shared aperture

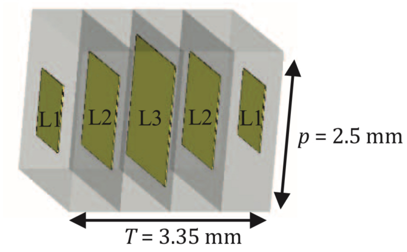

Figure 5.2: Unit cell based on layers of dielectric material and square patches (Image reproduced from Lima *et al.* [39]).

for the operation in both Ku and Ka bands.

The lens is based on a unit cell realized using five metal layers and it is illuminated by two horns mounted in orthogonal polarization at a distance of 110 mm. The system can reach high values of gain in the two bands of interest, respectively 27.1 dBi in down- and 29.9 dBi in up-link. The steering is obtained again with a manual movement of the focal source along the y-axis of the flat lens.

Moreover, Matos *et al.* [40] presented an iterative method for the optimization of the discussed unit cell distribution in the aperture for a lower value of $\frac{F}{D}$.

Liu *et al.* [35] demonstrated a transparent multibeam transmitarray operating at Ka-band. The structure of the TA is reported in figure 5.4, it is combined with seven array feed sources that can be activated alternatively with GaAs switches to achieve beam steering the H-plane from $-30°$ to $30°$. The TA unit cell is composed of meshed double-circle rings printed on a plastic material transparent to the visible light. It is characterized by a transmission loss no lower than -1 dB and a minimum dependence with respect to the angle of incidence at the Ka-band. The TA has a diameter of $9.9\lambda_0$ at 28.5 GHz, with a broadside gain of 25 dBi and the off-axis 30° peak gain of 21.5 dBi. This type of solution can be used in small cells and smart street furniture. It is not particularly suitable for satellite applications due to the low sensitivity of the scanning range, which is achieved through discrete feed switching.

"A possible realization of a beam-scanning system consists in the integration of active elements such as varactors or p-i-n diodes within the unit-cell design", as demonstrated by Padilla *et al.* [41] and Di Palma *et al.* [42].

These tunable components guarantee a "dynamic control of the transmission phase across the aperture", resulting in "optimal beam-steering capabilities and good radiation performance"[41]. However, this flexibility comes at the cost of a more complex structure, due to the presence of biasing networks and additional circuit layers. Also the efficiency is affected due to the non-ideal behavior of the active components.

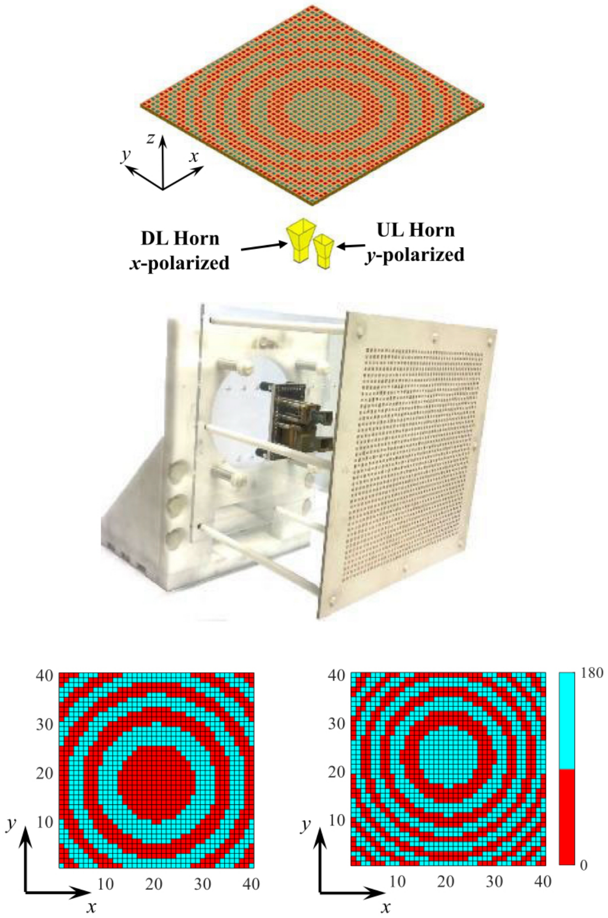

Figure 5.3: Schematic view (top) and photograph (middle) of the shared aperture TA with 1-bit phase gradients (down-link left-bottom and up-link-right-bottom) (Image reproduced from Madi *et al.* [40]).

Overall, active transmitarrays represent a promising step toward fully reconfigurable and adaptive aperture antennas, but their practical implementation still involves a delicate trade-off between performance, complexity, and fabrication feasibility.
The presented solutions occupy a relevant volume and the steering mechanisms are characterized by mechanical motion. The focal distance is also an important parameter of the designs that have been analyzed, which has to be minimized. The relative position between the feed and the lens is fixed, for this reason a mechanical motion of one of the two parts is still necessary.
"Ongoing research aims to enhance the performance through the integration of tunable materials, such as liquid crystals, graphene, and phase-change media, as well as through the application of optimization algorithms and machine-learning-based

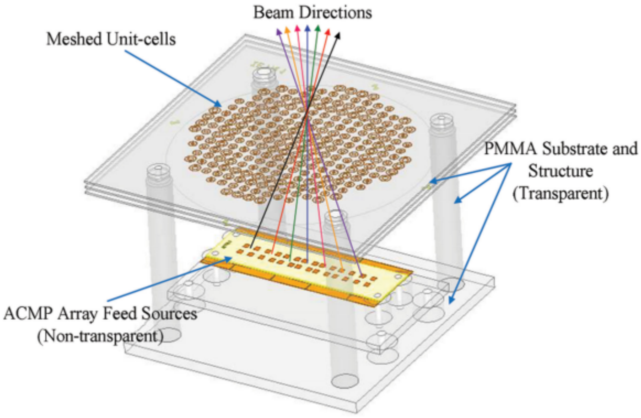

Figure 5.4: Tree-dimensional view of a system composed of sparse feed array and TA (Image reproduced from Liu *et al.* [35]).

synthesis methods" [43, 44].

5.2 Bifocal Lens - Feed Rotation

From the analysis of the results from the dual-band TA of Pham *et al.* [33] and the researches of Matos *et al.* [38] and Lima *et al.* [39], we aim to design a bifocal lens in order to achieve an optimal beam-steering. The first proposal is based on the design of a surface with the selected cell UC3 and a diameter $D = 200$ mm, illuminated by a feed positioned at a focal distance $F = 200$ mm. The resulting $F/D = 1$ describes a medium-sized profile. Despite not being ideal for a compact solution, this ratio is necessary for an accurate assessment of the scanning performance.
To enhance the scanning capabilities of the TA, a bifocal strategy can be adopted. With this approach, the required phase distribution of the lens is derived from the average of two distinct phase distributions, which are calculated by considering a different source focal position and desired pointing direction. Specifically, the design is based on the rotation of the source around the y-axis, maintaining the pointing direction towards the center of the lens. The feed has an angular freedom of movement θ_f of $\pm 40°$.
Figure 5.5 shows the schematic drawing of the two cases taken into consideration. In order to maintain a symmetric structure, the two offset angles have been chosen to be $\theta_{f1} = 40°$ and $\theta_{f2} = -40°$. Once the two focal points of the design are fixed, the phase path from these points to the surface can be identified, obtaining two distinct incident phase distributions on the aperture.
With this approach it is possible to determine two TA configurations that provide the

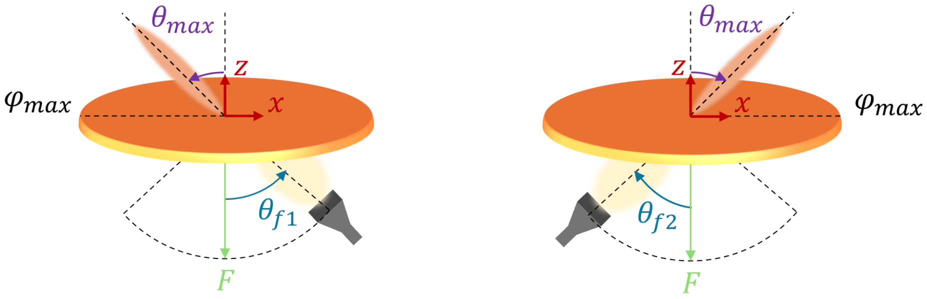

(a) **(b)**

Figure 5.5: Schematic representations of the feed positions and desired pointing directions.

desired pointing. For the feed with an incidence of $\theta_{f1} = 40°$, a phase compensation ϕ_1 is proposed, which allows for a pointing direction characterized by $\theta_{\max} = 40°$ and $\varphi_{\max} = 180°$ (Figure 5.5a). Conversely, for $\theta_{f2} = -40°$, a surface with a phase distribution ϕ_2 is adopted to achieve a pointing direction at $\theta_{\max} = 40°$ and $\varphi_{\max} = 0°$ (Figure 5.5b). These are the conventions utilized to define the beam directionality. It is important to emphasize that the problem has been reduced to a single-dimension scanning, specifically along the x-axis of the system. The required phase distributions for the two configurations are presented in Figure 5.6.

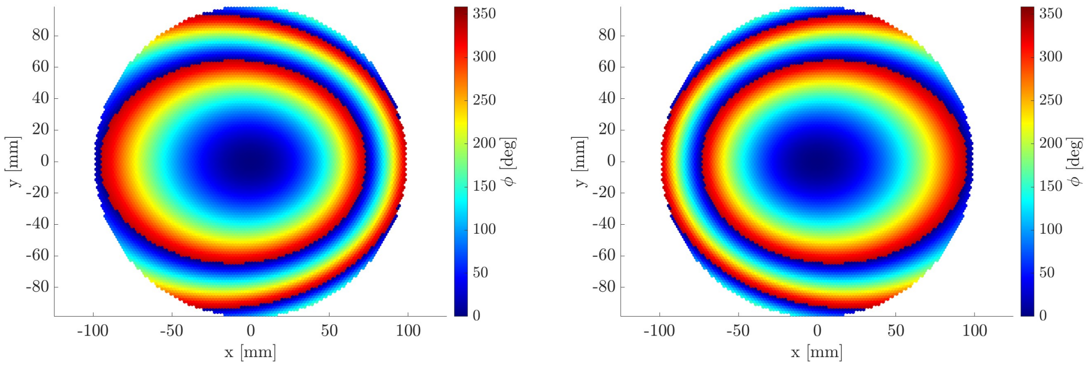

(a) ϕ_1 **(b)** ϕ_2

Figure 5.6: Phase distribution for the two feed placements.

Finally, the required phase distribution for each (m, n)-th element of the bifocal configuration can be uniquely derived through an averaging operation, as illustrated in Equation 5.2.

$$\phi_{bif}(m,n) = \frac{\phi_1(m,n) + \phi_2(m,n)}{2} \tag{5.2}$$

The result of this operation is presented in Figure 5.7, along with the frontal profile of the structure simulated in CST. This surface is characterized by a new phase distribution featuring an elliptical shape.

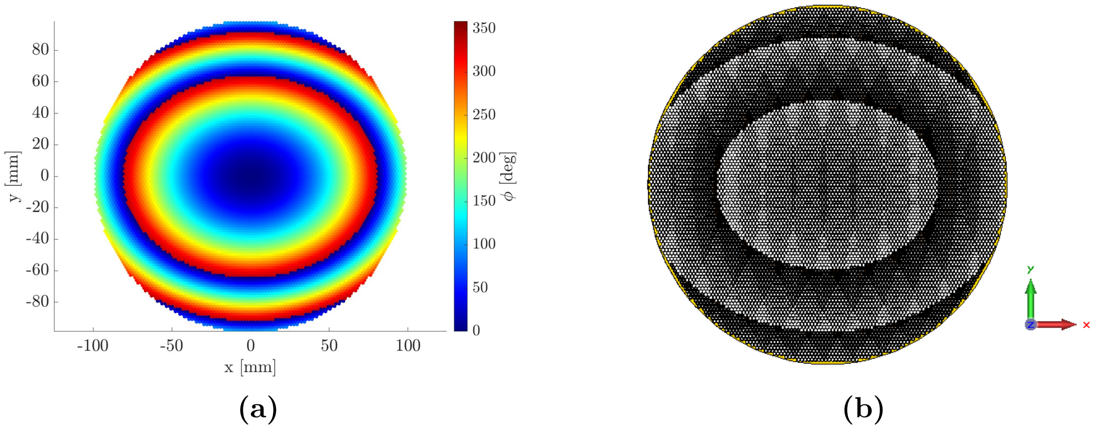

(a) **(b)**

Figure 5.7: Bifocal lens: **(a)** Phase distribution, **(b)** Front view of the CST model.

The bifocal transmitarray was numerically simulated using CST MWS, along with the unifocal version designed with a central feed placement. This facilitates a direct comparison of the performances of the two structures. The antenna radiation patterns have been evaluated for different positions of the source in the angular range $[-40, 40]^\circ$, obtained by moving the horn along a circular arc centered on the TA center. The radiation patterns obtained along the horizontal plane at 30 GHz for different values of θ_f are shown in Figure 5.8.

The scanning range is ±36° for the unifocal case and ±32° for the bifocal configuration. It is important to observe how the radiation pattern of the unifocal lens degrades as the pointing angle increases. The antenna's performance deteriorates rapidly due to the strong dependence of the unit-cell with respect to the direction of the incident field. As analyzed during the selection of the elementary cell type of the surface, the angle of incidence introduces both a phase and a magnitude error on the transmission coefficient. The impact on the latter, in particular, degrades the beam characteristics when a larger inclination is required. This effect can only be mitigated with a robust unit-cell design. Ideally, the unit cell should exhibit a transmission magnitude $|S_{21}|$ with a low dependence on the angle of incidence.

Table 5.1 presents the comparison of the gain and Side Lobe Levels (SLL) of the two configurations at 30 GHz.

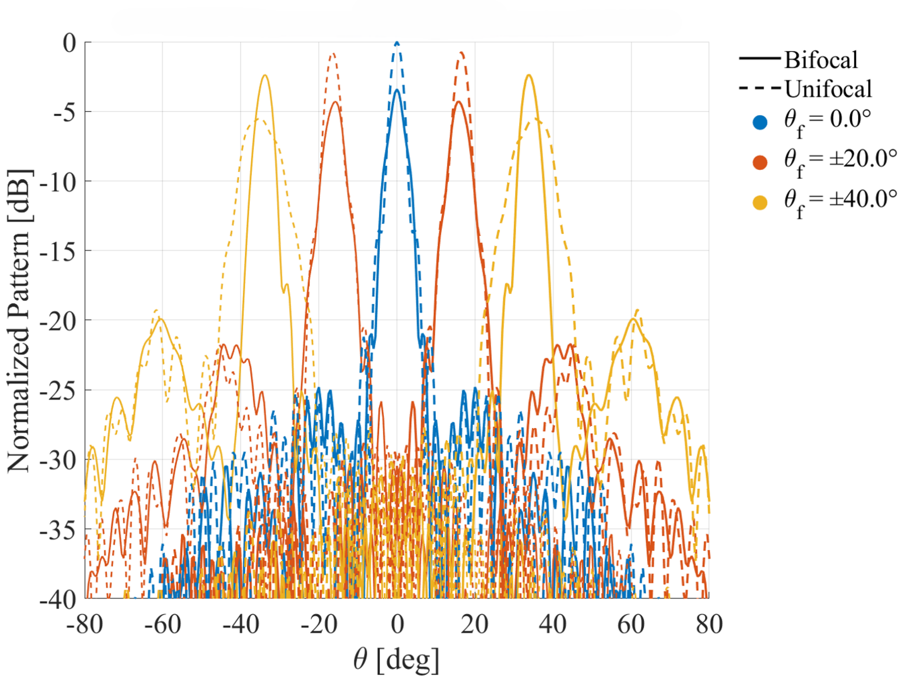

Figure 5.8: Feed rotation: Bifocal lens radiation patterns versus the unifocal case in the horizontal plane at 30 GHz.

Table 5.1: Feed rotation, unifocal versus bifocal designs at 30 GHz

θ_f	0°	±20°	±40°
Gain (unifocal)	32.84 dB	30.14 dB	27.34 dB
Gain (bifocal)	29.42 dB	28.20 dB	29.63 dB
SLL (unifocal)	-21.2 dB	-19.9 dB	-3.4 dB
SLL (bifocal)	-17.6 dB	-17.4 dB	-15.1 dB

The bifocal design exhibits a better trade-off between the two performance metrics. This solution tends to favor pointing at larger angles, where the maximum gain value of 29.63 dB is achieved at the design frequency, while maintaining good stability with smaller inclinations. The Side Lobe Levels (SLL) are improved in the bifocal TA case for an incidence of ±40°, while being reduced at incidences of 0° and ±20°. These values, however, remain below -15 dB throughout the entire radiation range.

To conclude, Figure 5.9 shows the gain behavior as a function of the pointing angle for both the unifocal and bifocal configurations. These graphs allows to analyze

the scan loss of the two antennas and their behavior across the band of interest, which is between 29 GHz and 31 GHz.
For the unifocal configuration, it can be observed that with higher frequencies the gain increases uniformly across the entire scan range, with a maximum in-band scan loss of 5.5 dB.
On the other hand, the bifocal lens introduces a reduction of the maximum achievable gain, balanced with the improvement of the scanning characteristics with a maximum in-band scan loss of 2 dB.

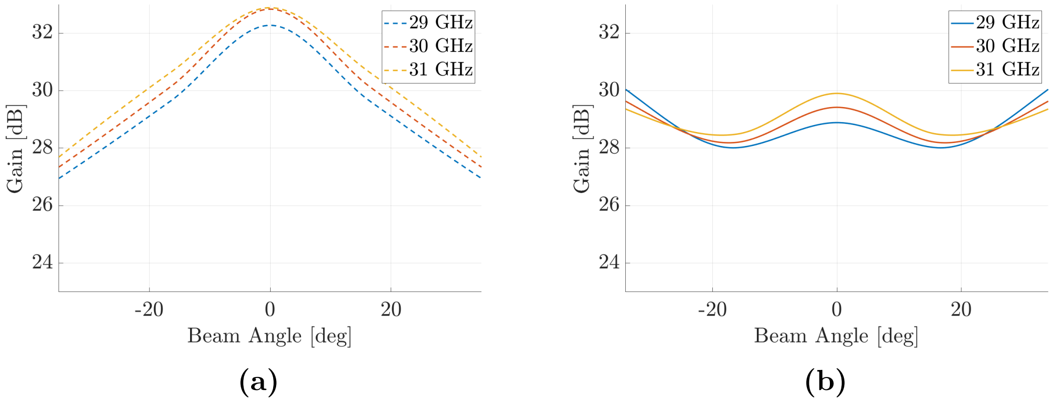

(a) **(b)**

Figure 5.9: Gain vs Beam Angle with feed rotation: **(a)** Unifocal lens, **(b)** Bifocal lens.

This first analyzed design is able to cover a limited angular range with a medium-sized structure. Such a solution cannot be easily implemented in practical applications because the rotation of the feed constitutes a significant constraint.
For this study, a horn antenna was utilized as the source for simplicity, but the final application would necessitate the integration of radiating elements on a PCB, such as simple patch arrays. The rotation of these components cannot be easily implemented considering the feeding constraints and the physical occupation that would result from reaching the required angles of incidence on the surface.
A possibility is the discretization of the incidence cases with the combination of multiple radiating elements. However, this approach would result in a more complex structure, still constrained to single-axis scanning.
The study showed interesting results in terms of gain stability and SLL limitation. The mechanical feed rotation and the large 200 mm focal distance represent the main obstacles for SOTM applications.

5.3 Bifocal Lens - Feed Translation

This final section proposes an evolution of the previous concept for both elevation and azimuth beam steering. The critical issues identified in the preceding solution were the inability to achieve a low-profile configuration and the unfeasible realization of the source rotation. For this reason, the new bifocal lens is positioned at a focal distance $F = 80$ mm, which, given the same surface diameter, results in an F/D ratio of 0.4. This value is significantly smaller than the typical ratios found in the state-of-the-art for scanning lenses, allowing for a significant reduction in the antenna's height.

The feed movement is based on a rigid translation along the x-axis. The issue related to the source movement is still present, but it can be solved by applying the horizontal translation to the flat lens while maintaining the feed in a fixed position. In this configuration, an in-plane rotation of the lens provides full 360° azimuth beam steering.

The design is based on an asymmetric scanning range, extending from 0° to 60°, which is able to provide a ±60° conical coverage when considering the full 360° azimuth rotation. The strategy adopted to achieve high scan angles, despite the reduced F/D ratio, relies on designing a lens that enables a non-zero elevation angle ($\alpha_0 \neq 0°$) for a central feed position ($a = 0$ mm).

To accomplish this, it is necessary to obtain a model that allows us to analyze the dependence of the scan angle α on the source translation a. For this one-dimensional analysis, the incident electric field illuminating the lens can be seen as a spherical phase distribution. Equation 5.3 describes this profile, where a represents the feed offset along the x-coordinate.

$$\phi_{in}(x, y) = k_0\sqrt{(x-a)^2 + y^2 + F^2} \tag{5.3}$$

It is known that the phase compensation required by the lens depends on the phase path between the source and the surface, and on the desired pointing angle. Equation 5.4 reports the phase delay that the lens must provide to obtain a collimated output beam with an arbitrary tilt angle α_0. Analytically, it coincides with the equation 3.1 previously adopted, simplifying the calculation of the pointing direction with a one-dimensional problem.

$$\phi_{lens}(x, y) = k_0\left(x\sin(\alpha_0) - \sqrt{x^2 + y^2 + F^2}\right) \tag{5.4}$$

The phase of the outgoing wave is therefore the simple sum of the two terms, as shown in Equation 5.5.

$$\phi_{out}(x, y) = k_0\sqrt{(x-a)^2 + y^2 + F^2} - k_0\sqrt{x^2 + y^2 + F^2} + k_0 x\sin(\alpha_0) \tag{5.5}$$

When $a = 0$ the first two terms compensate each other, with the remaining phase term describing a tilted main beam with a zenith angle $\alpha(a = 0) = \alpha_0$, as required. The analysis of Equation 5.5 was conducted by Eduardo B. Lima *et al.* [39] to understand the factors influencing the antenna's scanning performance. The considered research examined the system behavior near the central focal point. With a Taylor expansion of Equation 5.5 around that location it is possible to rewrite the phase of the outgoing wave as the sum of a linear and a non-linear terms. It was observed that in a region close to the central position, the output phase front is approximately equal to the linear component, which simplifies the study of the system's behavior.

For the design of the proposed lens, the final result of the study will be extrapolated. The research determined a first approximation of the output beam zenith angle $\alpha(a)$ based on the previously described linearization, as reported in Equation 5.6.

$$\alpha(a) \;=\; arcsin\,\left[sin(\alpha_0) - \frac{2a/F}{\sqrt{4 + (a/F)^2}}\right] \tag{5.6}$$

The output angle depends only on the selected beam inclination for the central position of the source α_0 and the ratio between the feed offset a and the focal distance F. For $a = 0$, it is possible to observe that $\alpha(a = 0) = \alpha_0$.

Figure 5.10a shows the theoretical beam scanning range given by Equation 5.6 versus the feed offset a for different values of α_0. Each of these curves identifies a different unifocal configuration according to equation 5.4 and the desired angular range can be obtained with different feed translations.

By imposing the scanning range between 0° and 60°, it is possible to highlight the advantages and disadvantages derived from the choice of the parameter α_0. Considering boresight pointing ($\alpha_0 = 0°$), a more linear variation is obtained as the feed position changes. Concurrently, the desired 60° pointing is achieved with a large source shift. On the contrary, for $\alpha_0 \neq 0°$, higher beam tilt requires less displacement of the feed.

It is important to note that the introduction of a shift results in a performance penalty on the system, as previously observed in the case of the unifocal lens with feed rotation. Therefore, it is required to obtain the smallest possible translation with respect to the center of the structure that still allows to achieve the desired angular range. For this reason it is necessary to study the behavior of Equation 5.6 with the variation of the central pointing angle α_0, identifying the corresponding spacing Δ able to cover the $[0,60]°$ range.

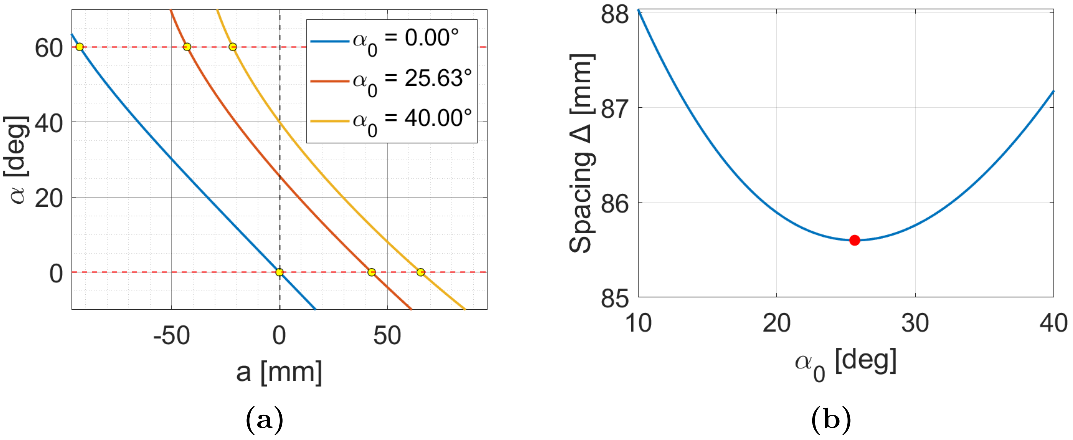

(a) **(b)**

Figure 5.10: Unifocal Study: **(a)** Beam direction angle as a function of the feed offset a, **(b)** α_0 optimization for spacing minimization.

Figure 5.10b shows the solution to the minimization problem. The curve exhibits a minimum point for $\alpha_0 = 25.63°$, a value for which the smallest possible feed translation of $\Delta_{min} = 85.16$ mm can be achieved. The value Δ_{min} reported represents the total movement that the feed must execute in order to pass from a boresight pointing to a 60° pointing. The maximum absolute distance with respect to the center of the structure is instead equal to $\Delta_{min}/2 = 42.6$ mm.

Once the optimal pointing angle α_0 is known, Equation 5.4 can be exploited to design the unifocal lens that guarantees the desired beam inclination for a central feed position at a focal distance $F = 80$ mm. The results obtained from this studied unifocal configuration will be presented subsequently.

With this strategy it is possible to design a bifocal lens that improves performance with the same angular coverage. Equation 5.7 describes the required phase compensation, which is defined as a weighted average of two distinct unifocal phase compensations.

$$\phi_{lens}^{bifocal} = \frac{A_1\phi_1^{unifocal} + A_2\phi_2^{unifocal}}{A_1 + A_2} \tag{5.7}$$

This weighted average must ensure two different behaviors of the surface based on the feed position along the x-axis. In this formula, the coefficients A_i, where $i = 1{,}2$, are Gaussian weight functions described in Equation 5.8.

$$A_i = e^{-\frac{(x-x_i)^2+y^2}{2\sigma^2}} \tag{5.8}$$

The Gaussian profiles guarantee a gradual transition between the two designed configurations. When $A_2 = 0$ or $A_1 = 0$ the lens phase correction reduces to the

unifocal case with focus at x_1 or x_2. The unifocal term $\phi_1^{unifocal}$ is dominant in regions of the lens near x_1, whereas near x_2 the dominant term is $\phi_2^{unifocal}$.
In order to minimize the losses associated to the translation, the two focal points must not be positioned too far from the center of the structure. For this reason the two feed centers were selected at symmetric distances of $x_1 = 30$ mm and $x_2 = -30$ mm. The value of σ is obtained instead from the analysis of the dominant electric field component E_y produced by the source.
Figure 5.11 shows the $|E_y|$ profile along the horizontal and vertical axes of the lens. The red dots represent the values extracted from the CST full-wave simulation. These points describe a spatial distribution that can be approximated to a Gaussian profile, which is plotted with a blue line. These curves are characterized by $\sigma_x = 32$ mm and $\sigma_y = 28$ mm for the two considered cut planes. The higher value between the two reported standard deviations is selected, obtaining in this way $\sigma = 32$ mm.

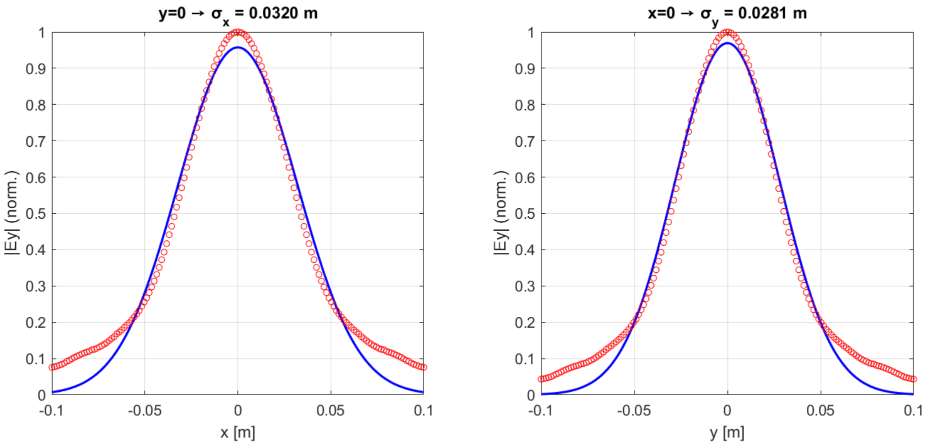

Figure 5.11: Gaussian approximations of $|E_y|$ in the horizontal and vertical planes of the surface.

Once x_1, x_2, and σ are known, it is possible to use the theory previously introduced to analyze the scan range of the two configurations. Since the focal coordinates were set by design, it is necessary to derive the unifocal configurations that allow to obtain the desired pointing directions with the feed placed at these two points. For a source positioned at coordinate $x_1 = -30$ mm a 60° pointing angle is required, while a boresight pointing is necessary at $x_2 = 30$ mm.
Starting from Equation 5.6, the two described unifocal profiles were derived. The first configuration has a pointing angle $\alpha_1 = 34.70°$ for a central feed position and allows a 60° pointing to be obtained with a translation $a = x_1 = -30$ mm. The second one, instead, is characterized by a pointing angle $\alpha_2 = 17.26°$ for a central feed position, enabling boresight pointing with a translation $a = x_2 = 30$ mm.

The schematic drawing of the two unifocal lenses with the feed in the central position is shown in Figure 5.12a.

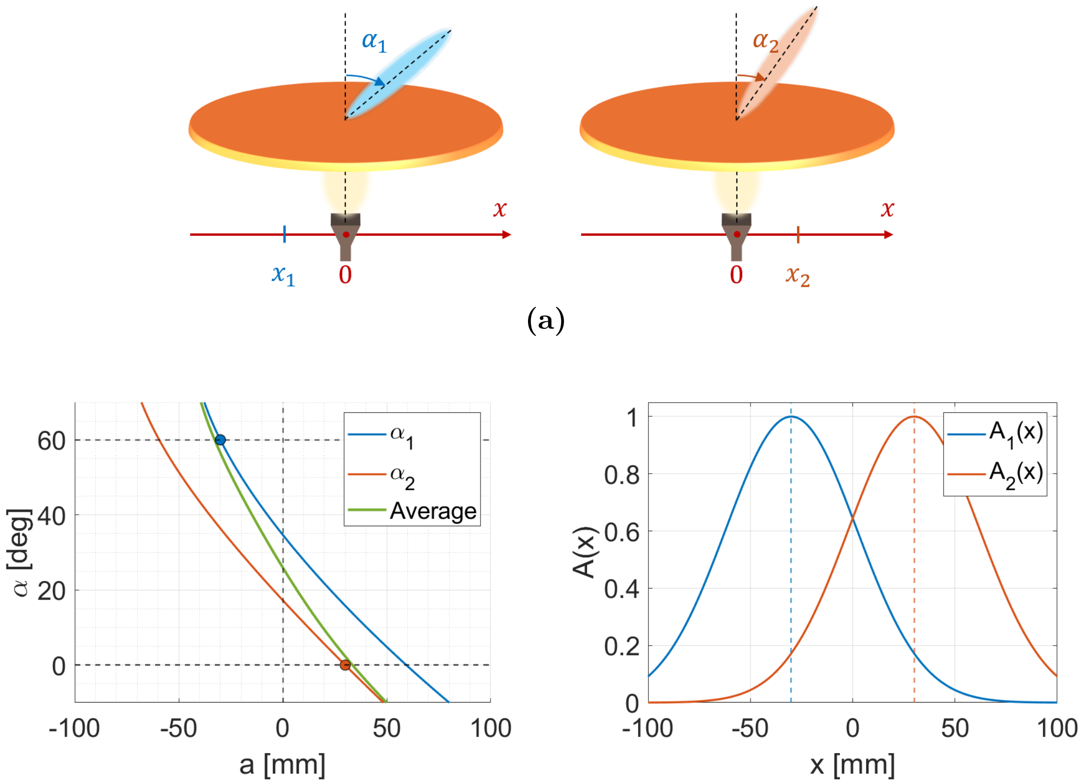

(a)

(b) **(c)**

Figure 5.12: Bifocal Study: **(a)** Schematic representation of the averaged configurations, **(b)** Beam direction angle as a function of the feed offset a, **(c)** Gaussian weight profiles.

Figure 5.12c shows the weights A_1 and A_2 in the horizontal plane, which are derived from Equation 5.8 knowing x_1, x_2 and the standard deviation σ.
Finally, Figure 5.12b represents the scan ranges of the two configuration with respect to the feed displacement. The blue curve describes the theoretical behavior of the first configuration while the red line is associated to second one. The final scan range obtained with the weighted average is reported in green and represents the theoretical bifocal behavior of the designed lens. As it can be seen it is able to cover gradually the same angular range with a reduced total shift with respect to the first designed unifocal lens.
Consequently, the two identified configurations were designed separately, with the resulting phase compensation determined by Equation 5.4. The phase distributions ϕ_1^{unifocal} and ϕ_2^{unifocal} are presented in Figure 5.13a and Figure 5.13b, respectively. The first one provides a theoretical 60° pointing for $x_1 = -30$ mm, while the second describes boresight pointing for $x_2 = 30$ mm.

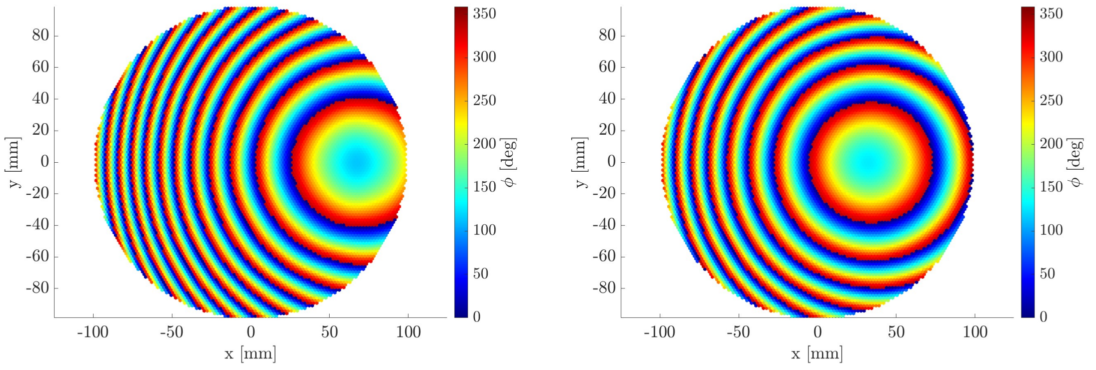

(a) $\phi_1^{unifocal}$

(b) $\phi_2^{unifocal}$

Figure 5.13: Phase distribution of the averaged configurations.

The phase compensation profile corresponding to the bifocal lens can be determined with the previously described weighted average of Equations 5.7 and 5.8. The result, along with the front view of the CST model used for the simulations, is presented in Figure 5.14.

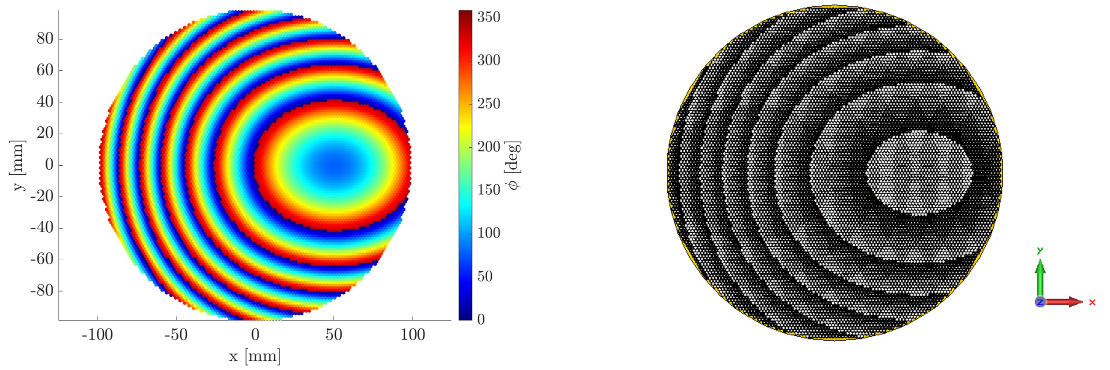

(a) **(b)**

Figure 5.14: Bifocal lens: **(a)** $\phi_{lens}^{bifocal}$ Phase distribution, **(b)** Front view of the CST model.

The study identified two TA configurations able to cover a scan range of $[0, 60]°$. The first one is a simple unifocal lens, designed to obtain a beam at 25.63° for a central feed position, while the second is the proposed bifocal configuration. Both structures were simulated using CST MWS and the results of the radiation patterns on the horizontal plane at 30 GHz are presented in Figure 5.15.

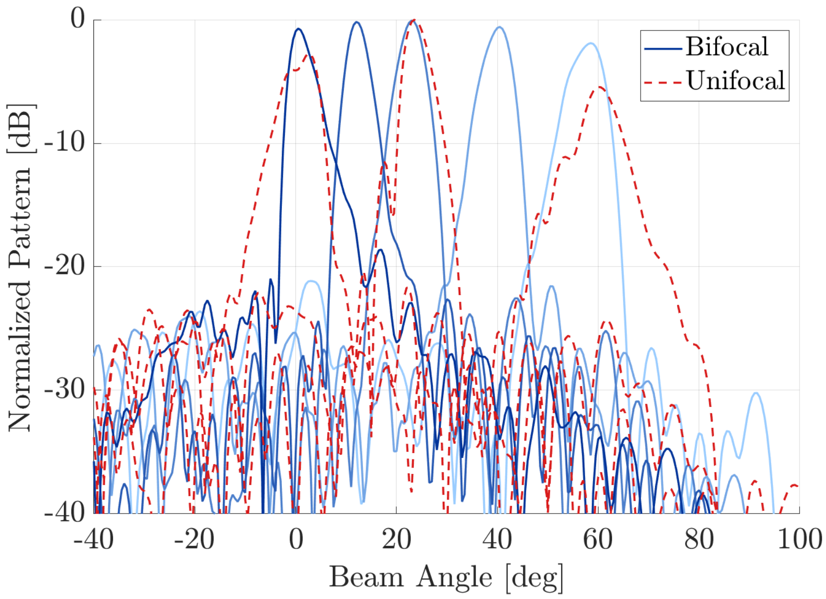

Figure 5.15: Feed translation: Bifocal lens radiation patterns versus the unifocal case in the horizontal plane at 30 GHz.

The performance of the unifocal configuration for three distinct source translations is shown in red. Specifically, for shift values $a = [50, 0, -50]$ mm, the correspondent pointing directions are $\theta_{\text{max}} = [2.7, 23.5, 59.5]^{\circ}$. The limits of the scan range are achieved with an absolute feed translation of 50 mm with respect to the central point. This result highlights the initial approximation adopted in Equation 5.6, which estimated an absolute variation of 42.60 mm based on the linearization of the output phase front. Optimal performance is achieved at the designed pointing direction, with a maximum gain of 27.94 dB and SLL of -11.42 dB. Moving the feed away from the central position leads to significant beam distortions and a scan loss exceeding 4 dB.

The bifocal configuration exhibits improved characteristics and was analyzed for five source shift values, reported with a blue gradient to facilitate better inspection of the resulting radiation profiles. For shift values $a = [40, 20, 0, -20, -40]$ mm the pointing directions are respectively $\theta_{\text{max}} = [0.5, 12, 23, 40.5, 58.5]^{\circ}$. As before, the initial approximation introduced by the mathematical model is still present. The simulations reveal two focal points at an absolute distance of 40 mm from the lens center, with a 10 mm deviation from the 30 mm estimated by the theoretical design.

Despite the introduced approximations, the overall performance of the bifocal lens is demonstrated to be effective. The radiation patterns are stable in the scanning process, with a marginal beam broadening when the the feed is far away with respect to the central position. In this centered location the best performance is obtained, with a maximum gain of 27.66 dB at 30 GHz. The scan loss is 1.5 dB and the SLLs are below -15 dB across the entire scanning range. The discussed results are summarized in Table 5.2. The comparison shows a significant improvement in lens performance when the bifocal configuration is adopted.

Table 5.2: Feed translation, unifocal versus bifocal designs at 30 GHz

	Maximum Gain	Scan Loss	Maximum SLL	Scan Range
Unifocal	27.94 dB	4.2 dB	-6.8 dB	$[2.7, 59.5]^{\circ}$
Bifocal	27.66 dB	1.5 dB	-15.2 dB	$[0.5, 58.5]^{\circ}$

To conclude, the in-band behavior of the two considered configurations was analyzed. Figure 5.16 shows the gain trends across the scanning range in the frequency band $[29, 31]$ GHz. A significant gain reduction is observed in the unifocal lens when the operating frequency increases. The behavior of the parameter is not stable in the band of interest and cannot be adopted for critical applications requiring stable wideband performance.

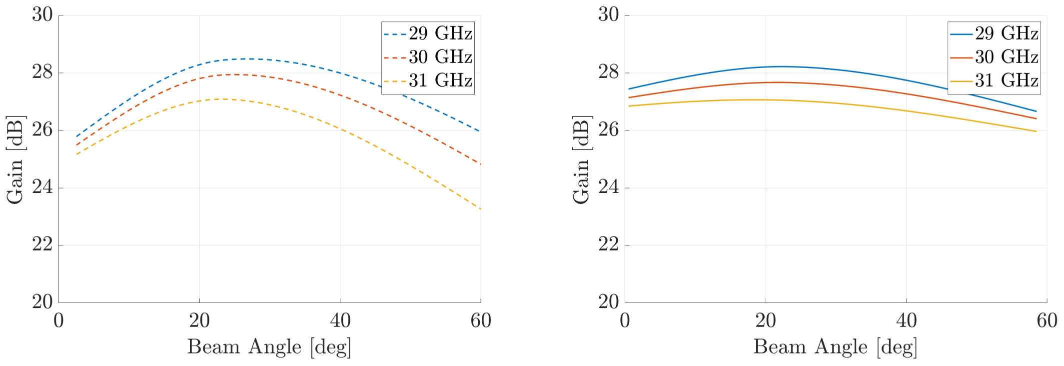

(a) **(b)**

Figure 5.16: Gain vs Beam Angle with feed translation: **(a)** Unifocal lens, **(b)** Bifocal lens.

The bifocal configuration exhibits the same trend with reduced slopes. The maximum value is obtained in the middle of the scan range for all the analyzed frequencies. In particular, at a frequency of 29 GHz and a pointing angle of 23°, the maximum gain of 28.21 dB can be achieved. The gain values are overall stable across the analyzed frequency range, with a total penalty of 2.2 dB considering the variations in both frequency and pointing angle.

The proposed solution provides a [0,60]° scanning along the x-axis. The structure can be implemented in a SOTM context with a reduced-size feed, such as a 2×2 patch array. The source can be placed in a fixed position, while the movement is assigned to the lens. The surface is placed at a reduced focal distance $F = 80$ mm with both translation and rotation capability to ensure full 360° coverage while maintaining the described scanning properties. In this manner, it is possible to obtain a system that provides a conical angular range of 60°.
The limitations are exclusively related to the mechanical movement, which can provide precise pointing at the cost of higher latency due to the inertia of the lens that must be displaced. The use of a fully dielectric material without metallization can marginally reduce the total weight of the structure.

Chapter 6

Conclusions and future work

The research conducted in this thesis provides a comprehensive understanding of the technical requirements and challenges involved in targeting civilian applications in the SOTM market. The need for low-profile, cost-effective antennas with high beam agility, driven by the rapid expansion of LEO and MEO constellations, guided the investigation toward a configuration consisting in a feed close to a planar meta-lens architecture as a possible alternative to complex phased arrays and bulky dome structures.

The work established the design methodology for a transmitarray adopted to realize the lens. The identification of a unit cell capable of ensuring low reflection and high transmission proved to be a fundamental requirement for an optimal system performance. The hexagonal unit cell with a tapered hole, selected through a parametric study, achieves the required phase coverage with low sensitivity from frequency and low dependence from the incident angle. The use of dielectric material enables fabrication through Additive Manufacturing (AM) techniques and the high dielectric constant contributes to a significant reduction in surface thickness. Preliminary analyses of the lens confirmed its excellent focusing and pointing properties. However, these performance metrics were initially achieved with a focal distance exceeding the strict limits of SOTM applications. In order to obtain a low-profile architecture, the study focused on implementing reduced focal-to-diameter ratios (F/D). This necessitated a critical methodological shift from the conventional far-field approximation to a dedicated near-field phase compensation model for the incident field and TA design. As the focal distance decreases, the results from these two approaches diverge significantly. This discrepancy validates effectively the proposed method, highlighting its superior accuracy in compact geometries where standard approximations fail.

By positioning the surface in the near-field region of the source, promising results were obtained. However, due to the passive nature of the material, the design is constrained to a fixed focal distance with a single desired pointing direction. This represented the primary limitation encountered during the research. Beam steering capabilities are severely restricted when both the feed and the lens remain in fixed spatial positions.

To overcome this limitation, an additional degree of freedom was introduced with the mechanical displacement of one of the system components.

Based on this principle, a preliminary bifocal lens was designed with a limited scanning range of ±32° and $F/D = 1$. However, the operating principle requires a mechanical rotation of the feed with respect to the surface center. This requirement imposes a severe structural limitation. The large focal distance adopted inherently expands the overall physical volume of the antenna, resulting in a bulky system that exceeds the volumetric constraints acceptable for mobile integration.

The second proposed design, therefore, introduces a bifocal lens with $F/D = 0.4$ and $[0, 60]^\circ$ scanning range, obtained with a simple translation of the feed along one direction. In order to simplify the feeding structure, the source is kept fixed and the lens is mechanically actuated to perform combined rotational and translational movements along multiple axes, ensuring full scanning flexibility. At the design frequency of 30 GHz, the gain reaches a maximum value of 27.66 dB with a scan loss of 1.5 dB, ensuring high stability across the scanning range with a maximum SLL of -15.2 dB. In the frequency band of interest (Ka-band), the gain ranges between 26.0 dB and 28.2 dB during the pointing operation, with a maximum variation of 2.2 dB.

This solution achieves the critical balance between wide-angle coverage (60°) and stable performance, while simultaneously satisfying the physical constraints required for the civil market.

Having successfully validated the feasibility of the project, this study serves as a foundational step toward future research. Beyond the critical imperative of eliminating all mechanical components to meet strict SOTM operational standards, several additional developments are necessary to transition the design into a possible commercial product. The study analyzed the surface behavior using a simple circular horn antenna, which can be replaced by a 2×2 or 4×4 patch array antenna with a significant reduced volume.

The study of the bifocal configuration is a first step towards multifocal architectures utilizing a planar arrangement of elementary feeds. In this scenario, beam steering could be achieved through the electronic commutation of distinct sources located on the focal plane, effectively discretizing the angular coverage. This architecture effectively addresses the limitations of mechanical beam steering systems, significantly reducing maintenance requirements and the risk of components malfunctions. However, the transition to a fully static system introduces a significant trade-off: it necessitates a higher complexity in the feeding structure and electronic control logic, requiring the integration of sophisticated switching matrices to manage the beam selection.

To preserve the structural simplicity of the system, the fixed positioning of the source is a necessary constraint. Consequently, future work will investigate a hybrid approach employing the compact patch array previously introduced as the primary feed. By manipulating the excitation coefficients of the array ports, an electronic pre-steering of the wavefront can be achieved.

The source can provide only a limited angular coverage, for this reason the performance improvement has to be achieved completely by the meta-lens design. Further research is required to design a surface capable of acting as an angular amplifier. Specifically, investigations should determine how distinct illumination zones can be mapped to wider deflection angles in order to maximize the steering capability of the source. In this context, the hexagonal discretization of the surface was selected precisely to facilitate the conical coverage with respect to a rectangular lattice.

Considering also the close proximity of the feed with respect to the lens, future work must refine the UC design to maintain consistently high transmission magnitude and minimal phase error under extreme oblique incidence.

In conclusion, this thesis has demonstrated a possible path toward high-performance, low-profile SOTM antennas using a robust bifocal dielectric meta-lens. The future work outlined represents the necessary steps to scale the validated concepts to meet the stringent demands of the emerging global civil SatCom market.

Bibliography

[1] Ryhan Uddin and Sathish Kumar. «SDN-based Federated Learning approach for Satellite-IoT Framework to Enhance Data Security and Privacy in Space Communication». In: Oct. 2022, pp. 71–76. DOI: `10.1109/WiSEE49342.2022.9926943` (cit. on pp. 1, 2).

[2] Alice Benini, Enrica Martini, Stefania Monni, Maria Carolina Viganò, Fabrizio Silvestri, Erio Gandini, Giampiero Gerini, Giovanni Toso, and Stefano Maci. «Phase-Gradient Meta-Dome for Increasing Grating-Lobe-Free Scan Range in Phased Arrays». In: *IEEE Transactions on Antennas and Propagation* 66.8 (2018), pp. 3973–3982. DOI: `10.1109/TAP.2018.2835575` (cit. on pp. 2, 6–9).

[3] R. Czarny et al. «High Permittivity, Low Loss, and Printable Thermoplastic Composite Material for RF and Microwave Applications». In: *2018 IEEE Conference on Antenna Measurements & Applications (CAMA)*. 2018, pp. 1–4. DOI: `10.1109/CAMA.2018.8530660` (cit. on pp. 3, 23).

[4] Thi Quynh Van Hoang, Julien Sourice, Erika Vandelle, Romain Faye, Matthieu Bertrand, and Brigitte Loiseaux. «Additive Manufacturing of a 460mm-diameter Flat Off-axis Lens for Ka-band Communications». In: *2023 17th European Conference on Antennas and Propagation (EuCAP)*. 2023, pp. 1–4. DOI: `10.23919/EuCAP57121.2023.10133541` (cit. on p. 3).

[5] Orcun Kiris, Kagan Topalli, and Mehmet Unlu. «A Reflectarray Antenna Using Hexagonal Lattice With Enhanced Beam Steering Capability». In: *IEEE Access* 7 (2019), pp. 45526–45532. DOI: `10.1109/ACCESS.2019.2909313` (cit. on p. 3).

[6] Ricardo Correia, Tiago Varum, João Nuno Matos, Arnaldo Oliveira, and Nuno Borges Carvalho. «User Terminal Segments for Low-Earth Orbit Satellite Constellations: Commercial Systems and Innovative Research Ideas». In: *IEEE Microwave Magazine* 23.10 (2022), pp. 47–58. DOI: `10.1109/MMM.2022.3188124` (cit. on pp. 5–7).

[7] Sérgio A. Matos, Nelson J. G. Fonseca, João C. Serra, João M. Felício, Jorge R. Costa, and Carlos A. Fernandes. «Generalized Risley Prism for Beam-Steering Transmit Arrays With Reduced Grating Lobes». In: *IEEE Transactions on Antennas and Propagation* 71.11 (2023), pp. 8420–8428. DOI: `10.1109/TAP.2023.3313230` (cit. on p. 6).

[8] Karu Esselle, Khushboo Singh, Dushmantha Thalakotuna, Mst Nishat Yasmin Koli, and Foez Ahmed. «Beam-Steering Antenna Technologies for Space-Related Applications». In: *2023 17th European Conference on Antennas and Propagation (EuCAP)*. 2023, pp. 1–5. DOI: `10.23919/EuCAP57121.2023.10133579` (cit. on pp. 6, 10).

[9] European Space Agency (ESA). *Low Earth Orbit*. Descrizione didattica dell'orbita terrestre bassa – altitudine, velocità orbitale, costellazioni. 2020. URL: `https://www.esa.int/ESA_Multimedia/Images/2020/03/Low_Earth_orbit` (visited on 08/07/2025) (cit. on p. 7).

[10] RedHotCyber. *Costellazioni di satelliti LEO: benefici e criticità*. Articolo online in italiano su vantaggi e criticità delle costellazioni LEO. 2024. URL: `https://www.redhotcyber.com/post/costellazioni-di-satelliti-leo-benefici-e-criticita/` (visited on 08/07/2025) (cit. on pp. 7, 8).

[11] SES S.A. *O3b mPOWER Newsroom Factsheet*. July 2020. URL: `https://www.ses.com/sites/default/files/2020-07/SES_O3b_mPOWER_Newsroom_Factsheet_v2.pdf` (cit. on p. 8).

[12] Cobham SATCOM (Sea Tel). *Sea Tel 3612 VSAT Antenna Data Sheet*. `http://www.sealink.co.kr/images/product/pdf/model-3612-antenna.pdf`. Accessed: 2025-11-07. 2013 (cit. on p. 11).

[13] General Dynamics Mission Systems. *M20-20M SATCOM-on-the-Move Terminal Data Sheet*. `https://gdmissionsystems.com/-/media/general-dynamics/ground-systems/pdf/on-the-move/satcom-on-the-move-20-20m-datasheet.ashx`. Accessed: 2025-11-07. 2021 (cit. on p. 12).

[14] Cobham SATCOM. *Cobham EXPLORER 9092M Ku/Ka-band Satcom-On-The-Move Antenna System*. `https://www.europasatellite.com/Cobham-Explorer-9092M-Satcom-On-The-Move-Ku-band-p/Cobham-Explorer-9092M-VSAT.htm`. Accessed: 2025-11-07. 2025 (cit. on p. 12).

[15] Kymeta Corporation. *Kymeta u8 Electronically Steered Flat Panel Antenna*. `https://www.kymetacorp.com/products/hawk-u8`. Accessed: 2025-11-07. 2025 (cit. on pp. 12, 13).

[16] Rolf Jakoby, Onur Hamza Karabey, Felix Goelden, and Atsushi Manabe. «Electronically steerable planar phase array antenna». U.S. Patent 10 320 089 B2. ALCAN Systems. 2019. URL: `https://patents.google.com/patent/US10320089B2` (cit. on p. 13).

[17] ALCAN Systems GmbH. *ALCAN Systems Enterprise NGSO Ground Antenna Data Sheet*. Accessed: Jan. 14, 2022. Darmstadt, Germany, 2020. URL: `https://www.alcansystems.com/files/data-sheets/2020-06-15_Data-Sheet-Antenna.pdf` (cit. on p. 13).

[18] Adam Bily, Nathan Kundtz, and M. Johnson. «Dynamic polarization and coupling control from a steerable cylindrically fed holographic antenna». U.S. Patent 10 587 042 B2. Apr. 2022. URL: `https://patents.google.com/patent/US10587042B2` (cit. on p. 13).

[19] ThinKom Solutions. *Airborne Satcom Antennas*. Ref. [22] in source document. Accessed: Jan. 14, 2022. 2022. URL: `https://www.thinkom.com/air/` (cit. on p. 13).

[20] SatixFy. *SatixFy Onyx Aero Terminal Brochure*. Accessed: Nov. 2024. 2024. URL: `https://www.satixfy.com/wp-content/uploads/2024/03/SatixFy-Onyx-Aero-Terminal-Brochure.pdf` (cit. on p. 13).

[21] Starwin. *ESA04 Phase Array VSAT Terminal*. Ref. [20] in source document. Accessed: Jan. 14, 2022. 2022. URL: `http://www.starwincom.com`.

[22] Ahmed Abdelrahman, Atef Elsherbeni, and Payam Nayeri. «Analysis and Design of Transmitarray Antennas». In: *Synthesis Lectures on Antennas* (Jan. 2017). DOI: `10.1007/978-3-031-01541-0` (cit. on pp. 16–18, 21, 22, 45).

[23] Miguel Dajer, Zhengxiang Ma, Leonard Piazzi, Narayan Prasad, Xiao-Feng Qi, Baoling Sheen, Jin Yang, and Guosen Yue. «Reconfigurable intelligent surface: design the channel – a new opportunity for future wireless networks». In: *Digital Communications and Networks* 8.2 (2022), pp. 87–104. ISSN: 2352-8648. DOI: `https://doi.org/10.1016/j.dcan.2021.11.002`. URL: `https://www.sciencedirect.com/science/article/pii/S2352864821000912` (cit. on p. 17).

[24] Tang-Jing Li, Guang-Ming Wang, Hai-Peng Li, and Hai-Sheng Hou. «Circularly Polarized Double-Folded Transmitarray Antenna Based on Receiver-Transmitter Metasurface». In: *IEEE Transactions on Antennas and Propagation* 70.11 (2022), pp. 11161–11166. DOI: `10.1109/TAP.2022.3188532` (cit. on p. 18).

[25] C. G. M. Ryan, M. R. Chaharmir, J. Shaker, J. R. Bray, Y. M. M. Antar, and A. Ittipiboon. «A Wideband Transmitarray Using Dual-Resonant Double Square Rings». In: *IEEE Transactions on Antennas and Propagation* 58.5 (2010), pp. 1486–1493. DOI: `10.1109/TAP.2010.2044356` (cit. on pp. 19, 20, 23).

[26] Andrea Massaccesi and Paola Pirinoli. «A Multilayer Unit-cell for Perforated Dielectric Transmitarray Antennas». In: *IEEE International Symposium on Antennas and Propagation (APS/URSI).* 2018, pp. 263–264. DOI: `10.1109/APUSNCURSINRSM.2018.8608712` (cit. on p. 22).

[27] Andrea Massaccesi, Paola Pirinoli, Valentina Bertana, and Giorgio Scordo. «3D-Printable Dielectric Transmitarray With Enhanced Bandwidth at Millimeter-Waves». In: *IEEE Access* 6 (2018), pp. 46407–46418. DOI: `10.1109/ACCESS.2018.2865353` (cit. on p. 22).

[28] K. Sakurai, Y. Yamaguchi, and T. Hori. «Huygens' Transmitarray Using Dual-Layer Metallic Patches». In: *IEEE Transactions on Antennas and Propagation* 68.5 (2020), pp. 3564–3574. URL: `https://arxiv.org/abs/2004.07129` (cit. on p. 23).

[29] He Li, Yun Bo Li, Chao Yue Gong, Shu Yue Dong, Shi Yu Wang, Hai Peng Wang, and Tie Jun Cui. «The Design of Programmable Transmitarray with Independent Controls of Transmission Amplitude and Phase». In: *arXiv preprint* arXiv:2109.08435 (2021). URL: `https://arxiv.org/abs/2109.08435` (cit. on p. 23).

[30] Emre Erdil, Kağan Topalli, and Nasim Seyedpour Esmaeilzad. «Reconfigurable Nested Ring-Split Ring Transmitarray Unit Cell Employing the Element Rotation Method by Microfluidics». In: *IEEE Transactions on Antennas and Propagation* 63.3 (2015), pp. 1164–1169. DOI: `10.1109/TAP.2014.2387424` (cit. on p. 23).

[31] Zhishu Qu, Yihua Zhou, James R. Kelly, Zhengpeng Wang, Kenneth Lee Ford, and Yue Gao. «A Reconfigurable Transmitarray Unit Cell Employing Liquid Metal». In: *IET Microwaves, Antennas & Propagation* 18.12 (2024), pp. 985–991. DOI: `10.1049/mia2.12518`.

[32] Samara Gharbieh, Jorick Milbrandt, Bruno Reig, Denis Mercier, Marjolaine Allain, and Antonio Clemente. «Design of a Binary Programmable Transmitarray Based on Phase Change Material for Beam Steering Applications in D-Band». In: *Scientific Reports* 14 (2024), p. 2966. DOI: `10.1038/s41598-024-53150-9` (cit. on p. 23).

[33] Trung Kien Pham, Liu Guang, David González-Ovejero, and Ronan Sauleau. «Dual-Band Transmitarray With Low Scan Loss for Satcom Applications». In: *IEEE Transactions on Antennas and Propagation* 69.3 (2021), pp. 1775–1780. DOI: `10.1109/TAP.2020.3031410` (cit. on pp. 25, 71, 72, 75).

[34] Erio Gandini, Fabrizio Silvestri, Alice Benini, Giampiero Gerini, Enrica Martini, Stefano Maci, Maria Carolina Viganò, Giovanni Toso, and Stefania Monni. «A Dielectric Dome Antenna With Reduced Profile and Wide Scanning Capability». In: *IEEE Transactions on Antennas and Propagation* 69.2 (2021), pp. 747–759. DOI: `10.1109/TAP.2020.3022960` (cit. on p. 25).

[35] Guang Liu, Mohammad Reza Dehghani Kodnoeih, Kien Trung Pham, Eduardo Motta Cruz, David Gonzalez-Ovejero, and Ronan Sauleau. «A Millimeter-Wave Multibeam Transparent Transmitarray Antenna at Ka-Band». In: *IEEE Antennas and Wireless Propagation Letters* 18.4 (2019), pp. 631–635. DOI: `10.1109/LAWP.2019.2899925` (cit. on pp. 25, 73, 75).

[36] Qiancheng Zhang et al. «Bioinspired engineering of honeycomb structure – Using nature to inspire human innovation». In: *Progress in Materials Science* 74 (2015), pp. 332–400. ISSN: 0079-6425. DOI: `https://doi.org/10.1016/j.pmatsci.2015.05.001`. URL: `https://www.sciencedirect.com/science/article/pii/S0079642515000377` (cit. on p. 25).

[37] Michele Beccaria, Giuseppe Addamo, Mario Orefice, Oscar Peverini, Diego Manfredi, Flaviana Calignano, Giuseppe Virone, and Paola Pirinoli. «Enhanced Efficiency and Reduced Side Lobe Level Convex Conformal Reflectarray». In: *Applied Sciences* 11.21 (2021). ISSN: 2076-3417. DOI: `10.3390/app11219893`. URL: `https://www.mdpi.com/2076-3417/11/21/9893` (cit. on pp. 47, 48).

[38] Sérgio A. Matos, Eduardo B. Lima, Jorge R. Costa, Carlos A. Fernandes, and Nelson J. G. Fonseca. «Design of a 40 dBi planar bifocal lens for mechanical beam steering at Ka-band». In: *2016 10th European Conference on Antennas and Propagation (EuCAP)*. 2016, pp. 1–4. DOI: `10.1109/EuCAP.2016.7481442` (cit. on pp. 72, 75).

[39] Eduardo B. Lima, Sérgio A. Matos, Jorge R. Costa, Carlos A. Fernandes, and Nelson J. G. Fonseca. «Circular Polarization Wide-Angle Beam Steering at Ka-Band by In-Plane Translation of a Plate Lens Antenna». In: *IEEE Transactions on Antennas and Propagation* 63.12 (2015), pp. 5443–5455. DOI: `10.1109/TAP.2015.2484419` (cit. on pp. 72, 73, 75, 81).

[40] Reda Madi, Antonio Clemente, and Ronan Sauleau. «Dual-Band, Aperture-Shared Transmitarray for Vehicular SatCom Applications». In: *IEEE Access* 11 (2023), pp. 71088–71096. DOI: `10.1109/ACCESS.2023.3293655` (cit. on pp. 72–74).

[41] P. Padilla, A. Muñoz-Acevedo, M. Sierra-Castañer, and M. Sierra-Pérez. «Electronically reconfigurable transmitarray at Ku band for microwave applications». In: *IEEE Transactions on Antennas and Propagation* 58.8 (Aug. 2010), pp. 2571–2579. DOI: `10.1109/TAP.2010.2050432` (cit. on p. 73).

[42] L. Di Palma, A. Clemente, L. Dussopt, R. Sauleau, P. Potier, and P. Pouliguen. «Circularly-polarized reconfigurable transmitarray in Ka-band with beam scanning and polarization switching capabilities». In: *IEEE Transactions on Antennas and Propagation* 65.2 (Feb. 2017), pp. 529–540. DOI: `10.1109/TAP.2016.2636833` (cit. on p. 73).

[43] Astrid Algaba-Brazález, Pilar Castillo-Tapia, Maria Carolina Viganó, and Oscar Quevedo-Teruel. «Lenses Combined with Array Antennas for the Next Generation of Terrestrial and Satellite Communication Systems». In: *IEEE Communications Magazine* 62.9 (2024), pp. 176–182. DOI: `10.1109/MCOM.024.2300370` (cit. on p. 75).

[44] Ulf Gustavsson et al. «Implementation Challenges and Opportunities in Beyond-5G and 6G Communication». In: *IEEE Journal of Microwaves* 1.1 (2021), pp. 86–100. DOI: `10.1109/JMW.2020.3034648` (cit. on p. 75).

Appendix

6.1 DXF file creation

The first generation approach based on the `.dxf` file is particularly suitable for the first two unit cell geometries, UC1 and UC2. These exhibit a simple configuration, characterized by a single hexagonal hole with diameter d, constant along the entire depth H of the cell. The Drawing Exchange Format (DXF) is a CAD data file format developed by Autodesk to enable data interoperability between AutoCAD and other software. To generate a `.dxf` file containing the geometry of an hexagonal unit cell, a custom MATLAB function was implemented. The purpose of the function is to write the ASCII instructions of a `.dxf` file directly into a text file, describing a closed polyline corresponding to a hexagon. The inputs of the function are:

- `fid`: the file identifier of the `.dxf` file opened in write mode;
- `Center`: the (x, y) coordinates of the hexagon center;
- `Diameter`: the distance between two opposite vertices of the hexagon, identified from us as the free parameter d.

The implementation of the described function adheres to a meticulously structured sequence of operations. Initially, the radius of the hexagon is determined as half the value of the provided diameter. With the center position of the cell and this radius known, the angular coordinates of the six vertices are calculated using basic trigonometric principles as shown in Fig. 6.1. Once the geometric framework is established, the creation of a `.dxf` file becomes necessary. This begins with the `HEADER` section, where the file version (specified as `AC1009`) is defined to ensure compatibility with CST software. Following this, a `TABLES` section is introduced to configure a dedicated layer named `Hexagons`, designated to contain all geometric entities relevant to the design. The central element of the file resides in the `ENTITIES` section. Within this section, a `POLYLINE` entity is initiated, representing the hexagonal shape. Each of the six previously computed vertices is recorded sequentially as `VERTEX` entries. This entity is subsequently concluded with the

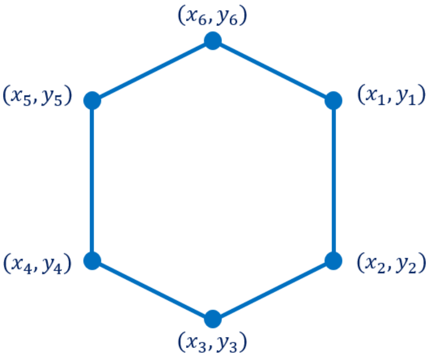

Figure 6.1: Hexagon written in the `.dxf` file.

`SEQEND` instruction, ensuring closure of the polyline. Finally, the `.dxf` file is terminated with the standard `EOF` command. This sequence produces a valid `.dxf` file that effectively encodes a hexagonal structure, centered at the specified location. The procedure can be repeated for each individual cell, culminating in a single unique file that can be seamlessly imported into CST and used as a parametric geometric building block for transmitarray design. After importing the `.dxf` file, an initial extrusion operation is required to obtain the dimensional geometry. By setting a depth H, the desired 3D models can be generated, shown in light blue in Fig. 6.2. The final stage involves a Boolean subtraction operation between a metalens—characterized as a simple cylinder with depth along the z-axis equal to the defined parameter H—and the resulting hexagonal structure. The outcome of this process is a finalized metalens featuring the desired holes, whose dimensions vary within the range dictated by parameter d, such as depicted in Figure 6.2.

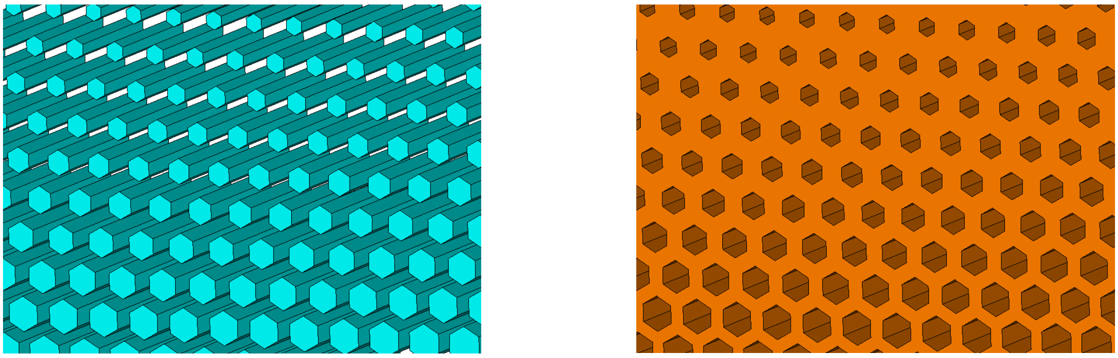

Figure 6.2: Generated 3D model and final result for the UC2 case.

6.2 STL file creation

The second approach enables the creation of any parametric solid by generating an `.stl` file. This method was specifically used to design the third type of unit cell UC3 which features a more intricate internal structure due to tapering introduced to enhance matching performance. Unlike the simple extrusion operation performed earlier using the `.dxf` file, this process requires a complete model to be constructed for subtraction from the surface. To address this requirement, the STL (Stereolithography) format was utilized, as it is among the most widely recognized standards for 3D object representation in CAD applications and additive manufacturing. An `.stl` file represents a solid's surface through a collection of triangular facets, each defined by three vertices and an associated normal vector. For this project, a MATLAB function was developed to produce the desired parametric geometry. The function accepts key inputs, including the overall dimensions of the unit cell, the depth of the hole, and the coordinates of the outer face's center. Based on these parameters, the vertices of a hexagon are calculated at varying depths to define the 3D shape while ensuring proper alignment of the hole along the cell's axis. After calculating the vertices, the function generates triangular faces that collectively form the solid's surface. For each facet, the normal vector is computed using the right-hand rule to ensure it points outward from the structure in the STL representation. These triangles, along with their respective normal vectors, are then sequentially written into an ASCII `.stl` file using syntax compatible with most CAD and simulation tools.

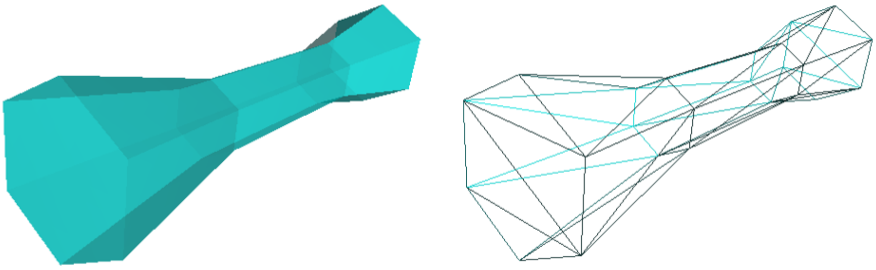

Figure 6.3: 3D parametric model.

This streamlined process facilitates rapid generation of the entire parametric structure while allowing variation of the free parameter d across different surface points. The result of this approach is illustrated in Figure 6.4.

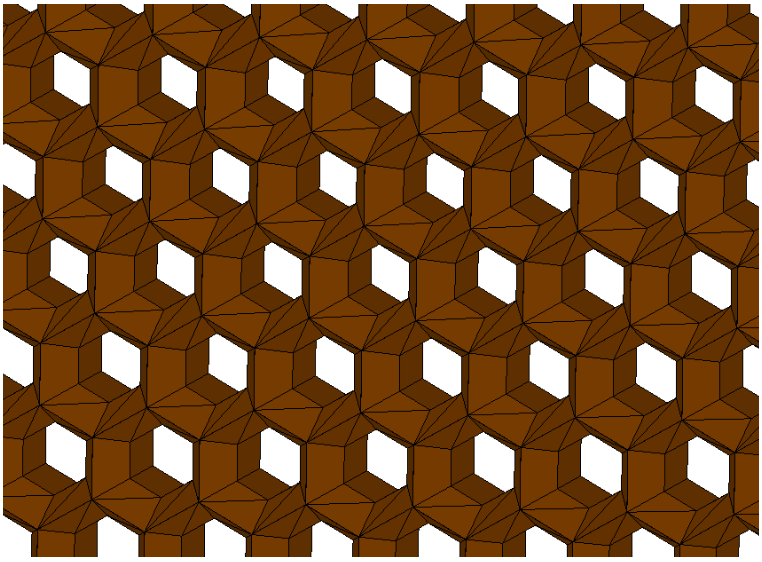

Figure 6.4: Final result for the UC3 case.